Mesoscopic Distinct Element Method for Multiscale Modeling of Carbon Nanotubes

A DISSERTATION

SUBMITTED TO THE FACULTY OF THE GRADUATE SCHOOL

OF THE UNIVERSITY OF MINNESOTA

BY

Hao Xu

IN PARTIAL FULFILLMENT OF THE REQUIREMENTS

FOR THE DEGREE OF

DOCTOR OF PHILOSOPHY

Advisor: Traian Dumitrică

July, 2019

Acknowledgements

In reminiscence of the past five years, it has been a very special life experience for me. Now as I am about to say farewell to my Ph.D. career and start a new journey, I would like to express my sincere gratitude for those who offered me tremendous help in so many ways.

First I would like to thank my advisor Professor Traian Dumitrică. It has been a very enjoyable experience working under his guidance. He is very nice, encouraging and knowledgeable. Not only am I grateful for his helpful advice which shed light on my way while I was wandering in the dark forest of science, but also for the comfortable environment he provided where I could really enjoy my research.

Also I would like to thank my committee members Professor Richard D. James, Professor Thomas Schwartzentruber, Professor Stefano Gonella and Professor Jialiang Le for their time and effort as well as valuable questions and

advice on my research.

I would like to acknowledge all of my collaborators, Dr. Yuezhou Wang, Dr. Jihong Ma, Mr Grigorii Drozdov, Dr. Prashant Kumar and especially Professor Andre Mkhoyan. They teach me a lot. It would be a much tougher experience without their help.

During the five years, I couldn't remember how many times my friends had helped me. Some of them are new friends, Kuan Zhang, Jiadi Fan, Mingjian Wen, Hanlin Gu, Yuchen Luo, and Tao Zhang. I spent my five years with them here in Minnesota. Some are old friends, Lilong Zhang, Wenzhe Zhu, Wenzheng Yang, Xiao Liu, Su Xu, Baoran Jia, Siming Ma, and Shushan Cui. I deeply treasure the friendship with all my friends.

Finally and most importantly, I want to thank my parents. No more word is necessary. They are the best parents.

I appreciate National Science Foundation, NASA and Minnesota Supercomputer Institute for their kind support.

Abstract

Super strong lightweight material systems comprising carbon nanotubes (CNTs) are especially suitable for aerospace applications. Assembles of CNTs obtained by mechanically stretching the CNT sheets, represent a promising material platform for developing composite materials with mechanical attributes approaching those of individual CNTs. In this quest, the guidance power of computational materials modelling is critical. Ideally one would like to investigate CNT assembles with all atom simulation methods, but this approach is computationally prohibitive. Due to the inherent spatial and temporal limitations of atomistic modeling and the lack of mesoscale models, mesoscopic simulation methods for CNT systems are missing. My work focuses on deriving ultra-coarse-grained models based on mesoscopic dintinct element method (mDEM). Our mDEM model is informed by atomistic data obtained with molecular dynamics (MD) and density functional theory-based tight-binding (DFTB) objective molecular modeling. Our mDEM model is capable of reproducing the atomistic elastic and frictional properties of CNTs. With the mDEM model, tensile tests of mesoscale CNT network were carried out, showing results in good agreement with experiments. The tensile tests revealed nanofriction was a key factor deciding the load transfer of CNT network.

Our mDEM model serves as a powerful tool to expand the understanding and guide the development of CNT materials.

Contents

List of Tables

List of Figures

Chapter 1

Introduction

1.1 Motivation and Objectives

Composite materials, such as wood and bone, consists of relatively strong, stiff fibers (cellulose and hydroxyapatite) located in a tough resin (lignin and collagen). By combining materials with complementary properties, the natural composites obtain most of the benefits (high strength, stiffness, toughness, and low density) with few of the weaknesses of the individual components. Better known synthetic composites, carbon- and glass-fiber-reinforced plastic, are widely used in the aerospace and other industries. They consist of carbon and glass fibers, which are stiff and strong, but brittle, in a tough polymer matrix. Nevertheless, carbon nanotubes (CNTs), allotropes of carbon with cylindrical nanostructure - are an

order of magnitude stronger [1] than any other engineered fiber. Unfortunately, for the past decades it has been a challenge to fully utilize the enormous CNT potential for manufacturing super-strong composites.

In addition to excellent mechanical properties, mass saving is a prime factor in selecting materials for the aerospace industry. A key difference between fibrous and particulate composites relates to directionality of properties. While particulate composites are isotropic (i.e., their properties are the same in all directions), fibrous composites are anisotropic (i.e., their properties vary depending on the direction of the load with respect to the orientation of the fibers). This anisotropy is overcome by forming a laminate, i.e., by stacking panels, each often only fractions of a millimeter thick, on top of one another with the fibers oriented at different angles. To produce important material savings, and therefore mass savings, the differently-oriented panels are not randomly stacked but stacked in intricate engineered sequences that maximize the mechanical properties of the laminate.

Rather than focusing on further optimizing the stacking sequences of existing carbon fiber laminates, I work on enabling the manufacturing of new CNT-based composites for laminate panels in a computationally-guided approach. During synthesis, the parameters (diameter, length, number of inner walls) of the individual CNTs can be adjusted, but the consequences on the materials'

properties are not known a priori. Since an exhaustive exploration of the large parameter space by direct manufacturing is impractical, the guidance offered by simulations is critical. Multiscale simulations are used to predict the variations in mechanical response caused by these parameters, and to guide the synthesis conditions toward the optimal parameters of the CNTs. Further, simulations are used for developing designs for hybrid CNT mats impregnated with polymer fillers.

The specific goal of my research is to enable multiscale simulations by filling the current gap between atomistic molecular dynamics (MD) and continuum finite element modeling (FEM) methods. Ideally, one would like to simulate the CNT systems with all-atom MD simulations [1]. While MD is valuable for modeling atomic scale deformations, unfortunately it is not suitable at substantially larger scales due to prohibitive computational cost and complexity. For example, the problems of study of CNT materials require time integration of representative assemblies of CNTs, including at least billions of carbon atoms. Besides, capturing in a realistic manner the CNT relaxation and energy dissipation processes during material deformation requires simulations under "slow" applied strain rates; this regime requires at least tens of microseconds time span. With the modern performance of computational clusters, such spatial and temporal scales remain prohibitive. At macro scales, FEM can successfully analyze the behavior of CNT composites. Nevertheless, extending FEM to model mesoscopic scale features for

CNT composites is challenging due to the complex topologies, inhomogeneities, and the dynamical inter-tube sliding. At mesoscopic dimensions, between the atomic scale of MD and the macro scale of FEM, an important gap exists in our ability to model the CNT composites. Understanding this scale is critical, since the extreme variability in topology and wide range of material defects have a direct impact on the material's mechanical properties.

To this end, I am developing a new coarse grained (CG) capability, titled the mesoscopic distinct element method (mDEM), which is being built on the framework of classical DEM [2]. CG modeling aims at simulating the behavior of complex systems using their CG simplified representation. Nowadays, CG models are widely used for modeling of polymers and biomolecules at various granularity levels. Molecules are represented by pseudo-atoms (that replace a group of atoms). By decreasing the degrees of freedom, much longer simulation times can be studied than using all atom MD. Bead-and-spring (BS) CNT models [3], are largely used today for studying the mesoscale mechanics of CNT systems. While extremely valuable, BS present a series of deficiencies, which make them unsuitable for the problem at hand. These deficiencies include improper accounting of the inter-tube load transfer between CNTs represented with large granularity, and neglect of the torsional deformation of the CNTs. The mDEM developed in my project represents the next generation of CG models for CNTs. mDEM represents a CNT

by a chain of rigid discrete elements interacting through contacts [2]. mDEM is an ultra CG representation as each element generally represents a segment of the detailed CNT containing hundreds of carbon atoms. My PhD work focuses mainly on informing the mDEM contacts with accurate atomistic-level input in order to transfer the essential nanomechanics to the mesoscale.

1.2 Carbon Nanotubes

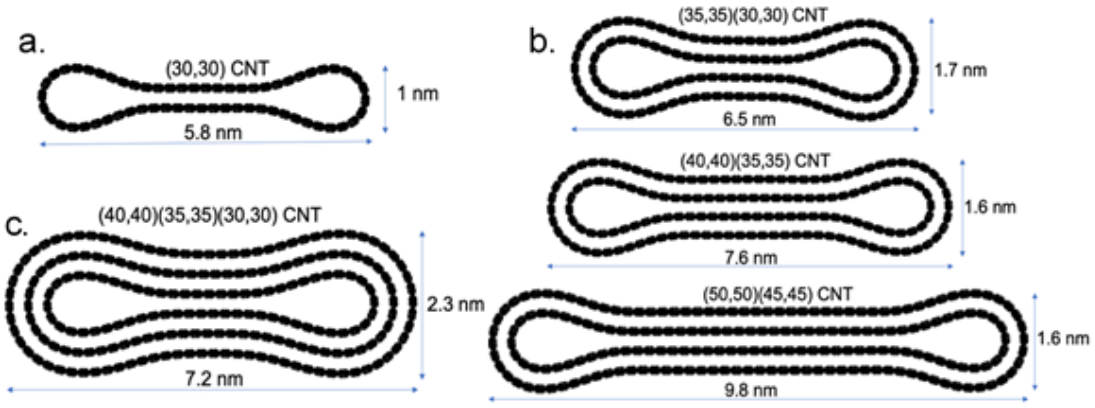

Figure 1.1. Cross-sectional views of a) a single-walled collapsed CNT, b) double-walled collapsed CNTs of different widths, and c) a triple-walled collapsed CNT, as obtained with DFTB.

Carbon nanotubes (CNTs) have always been an eye-catching material

since its discovery, thanks to its extraordinary mechanical[1], thermal and electrical properties[4–6]. CNTs can be viewed as a structure formed by rolling up a graphene sheet into a hollow cylinder along a characteristic chiral vector $\vec{C} = m\vec{a_1} + n\vec{a_2}$. Here $\vec{a_1}$ and $\vec{a_2}$ are the two unit vectors of the graphene lattice. $\vec{C}$ defines the circumference of the cylinder. Based on m and n, CNTs can be characterized as zigzag ($m = 0$ or $n = 0$), armchair ($m = n$) and chiral ($m \neq n$) CNTs.

Diameter of CNTs varies from a few angstroms to tens of nanometers. Nevertheless, the morphology of CNTs is not always cylindrical. Zhang etc [7] found collapsed single-walled CNTs were energetically more stable than the cylindrical configuration when the diameter exceeds $62\mathring{A}$. Recent atomic-resolution transmission electron microscopy on the stretched sheets also found the massive presence of collapsed CNTs[8]. Figure 1.1 shows the dog-bone cross section of collapsed CNTs.

1.3 Kolmogorov Crespi Potential

To get better understanding of the mechanics of CNT systems, it is critical to obtain accurate description of the van der Waals (vdW) interaction between CNTs. The vdW interaction was typically described with Lenard-Jones

(L-J) type potential [9]. Nevertheless, L-J potential significantly underestimates the characteristic corrugation between commensurate graphene layers. As one graphene layer slides with respect to another, overlap of π orbitals leads to large energy barriers L-J potential fails to capture. To address this issue, a newly developed registry dependent Kolmogorov-Crespi (K-C) potential was selected in our simulations to describe the corrugation, equation 1.1 [3].

$$\begin{gathered} V(\vec{r_{ij}}, \vec{n_i}, \vec{n_j}) = e^{-\lambda(r_{ij}-z_0)}[C + f(\rho_{ij}) + f(\rho_{ji})] - A(r_{ij}/z_0)^{-6} \\ \rho_{ij}^2 = r_{ij}^2 - (\vec{n_i}\vec{r_{ij}})^2 \\ \rho_{ji}^2 = r_{ij}^2 - (\vec{n_j}\vec{r_{ij}})^2 \\ f(\rho) = e^{-(\rho/\delta)^2} \sum C_{2n}(\rho/\delta)^{2n} \end{gathered} \tag{1.1}$$

Here $\vec{n_i}$ and $\vec{n_j}$ are local orientations of π orbitals of the two interacting atoms. Our implementation of the KC potential uses the scheme proposed by Haddon [10]. For each carbon atom we needed to locate the positions of its three nearest neighbor atoms in order to define its π orbital orientation as the direction perpendicular to the plane formed by those neighbors.Specifically, $\vec{n_i} = (\vec{x_2} - \vec{x_1}) \times (\vec{x_2} - \vec{x_1})/|(\vec{x_2} - \vec{x_1}) \times (\vec{x_2} - \vec{x_1})|$, Figure 1.2. For all the parameters, we followed ref [3], $C_0 = 15.71$, $C_2 = 12.29$, $C_4 = 4.933$, $C = 3.030$, $\delta = 0.578\mathring{A}$, $\lambda = 3.629\mathring{A}^{-1}$,$A = 10.238$, $z_0 = 3.34\mathring{A}$.

The adequacy of the KC potential is demonstrated in Figure 1.3. Figure 1.3a and Figure 1.3b, we display two graphene layers in which the a lattice vectors

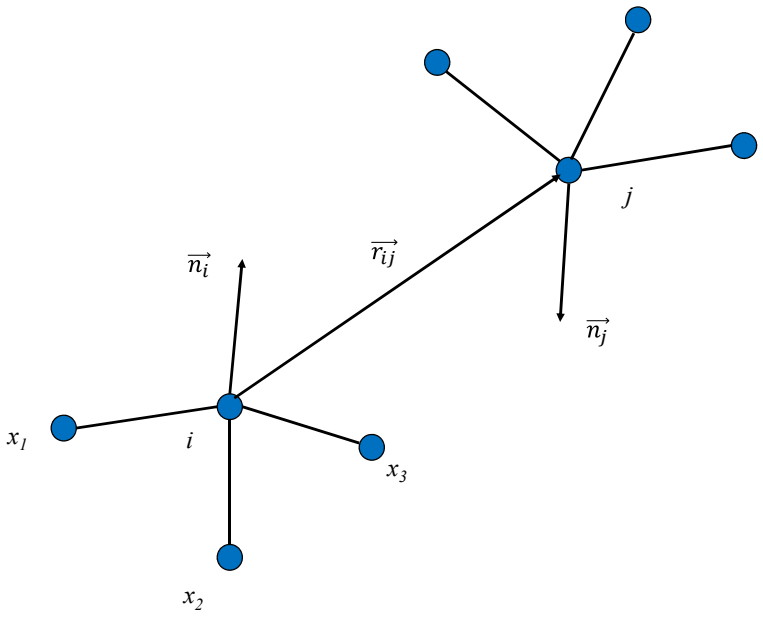

Figure 1.2. Schematics of π orbitals of two nearby carbon atoms.

of the two layers are parallel and perpendicularly oriented, respectively. In Figure 1.3c, it can be seen that the shifting of the top layer along the armchair and zigzag lattice directions leads to a periodic corrugation of the vdW energy for the commensurate periodicities (periodicity ratio 1), but a vanishing corrugation when the periodicities are incommensurate (periodicity ratio 1/3).The measured energy barrier agrees well with DFT results[3].

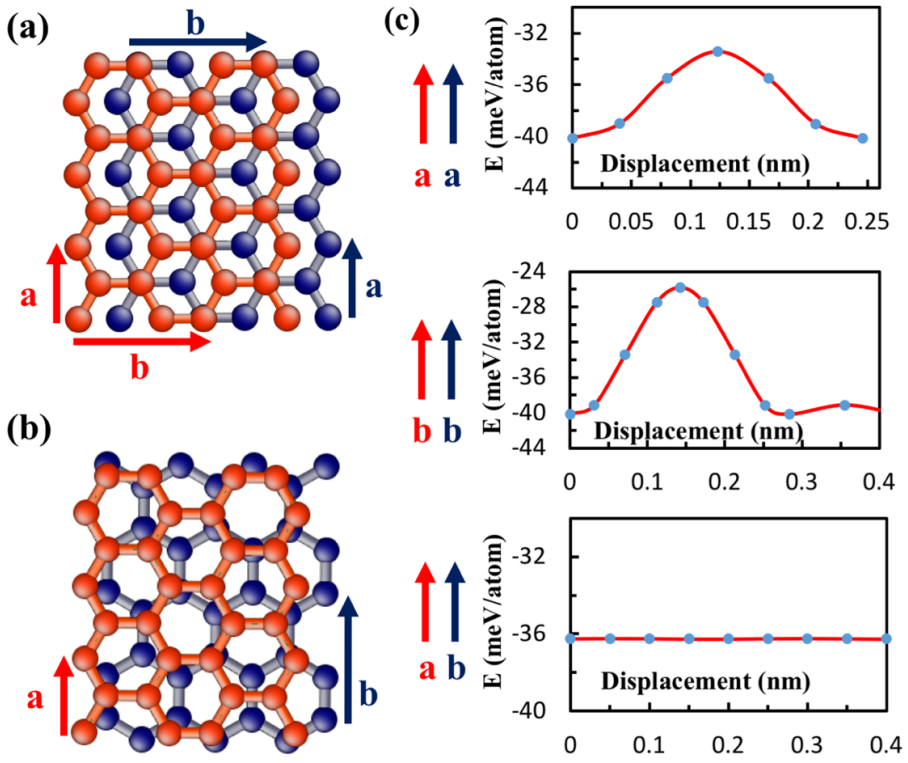

Figure 1.3. Two stacked graphene layers with the lattice vectors of the rectangular unit cells (shown by arrows) (a) parallel (AB stacking) and (b) 90° rotated. (c) The KC interlayer vdW energy versus in-plane relative displacements of the two layers. The displacement directions for each layer are indicated by the arrows. The interlayer distance is kept at 0.335 nm.

1.4 Distinct Element Method

The simulation scheme we use to model mesoscale CNT network is Distinct Element Method (DEM). DEM was developed by P. Cundall for geomechanics [11], and was widely applied in civil and petroleum engineering [12]. DEM elements are treated as rigid bodies with translational and rotational degrees of freedom. Different elements are connected with linear normal and shear springs representing their interactions. Such interactions are called contact models. For CNT networks, each DEM element represents a segment of CNT, consisting of hundreds of carbon atoms. Specifically for cylindrical (10,10) single-walled CNTs, each cylindrical element has length of 1.36 nm and radius of 0.68 nm, consisting of 220 carbon atoms[13]. These mesoscopic elements are tracked in the Lagrangian frame. In the PFC3D implementation[14], they are evolved deterministically in time as rigid bodies with a damped scheme based on a velocity Verlet algorithm for translations and a fourth-order Runge–Kutta for rotations.

We name the first type of contact model parallel-bond contacts, which are trained to capture the intra-tube covalent interactions responsible for the local linear elasticity of individual CNTs. In addition, we account for the microscopic vdW interactions, which are represented at the mesoscale by the non-bonded contacts acting between elements in close spatial proximity [13]. The cylindrical

elements are coupled by parallel-bond contact, which introduce forces (F) and moments (M) to resist relative displacements and rotations. The parallel-bonds were calibrated to atomistic data [13], and the chain of parallel-bonded elements describes the individual CNT as an Euler–Bernoulli beam. Mesoscopic elements located on two different CNTs may interact via vdW and viscous contacts. The vdW contact has been developed by us via a procedure that involves the integration of the atomistic vdW interactions between two CNTs[13]. Our vdW contacts capture the general case when two finite size CNTs are misaligned and crossed. Unlike isotropic potentials, our anisotropic vdW potential is free of "corrugated" spurious effects [15], which could cause artificial load transfer between CNTs. Thus, in mDEM, missaligned (shifted) parallel CNTs will undergo smooth sliding under the action of mesoscopic vdW forces. Similarly, crossed CNTs will be zipping under under the action of the long-ranged vdW forces and aligning moments. Ref [13] gives the explicit form for the mesoscopic vdW forces and moments.

The athermal model overviewed above is augmented next to capture the dissipative atomistic scale processes. mDEM presents two channels for energy dissipation: a viscous damping and a local damping [13,16]. The effective dissipative force acting between two aligned CNTs is captured by dashpot viscous contacts with constitutive equation $\vec{F_d} = \gamma \vec{v_r}$, acting in parallel with the vdW contacts. Here $\vec{F_d}$ is the friction force, $\vec{v_r}$ the relative velocity of the distinct elements in vdW

contact, and γ is the linear viscous coefficient. Local damping adds forces ($\vec{F}_\alpha$) and moments ($\vec{M}_\alpha$), $\vec{F}_\alpha = -\alpha\vec{F}sign(\vec{v})$ and $\vec{M}_\alpha = -\alpha\vec{M}sign(\vec{w})$, where $\vec{v}$ and $\vec{w}$ are the translational and rotational velocities of an element, respectively, and α is the local damping parameter. Local damping is introduced in the classical DEM [34] with the sole goal of stabilizing the numerical time integration.

1.5 Organization of the Thesis

The focus of my thesis can be categorized into three aspects. First with atomistic scale modeling (MD and DFTB), we obtain quantitative description of the elasticity of individual CNT as well as friction and vdW interaction between CNTs. Next we develop DEM contact models capable of reproducing atomistic behaviors. Finally, the model was applied for mesoscale CNT network simulations.

In Chapter 2 we go over a widely studied problem, CNT oscillator, with the K-C potential. The findings, contrary to previous results, reveal the importance of corrugation in the study of CNTs. Chapter 3 describes our MD simulations to calculate friction between CNTs. Chapter 4 focuses on the contact model for the elasticity of collapsed CNTs. Chapter 5 studies the bending properties of few-layer graphene. Chapter 6 shows some network simulation examples, and compares DEM model with a BS model. Chapter 7 concludes the thesis, and

provides envision for possible future research directions. Most of this work was published in the following references: Ref[17], Ref [18], Ref [19] and Ref [20].

Chapter 2

Role of Inter-tube Corrugation in the Dynamic Sliding Friction of Concentric Carbon Nanotubes

Based upon the experimental realization of low-friction nanoscale bearings, carbon nanotubes (CNTs) attracted interest for designing GHz nested CNT nanomechanical oscillators. A key issue in designing such devices is the energy dissipation during the oscillatory sliding of the inner CNT. In this chapter, dynamical sliding of concentric double-walled CNTs of nanometer lengths and different commensurations is investigated with molecular dynamics simulations and a model potential that accounts for inter-tube corrugation. We find that accounting for

the small variation in energy under inter-tube shifts and rotations gives rise to a dependence of the frictional forces not only on velocity and edge, but also on the contact area and commensuration. Coupled to sliding, we observed an unusual dissipation of the sliding motion into spinning motion, which is also connected to commensuration. These results advance our understanding of dynamical friction and suggest that considerations on interfacial corrugation are important in designing CNT oscillators even when their intra-tube gap is larger than 3.3 $\mathring{A}$. This chapter has been published in Ref [17].

2.1 Introduction

Multi-walled carbon nanotubes (CNTs) [21] are quasi one-dimensional nanostructures comprising concentric tubular graphene layers. While the intralayer sp^2 chemical bonds that make each individual tubule imparts extraordinary stiffest and strength [22, 23], the predominantly van der Waals (vdW) inter-wall interactions confers ultra-smooth contacts between tubules [24]. In a pioneering work, Cumings and Zettl [25] demonstrated that an inner tube can be pulled out by a small force applied via a carbon-tipped manipulator, and it can also be spontaneously pulled back to its initial position that maximizes the

vdW energy. Notably, the telescopic extension–retraction process could be operated repeatedly as it does not cause structural damage on the adjacent surfaces. Based on this result, Zheng and Jiang [26] have proposed that multiwalled CNTs could be the basis for a new generation of nanomechanical oscillators. Using static models, they have predicted that multiwalled CNTs could lead to nano-oscillators in the range of several GHz. However, in order to design such devices, aspects that can compromise device performance, such as inter-tube friction have to be considered.

The independence of macroscopic friction on the contact area refers to the projected or apparent contact area, whereas a real contact occurs between rough surfaces. [27] However, the nano-scale interface between defect-free concentric CNTs is exceptionally smooth. The energetic barrier to axial sliding in defect-free long CNTs containing thousands of atoms can be comparable to that for a single unit cell of crystalline graphite evaluated at 15 meV/atom with density functional theory calculations. [24]. The force originating from the atomic-scale corrugation of the inter-tube potential is more than two orders of magnitude lower that the force related to the decrease in the surface area of vdW interaction, [28–30] and thus cannot be expected to make any significant contribution to the static friction. For this reason, molecular dynamics (MD) simulations for

these systems [30–34] are typically utilizing for the inter-tube interatomic interactions a Lennard-Jones (L-J) treatment, which is capturing well the vdW adhesion between CNTs.

Using MD, Legoas et al. [29] confirmed that the GHz nano-oscillators are dynamically stable when the radii difference values between inner and outer tubes are of ~ 3.4 $\mathring{A}$. Tangney et al. [33] found that the dynamical friction is independent of the overlap area between tubes, and that tube commensuration does not lead to significantly increased dissipation. The primary source for friction was found to be the edges of the CNTs. In contrast, Guo et al. [32] obtained that energy dissipation in a commensurate (such as armchair/armchair or zigzag/zigzag) oscillator is larger than in an incommensurate (e.g., zigzag/armchair) oscillator. Nevertheless, because the L-J treatment utilized in all these simulations is much too smooth, the variations in the relative alignment of adjacent walls [35, 36] responsible for commensuration effects are practically not captured. Focusing on the role of commensuration on the oscillatory motion, in this chapter we re-examine this issue with classical MD that relies on the registry-dependent Kolmogorov–Crespi (K-C) [34] potential for the inter-tube interactions. Because of the difficulties in the precise calibration of the K-C potential on the tubular CNT interfaces, the obtained rates of the energy dissipation are qualitative semiquantitative. Nevertheless, by looking at possible relations among the dependence of

calculated $F_{frictionon}$ the inter-tube corrugation landscape, and the damping of the telescopic oscillations in double-walled CNTs observed in MD, we focus here on qualitative behavior, namely on the possible dependence of $F_{friction}$ on the contact area. [18, 37, 38]

2.2 Computational Methods

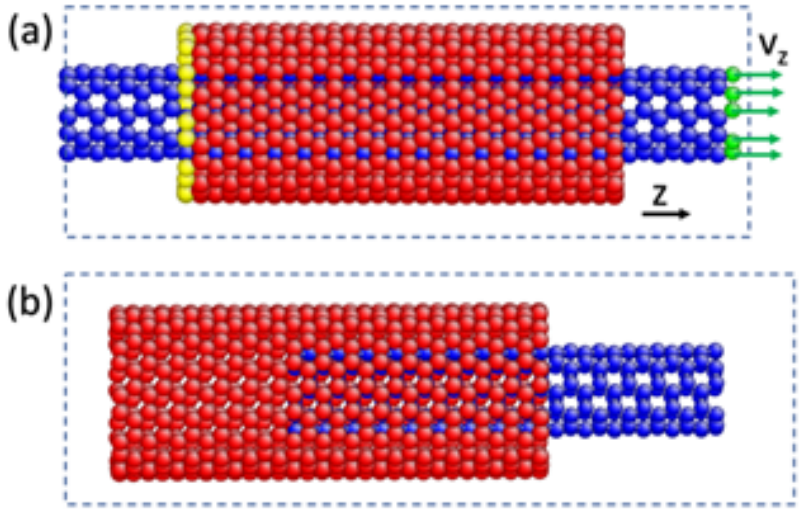

Figure 2.1. Schematics of the MD setups used to (a) measure $F_{friction}$ (Setup 1) and (b) to simulate the oscillating motion in double-walled CNTs (Setup 2). In (a), one left ring of atoms (yellow) are fixed; desired velocities are applied to one right ring of atoms (green). The dashed lines indicate the PBC cells.

Our MD simulations are carried out with LAMMPS [39] and rely on

the standard empirical AIREBO potential among intra-tube atoms. [40] The corrugation effect is attributed mainly to the overlap of π orbitals located on different tubes. [34] To distinguish the possible impact of the interfacial corrugation on $F_{friction}$ we have also performed comparison simulations in which K-C was replaced by the L-J potential of AIREBO. Two simulation setups, used before [29–33] and presented next, were utilized in our investigation.

Figure 2.1a presents setup 1, which was used prior to the oscillator motion study. It is designed to measure $F_{friction}$ at a controlled velocity v_z, and to assess the possible role of the contact area. The inner CNT is placed under periodic boundary conditions (PBC). A velocity component v_z is imposed to one ring of atoms belonging to the inner tube to realize sliding. The outer CNT is shorter than the inner one, and thus in this configuration the sliding motion occurs under fixed contact area. After the initial relaxation, a ring of atoms of one end of the outer tube was kept fixed. As edges are expected to introduce additional friction by thermal vibrations, freezing is likely to inhibit this effect. The behavior of the two edges becomes non-equivalent during the unidirectional sliding motion of the inner tube. Therefore, we have considered simulations in which the frozen ring of atoms was located on both left and right edges. However, we noted that the $F_{friction}$ values (cumulating edge and potential contact area contributions) obtained by fixing a ring of atoms on one side or the other are similar. This

observation suggest that the edge effect is dominated by the atoms of the inner CNT that are located in a potential vdW well induced by the outer tube. [13] All the other atoms are evolved in time in the canonical ensemble. Temperature is kept at 300 K with the help of a Nose-Hoover thermostat. Simulations were conducted for 100 ps in order to achieve steady state, after which $F_{friction}$ was measured over the subsequent 900 ps. Reported $F_{friction}$ represents the averaged net axial force exerted onto the outer CNT.

Setup 2 (Figure 2.1b) is the nanomechanical oscillator in its simplest form. It consists of a double-walled CNT where the inner tube can move inside the outer tube in an oscillatory motion of high frequency. At the atomistic level, this motion is induced and maintained by vdW interactions between the inner and the outer tubes. The inner tube is first pulled out by a certain distance to create new inner and outer surfaces. A Noose Hoover thermostat is applied for the first 10 ps to keep the CNTs at 300 K. During this process, the centers of mass of the CNTs are kept fixed to prevent the restoring motion that maximizes the vdW energy. While maintaining the relative positions of CNTs, for the next 10 ps we turned off the thermostat and switched to the microcanonical ensemble, Finally, we allow the created 'zero input' system to evolve in the microcanonical ensemble without constraints and track in time the distance z between the centers of mass of the two CNTs.

2.3 Results and Discussion

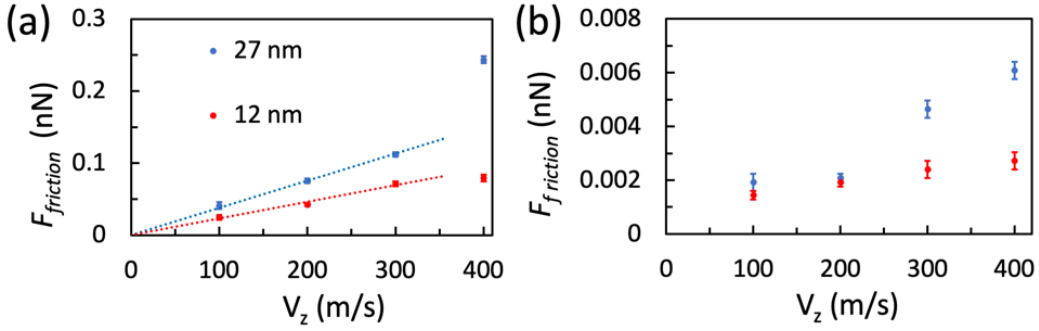

Figure 2.2. $F_{friction}$ vs. v_z for (5,5)(10,10) CNTs based on (a) K-C and (b) L-J inter-tube potential. All inner CNT lengths are $30nm$. Outer CNT l are $12nm$ and $27nm$. Dotted lines are linear fits up to $v_z = 300m/s$.

With setup 1 we have simulated two commensurate systems, (5,5)(10,10) and (9,0)(18,0), and a incommensurate one, (9,0)(15,5). Figures 2.2a and 2.2b present the obtained v_z dependence for the (5,5)(10,10) CNT case with both KC and L-J treatment of the inter-tube interactions, respectively. Comparing the K-C and L-J -described magnitudes of $F_{friction}$, it is evident that the inter-tube corrugation effect is important as it brings orders of magnitude differences. Figure 2.2a further indicates a linear dependence for $F_{friction}$ up to $\sim 300m/s$ velocities. The differences in slopes of $F_{friction}$ vs v_z lines at the two 'sleeve' lengths l suggest also a dependence on the contact area $2\pi rl$, as $F_{friction} = 2\pi r(l + e)\gamma v_z$. Here $r = 6.8\mathring{A}$ is the radius of the outer CNT, e a parameter that accounts for edge

effects, and γ is the viscous friction coefficient per unit area. Fitting to the two linear dependences of Figure 2a gives e=107 $\mathring{A}$ and $\gamma = 2.34 * 10^{-3} pNps/\mathring{A}^3$.

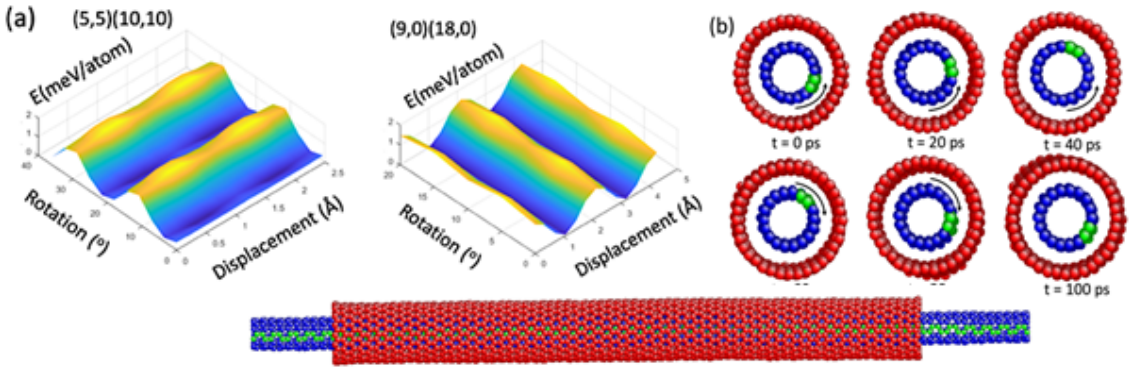

Figure 2.3. (a) K-C interlayer energy vs. axial relative rigid displacement and rotation for infinitely-long (5,5)(10,10) and (9,0)(18,0) CNTs. (b) Axial view of (9,0)(18,0) CNT at selected MD times. The marker (green) rows, visible in the side view below, reveal the rotation of the inner CNT during sliding. The inter-tube treatment is K-C.

The $F_{friction}$ values listed in Table 2.1 shows that that the differences between K-C and L-J results are maintained in (9,0)(18,0) as well as (9,0)(15,5) CNTs. Let's now focus on the K-C results. The CNTs compared in Table 2.1 have similar diameters and inter-tube gaps. The 'sleeve' l are $\sim 20nm$, while the inner CNT length are $\sim$ 30 nm in all cases. Therefore, any differences in $F_{friction}$ should largely reflect commensuration. In commensurate interfaces, atoms are able to simultaneously lock into registry and creep away largely in phase from the

CNTs	(5,5)(10,10)	(9,0)(18,0)	(9,0)(15,5)
$\Delta r(\mathring{A})$	3.31	3.42	3.42
K-C: $F_{friction}(pN/atom)$	0.014	0.362	0.006
L-J: $F_{friction}(fN/atom)$	0.3	0.3	0.2

Table 2.1. $F_{friction}$ for (5,5)(10,10), (9,0)(15,5), and (9,0)(18,0) CNTs with K-C and L-J potentials when v_z =100 m/s and $l \sim 20nm$. The differences in inner and outer radii Δr are also given.

local free energy minima described with the K-C model potential. The creep out motion releases the elastic energy stored by the stiff sp^2 bonds [41] into thermal energy. Both (5,5)(10,10) and (9,0)(18,0) CNTs have short axial and angular periods and present relatively large ($\sim 1meV/atom$) disparity in the corrugation against sliding and rotation. [35] $F_{friction}$ experienced by the zig-zag system turns out to be one order of magnitude larger than the armchair case. This result can be comprehended based on the inter-tube energy map of Figure 2.3a, which shows indeed a significantly larger barrier for the axial displacement (rotation) in the zig-zag (armchair) CNT. In the snapshots presented in Figure 2.3b, it is interesting to note that the sliding of the inner (9,0) CNT bifurcates into an additional spinning motion. This kinetic effect, present in the incommensurate but not in the armchair case, is evidently fostered by the already noted disparity in

the local energy barriers for rotation. Due to the larger barriers for displacement, atoms are more likely to creep away from their current local free energy minima by rotation. The large CNT shear moduli, [22] which associates significant strain energy penalty to differential twist drives the rotation of the atoms which are not located under the 'sleeve'. In the incommensurate (9,0)(15,5) CNT, interface atoms effectively sample more locations in the K-C potential environment at once, averaging out of the registry-dependent interactions.The net result is that the (9,0) CNT experiences little potential energy change ($\sim$0.1 meV/atom) upon sliding and rotation, and therefore less friction in comparison with the two commensurate cases. From the last column of Table 2.1, it is evident that accounting for this effect is important as $F_{friction}$ is an order of magnitude larger than in the L-J case.

The simulations with setup 2 obtained that the oscillatory motion, monitored in the z vs. time t plots in Figure 2.4a-c for the same set of CNTs with $l = 30\mathring{A}$, is significantly more damped in with K-C than with the standard L-J description (continuous black line). Note that z(t) for (9,0)(18,0) CNT computed with L-J is not shown as it is overlapping with the one for (9,0)(15,5) CNT. In order to limit the $F_{friction}$ dependence on v_z to the linear regime, we have considered relatively small initial pull out length $z(0) = 30\mathring{A}$. This initial condition was sufficient for triggering underdamped GHz oscillations in (5,5)(10,10) and (9,0)(15,5)

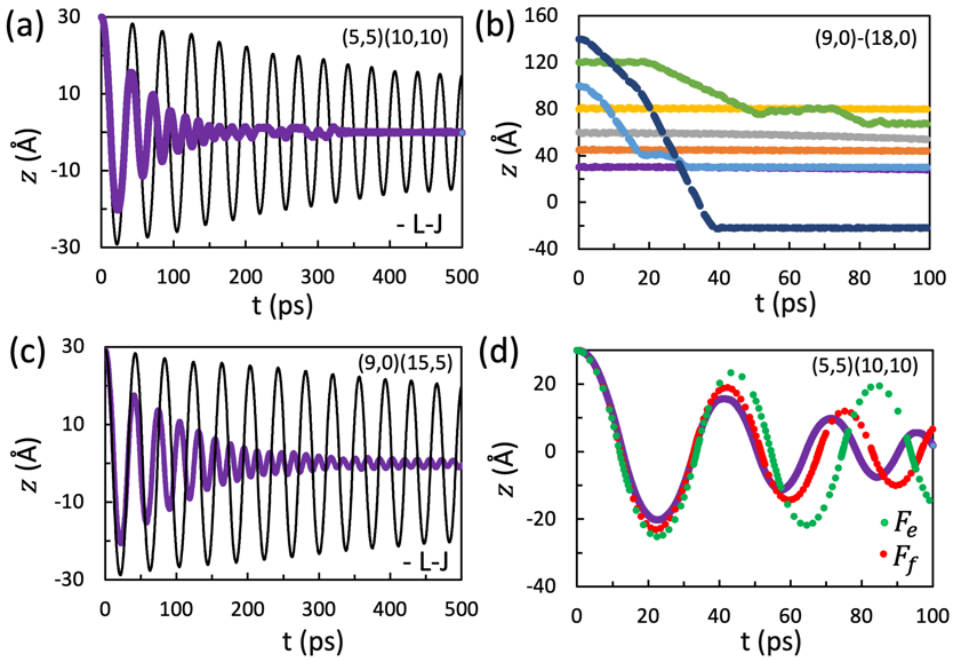

Figure 2.4. Time evolution of z in (a) (5,5)(10,10), (b) (9,0)(18,0), and (c) (9,0)(15,5) CNT oscillators. (d) MD and numerical solutions of eq. (1) with two $F_{friction}$ models. All unlabeled curves are obtained with K-C.

CNTs but not in (9,0)(18,0) CNTs. In Figure 2.4b, it can be seen that pullouts as large as 140$\mathring{A}$ are needed to trigger overdamped oscillations. Analysis of the MD animation also revealed a spontaneous excitation of the spinning motion during sliding, similar with the observations with setup 1. Overall, the trends in the damping of the telescopic motion are fully consistent with the trends in $F_{friction}$ obtained with setup 1.

To further illustrate the impact of the contact area dissipation during

the telescopic motion, we have attempted to describe the dynamics of (5,5)(10,10) CNT with a lumped-model idealization [33, 41]

$$m\ddot{z} + F_{friction}sgn(\dot{z}) + sgn(z)F_{vdW} = 0 \qquad z(0) = 30\mathring{A} \tag{2.1}$$

Here the dot notation is the time derivative of the displacement variable. The vdW force parameter F_{vdW}, calculated as 720 pN in modulus, is the absolute value of the derivative with z of the vdW energy between the concentric CNTs with z, while $m = 9928amu$ is the reduced system mass. [41] We have solved numerically Equation 2.1 with two models for the dynamic friction $F_{friction}$, one accounting only for the edge, $F_e = 2\pi re\gamma z$, and the other fully accounting for both edge and contact area, $F_f = 2\pi r(l - z + e)\gamma z$. We have used the e and γ values determined previously with setup 1. In the comparison shown in Figure 2.4d, it can be seen that the numerical solution of the Equation 2.1 with $F_{friction} = F_f$ follows more closely the MD solution based on the K-C potential. The agreement with MD is obviously imperfect, likely due to the non-linear variation of $F_{friction}$ with v_z (since v_z reaches $\sim 400m/s$) and differences edge effects in the two MD setups. The $F_{friction} = F_e$ solution is closer to MD based on L-J.

The different rates of the amplitude decay of the (9,0)(15,5) oscillator obtained with the K-C and L-J descriptions is intriguing considering the incommensurate character of the interface. For more insight into this behavior, in Figure

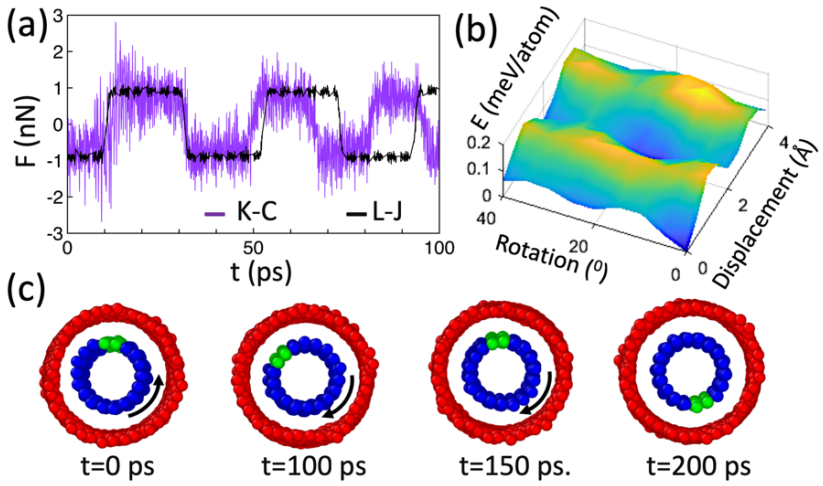

Figure 2.5. (a) The relative force between the inner and the outer tube for the (9; 0)(15; 5) oscillator descried with K-C and L-J. (b) K-C interlayer energy vs. axial relative rigid displacement and rotation. (c) Axial view at selected MD times. The marker (green) atoms reveal the rotation of the inner (9,0) CNT during sliding. The inter-tube treatment is K-C.

2.5a we plot the relative force F between the tubes projected onto their common axis in the two descriptions. In the absence of friction, F would be a piece-wise constant [25, 26]. With L-J, MD gives small and relatively constant oscillations around the piece-wise solution of F. With K-C, there are large F oscillations, which are due to the still-present corrugation and energy barriers to axial sliding, Figure 2.5b. These oscillations are largest close to the 10 ps time, where there is maximum overlap and force changes sign, and appear to maintain a somewhat

lower amplitude at later oscillating cycles. This observation suggests a change in the inter-tube potential landscape with each oscillation. Indeed, as it can be seen in the simulation frames of Figure 2.5c, the inner CNT undergoes large rotational self-excitations as a way to avoid the crossing of the larger axial barriers, Figure 2.5b.

2.4 Conclusions

MD simulations of concentric CNTs based on a K-C model potential bring fresh evidence to support the dependence of the dynamical friction on contact area and commensuration. Stick-slip and superlubric behaviors might not be particular to graphene, [42] and considerations on commensuration are important for guiding the design of CNT oscillators with minimal dynamic friction attributes. It also points out for the need to develop ways to sustain the oscillatory motion, perhaps by a selective generation of coherent phonon modes with ultrafast laser pulses. [43]

Chapter 3

Nanofriction between Cylindrical and Collapsed Carbon Nanotubes

In this chapter, we first discuss the measurement of friction between cylindrical CNTs and damping parameter calibration in the mDEM model. Next we present the characteristics of the sliding friction in large-diameter collapsed carbon nanotubes (CNTs) as emerged from molecular dynamics simulations. The friction force is found to depend strongly on the CNT sliding velocity, the interface area, interface commensuration, and temperature. The non-classical smooth sliding and superlubric behaviors identified at the molecular level give a useful starting reference to the ongoing efforts aimed at engineering the mechanical load transfer in material systems comprising collapsed CNTs. This work has been

published in Ref [20] and Ref [18].

3.1 Introduction

Carbon nanotubes (CNTs) [21] have outstanding physical properties including very high elastic modulus and tensile strength [1], and high electrical and thermal conductivities [4–6]. Commercial methods produce a buckypaper soot-like CNT material containing also impurities in the form of catalyst nanoparticles [44]. A critical problem hindering applications is the processing of the as produced material into yarns and sheets comprising highly aligned CNTs so that the outstanding properties of individual CNTs can be more effectively utilized for developing diverse applications, including super-lightweight aerospace structures, artificial muscles, energy storage and generation devices [45, 46]. Sliding friction between CNTs has a huge impact on the load transfer during the yarn formation process. In section 3.2, we describe MD simulations and mDEM calibrations to obtain the viscous and local damping parameters for cylindrical (10,10) CNTs.

Section 3.3 and 3.4 focuses on collapsed CNTs. Recent atomic-resolution transmission electron microscopy on the stretched sheets found the massive presence of collapsed CNTs, which were alligned, packed, and free of catalyst particles.

The achieved high-concentration of aligned CNTs is interesting for the development of superstrong composites, anticipated to compete with carbon fibers [8]. Nevertheless, conceiving a good load transfer between CNT structural units will be essential in this endeavor. So far, the carbon nanotribological studies have focused on C_{60} [47], concentric CNTs [48–51], graphene [48, 52, 53], and graphene nano scrolls [54], and the knowledge of the friction at the collapsed CNT interfaces is still missing. To uncover the characteristics of the sliding friction, we make recourse to classical molecular dynamics (MD) simulations of collapsed CNTs stacked in bundle arrangements similar with the ones observed in experiment [55].

3.2 Damping calibration of cylindrical (10,10) CNTs

First, we focus on characterizing the nanofriction developed between two (10,10) CNTs in vdW contact. MD simulations were performed with LAMMPS [56] and rely on the K-C vdW potentials [57] among inter-tube CNT atoms and standard AIREBO potentials [58] among intra-tube CNT atoms. The use of the KC potential is particularly important for characterizing the sliding friction since this potential captures the registry-dependent corrugation between armchair

cylindrical CNTs [59].

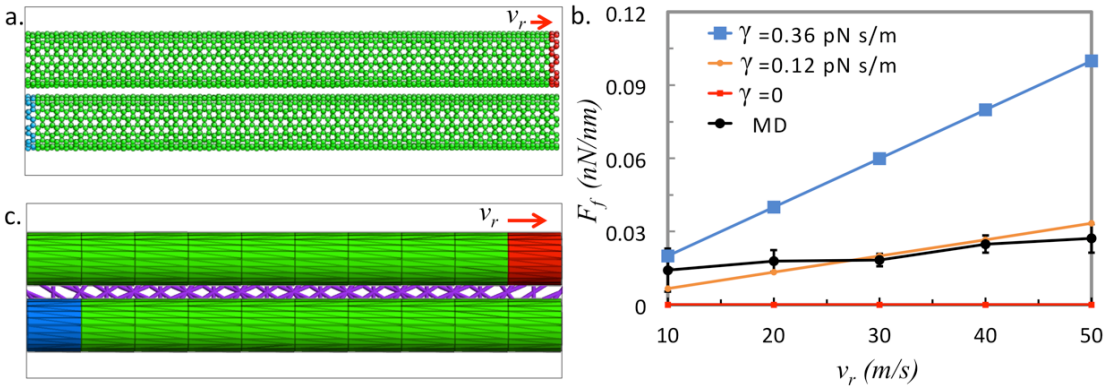

Figure 3.1. (a) MD setup used to compute dynamical friction between two aligned (10,10) CNTs. The desired sliding velocity is imposed to the one unit cell "ring" and one distinct element (red) belonging to the upper CNT. One unit cell "ring" and one distinct element (blue) belonging to the lower CNT is at rest. (b) F_f (per unit length) vs. v_r. MD data (black circles) shows smooth sliding. (c) mDEM setup used to calibrate mesoscale friction. The purple lines indicate the vdW contacts between distinct elements located on the two CNTs.

The MD setup consists of two aligned (10,10) CNTs each 13.6 nm in length placed under periodic boundary conditions (PBC), Figure 3.1(a). Because the periodicity is kept large in the transversal directions, the two (10,10) CNTs have only one surface in vdW contact.

After carrying out initial relaxations, a one-unit ring belonging to bottom CNT is kept fixed to prevent the motion of its center of mass. Velocity v_r controlled

sliding is realized by imposing a desired v_r along the CNT axis to a one-unit ring belonging to top CNT. Note that because of the imposed PBC, no new vdW surfaces are created during sliding. All unconstrained atoms are evolved in time in the microcanonical ensemble corresponding to an average temperature of 300 K. The friction force F_f measurements are carefully done after 100 ps time, in order to allow for equilibration after the initial acceleration period. The measured v_r is the net vdW force exerted onto the upper CNT projected onto its axis, averaged over the subsequent 500 to 3,000 ps. During averaging, the instantaneous temperature increases only up to 350 K. We considered v_r as low as 10 m/s in order to approach the regime of the conventional pulling velocity exerted on materials.

Our simulations summarized in Figure 3.1 uncover a v_r dependent nanofriction, which differs from the velocity-independent friction of the macroscopic scale. We expect that the MD-computed room-temperature F_f will decrease with increasing temperature [60]. Nanofriction depends on the contact interface area [39, 40]. In this respect, we find that F_f between cylindrical (10,10) CNTs (for example $F_f = 0.014 \pm 0.001 nN/nm$ at $v_r = 10 m/s$) is an order of magnitude smaller than F_f computed for collapsed (35,35) CNTs (for example $F_f = 0.28 \pm 0.06 nN/nm$ at $v_r = 10 m/s$) [40], which present a much larger contact area.

Second, we focus on MD simulations aimed at determining the relaxation timescales for the spontaneous zipping process. Since in the network environment,

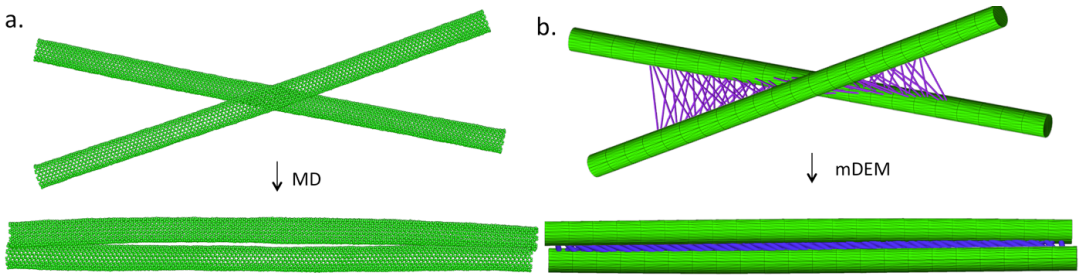

Figure 3.2. (a) MD setup used to compute the relaxation time of two crossed (10,10) CNTs each 30 nm in length. (b) mDEM setup used to calibrate the crossing relaxation at the mesoscale. The purple lines indicate the vdW contacts between distinct elements.

an individual CNT crosses with a number of other CNTs, the zipping relaxation occurs rather locally, over small CNT portions. Thus, our simulations focused on zipping of short CNTs. Figure 3.2a shows the MD setup in which two (10,10) CNTs, first equilibrated at room temperature, are placed in a crossed configuration. At the crossing point, the minimal wall-to-wall distance is 0.5 nm [13]. Due to the long-range vdW inter-tube forces, the two CNT align spontaneously with a coherent motion under velocity Verlet dynamics, forming the bundle shown at the bottom. The measured zipping relaxation times function of the initial crossing angle are recorded in Table 3.1.

Calibration of viscous damping γ and local damping α parameters of the mDEM is based on the atomistic level behavior obtained above. Since local

damping produces a negligible dynamic nanofriction [13], we first train γ to the MD data and next adjust α to reproduce the zipping relaxation times of crossed CNTs. Figure 3.1c shows the parallel mDEM realization of the sliding simulation setup, which comprises two CNTs each represented by 10 mesoscopic elements. The system is placed under PBC, and velocity-controlled sliding is imposed in the same manner as in MD. mDEM simulations were performed under different γ values. As it can be seen in Figure 3.1b, the v dependent room temperature phononic friction revealed by MD is best matched in mDEM with $\gamma = 0.12pNs/m$. Figure 3.1b also confirms that the mesoscale friction force is practically vanishing when $\gamma = 0$. This result insures that the numerical damping plays a negligible role in the mesoscopic friction. At the same time, this result demonstrates that accounting for vdW adhesion alone is not sufficient to capture the dynamical friction at the mesoscale.

In Table 3.1, we see that the numerical damping parameter $\alpha = 0.4$ matches the MD zipping relaxation times with a 5 ps precision. Due to significantly reduced degrees of freedom, the undamped ($\gamma = 0$) simulations leads to relaxation times shorter than in MD, Table 1 last column.

Crossing Angle	Zipping Time (ps)		
	MD	mDEM $\gamma = 0.12(pNs/m)$	mDEM $\gamma = 0$
30°	50	55	40
45°	140	144	118
60°	220	216	180

Table 3.1. Computed zipping relaxation time of two crossed (10,10) CNTs each 30 nm in length. In the mDEM simulation results of the last two columns, we selected $\alpha = 0.4$.

3.3 Friction between collapsed CNTs

Similar with our friction measurement of cylindrical CNTs, we performed a more systematic study of the nanofriction between collapsed CNTs. MD simulations were carried out with LAMMPS [56] and rely on standard empirical AIREBO potentials among intra-tube CNT atoms [58] and the K-C (vdW) potentials among inter-tube CNT atoms [57].

To prepare the collapsed CNTs, a Nose-Hoover thermostat was used initially to equilibrate the cylindrical CNTs at 5K. After the system reached equilibrium, a 0.01eV/atom force was added in the transverse direction for 15 ps to squeeze the structure. The system was then freed in the transverse direction and

equilibrated again under microcanonical ensemble for another 500 ps. Periodic boundary conditions (PBC) were applied in the axial direction throughout the whole process. In the end, we used conjugate gradient relaxation to relax the collapsed structures at 0K. The structures remained collapsed during the subsequent MD friction studies.

To study friction, we employed MD setups consisting of three (Figure 3.3a) and four (Figure 3.3b) collapsed CNTs placed under PBC. These setups allow to investigate the sliding of CNT1 in vdW contact with CNT2 (Figure 3.3a), and CNT2 and CNT2′ (Figure 3.3b). After carrying out an initial conjugate gradient relaxation of the CNTs system, a one-unit ring belonging to CNT3 is kept fixed to prevent the motion of its center of mass. CNT3 is linked to CNT2 and to CNT2′ by twenty sp-type covalent cross-links, which are created by adding ten interstitial atoms. Note that in Figure 3.3b, CNT3 and CNT2′ are cross-linked by PBC. Before the production runs, the system was equilibrated for an initial 10 ps at the desired temperature imposed on the system using Nose-Hoover dynamics. Next, velocity v controlled sliding is realized by imposing a desired v to a one-unit ring belonging to CNT1. A Nose Hoover thermostat is applied during MD to the unconstrained atoms. The friction force F measurements are done after 100 ps MD time, in order to allow for equilibration after the initial acceleration period. The reported F is the net vdW force exerted onto CNT1 projected onto its axis,

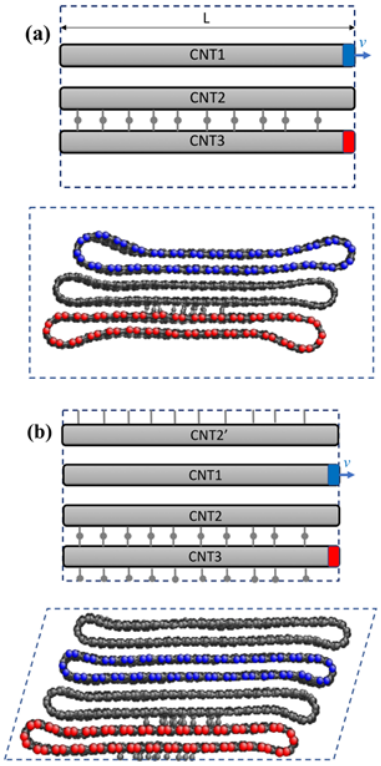

Figure 3.3. Schematics (side views) and atomistic models (axial views) for the MD setups with (a) three and (b) four collapsed CNTs in the computational cell. Velocity is imposed to the one-unit cell "ring" (blue) belonging to CNT1. One-unit cell ring (red) from CNT3 is kept fixed. The vertical lines between CNT3 and CNT2 (and CNT2′) indicated the introduced cross-links. The dashed lines indicate the (a) rectangular and (b) triclinic periodic boundary conditions. Note that in (a) the vertical periodicity is large so CNT1 and CNT3 are virtually non-interacting by vdW.

averaged over the subsequent 500 to 10,000 ps.

An alternative way to the direct measurement is to extract F from the energy balance $\Delta Q = Fvt$. Here ΔQ is the kinetic energy extracted from the reservoirs, t is the sliding time. In Figure 3.4 we plot ΔQ vs. vt computed from the MD simulations of (30,30) collapsed CNTs with $L = 13.6nm$ sliding with $v = 100m/s$ at room temperature. With this energy method, we obtain $F = 7.58eV/\mathring{A}$, in good agreement with the direct force measurement of $7.52eV/\mathring{A}$ or $.89nN/nm$. Additionally, we emphasize that the role of the 20 added cross-links in our MD setups is to constrain the sliding of CNT2 and CNT2′. The reported results are converged with the number of cross-links. For example, in the above example, with 20 cross-links we measured $F = 0.89 \pm 0.12nN/nm$, while with 16 cross-links is $F = 0.88 \pm 0.12nN/nm$.

Previous MD studies [49] on dynamical friction in oscillating CNTs obtained relative v in the range of $120m/s$ to $790m/s$, depending on the magnitude of the oscillations. These MD simulations give an indication of the v values that could be expected during the mesoscale CNT sliding processes occurring during the spontaneous CNT film formation. In addition to considering such a high v regime, we also lowered v up to $10m/s$ in order to approach the regime of the conventional pulling velocity exerted on materials. The MD setups of Fig. 3.3 are selected because they are robust to the thermostat location, and eliminate

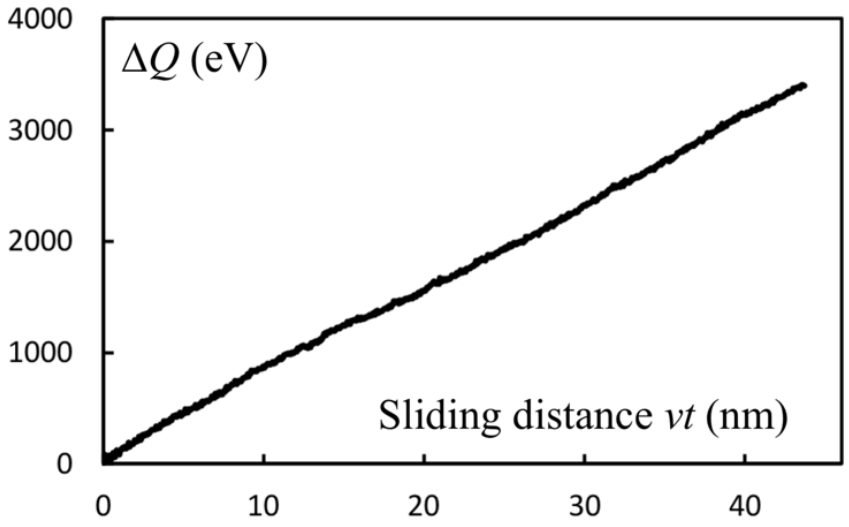

Figure 3.4. The energy extracted by the thermostats ΔQ vs. sliding distance vt in the three- (30,30) collapsed CNT setup at room temperature. Here $v = 100m/s$.

large F peaks at selected v, observed in a two-CNT setup (Figure 3.5). In Figure 3.5a, we are showing a simpler two collapsed CNT setup, which was used in the early stages of this work. As shown in Figure 3.5b, this setup gives large frictional peaks at selected sliding speeds, such as v=350 m/s.

With two-CNT setup, we observed that the corresponding velocities where peak F exists have a linear dependence on the inverse of our selected tube length $1/L$. Phonon density of state (DOS) analysis was carried out next. While Fourier transforming the velocity-velocity correlation function, by merely considering longitudinal component and transversal component of velocities, respectively,

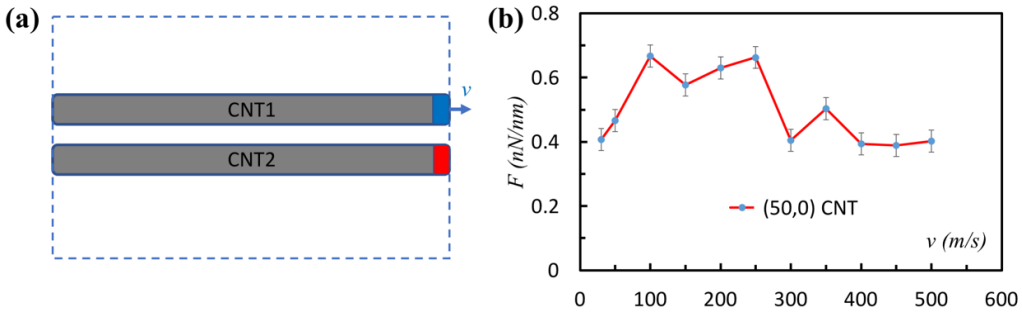

Figure 3.5. (a) Schematics (side view) for the MD setup containing two collapsed CNTs in the computational cell. (b) The computed F vs. v presents peaks at selected v.

we obtained large longitudinal and transversal DOS at the previously identified peak velocities. The frequencies of these excited modes also depend linearly on $1/L$, thereby proving a correlation between these excited vibration modes at the selected pack velocities. Stronger vibrational excitations can also be observed at the peak velocity in comparison with sliding at non-peak velocities. We have identified that the modes are standing waves created in CNT2 by fixing the ring of atoms (marked in red) in order to prevent the motion of its center of mass. In the three- and four- CNT setups of Figure 3.3, this is accomplished instead by cross-linking CNT2 and CNT2′ with CNT3. CNT3′ motion of its center of mass is prevented. In these slightly more complex setups we can successfully avoid the excitation of these peak modes and are able to provide representative measurements

of the friction force.

Note that friction enhancement at selected v have been reported in the sliding of coaxial cylindrical CNTs [51]. Additionally, any stretching or breaking of the interstitial bonds give an indication on the load transfer.

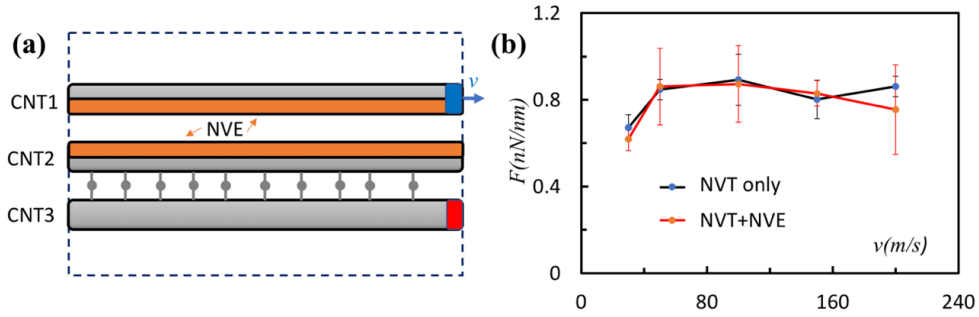

Figure 3.6. (a) Schematics (side view) for the MD setup containing three collapsed CNTs in the computational cell. Unlike in the set-up described in Fig.3.3a of the main paper, the interface atoms between CNT1 and CNT2 are evolved in the microcanonical ensemble (NVE). (b) Comparison between the F computed with the set-up used in the main paper (NVT) and the combined NVT+NVE set-up described in (a).

To validate that thermostat doesn't compromise our results, in Figure 3.6 we demonstrate an alternative three-collapsed CNT setup in which the vdW contacting orange (non-contacting gray) faces of CNT1 and CNT2 were evolved in the microcanonical (canonical) ensemble, Figure 3.6a. As demonstrated in Figure

3.6b, the friction forces computed this way have similar magnitudes with the MD set-up used in Figure 3.3.

3.4 Results and discussions

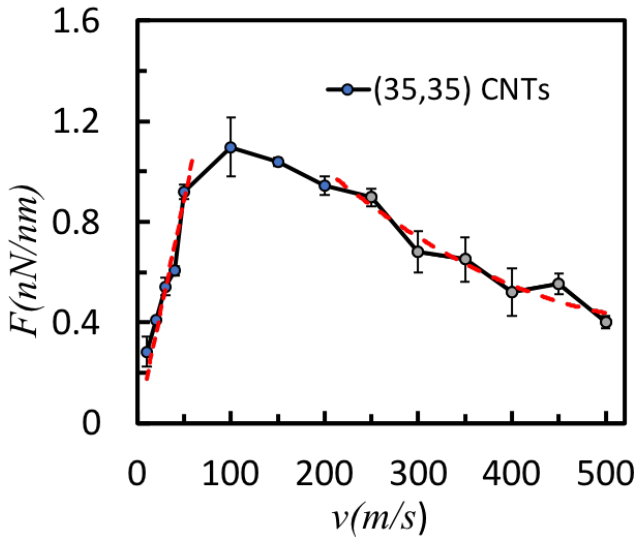

Figure 3.7. F (per unit length) vs. v for (35,35) collapsed CNTs. Dashed (red) lines are trend lines. Results were obtained with the three-CNT MD setup.

We recently reported a low rate of thermal energy dissipation at the vdW interfaces of collapsed CNTs [61]. Focusing here on relative motion, we uncover a v dependent mechanical energy dissipation reflected by a complex dependence of F on v. This behavior differs from the classical v-independent F of the macroscopic scale. Figure 3.7, which summarizes our MD results obtained in the three (35,35)

collapsed CNT setup, reveals in fact three contiguous F regimes: (i) linear smooth sliding ($v < 80m/s$), (ii) peak $80 < v < 250m/s$), and (iii) weakening ($250 < v < 500m/s$). In Figure 3.9a, a similar behavior can be observed in the room temperature sliding of (50,0) collapsed CNTs. Both simulations are examples of commensurate configurations as the ratio of their unit cell sizes is 1. We relate next these F regimes to the popular Prandtl-Tomlison (PT) model of the damped motion of an atom driven over the external periodic potential by means of a spring [62].

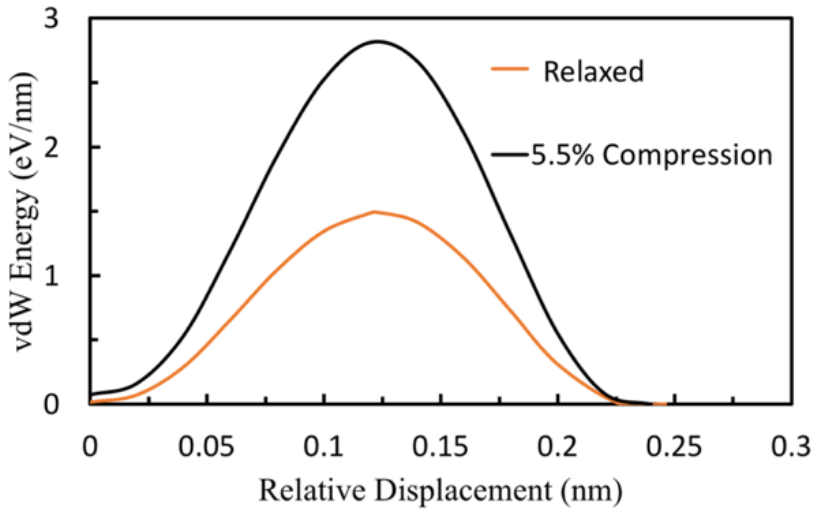

Figure 3.8. (Variations of the static inter-tube van der Waals energy (measured from the most favorable stacking) at the (35,35)-(35,35) collapsed CNT interface under relative axial sliding. Both the relaxed and 5.5% compressed cases are shown.

Despite the relative weakness of the vdW binding, we expect important energy corrugation U at the collapsed CNT interfaces. This is because layer stacking arrangements, where the carbon atoms do not eclipse the each other's p_z orbitals, Figure 1.3a, are most favorable. Indeed, for the commensurate example of Figure 3.3, we measured $U = 1.5eV/nm$, Figure 3.8. In the low v regime, the thermal motion of atoms plays an important role in helping CNT creep out from these energy barriers. As in the PT model [62], the creep out motion results in release of the elastic energy stored in the intratube sp^2 bonds into thermal energy. In agreement with our MD results for $v < 80m/s$, PT predicts smooth sliding when there is a large disparity between the strengths of the atom-external potential (vdW bonding here) and the spring constant (intratube sp^2 bonding here). Next, the peak F regime indicates that the timescale for the thermal creep becomes negligible in comparison with the competing transport timescale a/v. Here, $a = 0.24nm$ is the corrugation periodicity. Finally, the F weakening obtained as v is approaching the thermal speed of carbon atoms ($790m/s$ at room temperature) can be attributed to the decrease in the energy dissipation when interfacial atoms have less time to release their kinetic energies before the next barrier jump.

According to Krim [63], the phononic contribution to the smooth sliding $F = \gamma v$ should be sensitive to the contact interface area A and crystallographic

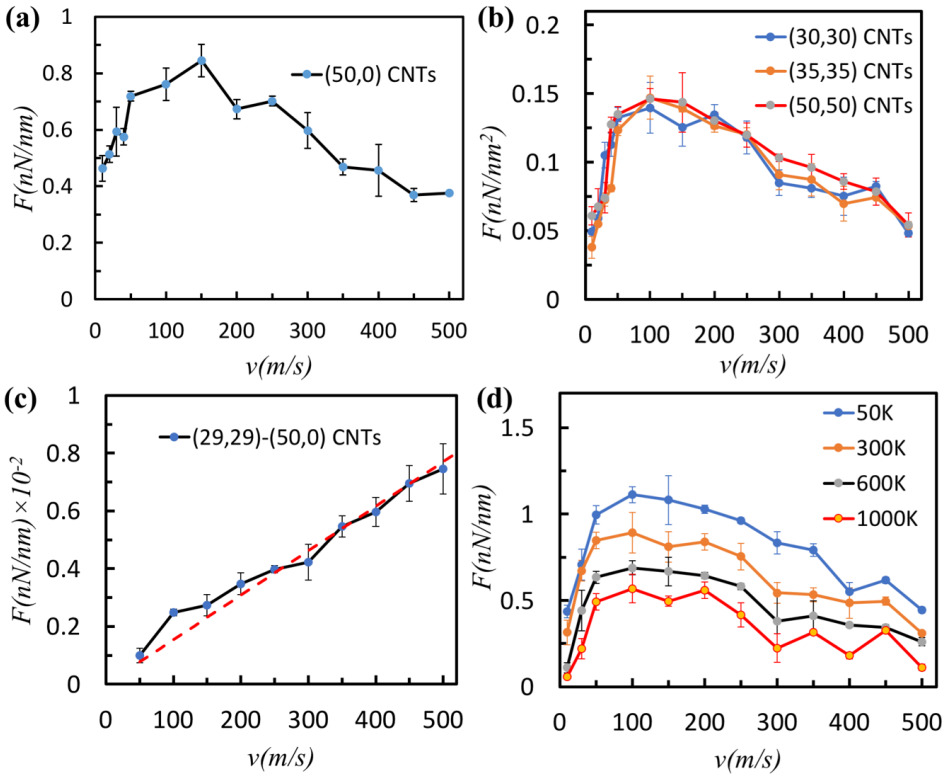

Figure 3.9. MD results with the three-CNT MD setup. (a) F (per unit length) vs. v for (50,0) collapsed CNTs. (b) F (per contact area) vs. v for collapsed armchair CNTs of different widths. The interface contact area A is $81.5nm^2$, $96.3nm^2$, and $138.4nm^2$ for (30,30), (35,35), and (50,50) collapsed CNTs, respectively. (c) F (per unit length) vs. v at the interface of (29,29) and (50,0) collapsed CNTs. In (a)-(c) $T = 300K$. (d) F (per unit length) vs. v for (30,30) collapsed CNTs at different T.

commensuration, via $\gamma = \alpha A U^2$. Here γ is the coefficient of friction while parameter α captures the temperature T dependence. Previous MD on concentric cylindrical CNTs found F to be independent on A and commensuration [50]. On the contrary, in collapsed CNTs we find that F is very sensitive to A,U and T. First, (i) Figure 3.9b shows that F/A vs. v data for (30,30), (35,35) and (50,50) collapsed CNTs falls onto a single curve, when A is approximated as $A = wL$. Here, w is the width of the collapsed CNTs in vdW contact, and $L = 13.6nm$ the length of the translational periodicity. For the linear regime, our MD gives $\gamma/A = 2.9nNps/nm^3$. Second, (ii) Figure 3.9c considers the dynamic sliding at the (29,29)-(50,0) collapsed CNT incommensurate interface (periodicities ratio $1/\sqrt{3}$). Here $L = 6.4nm$ in order to closely match the periodicities of 26 (29,29) CNT units and 15 (50,0) CNT unit cells. During MD, the collapsed (29,29)-(50,50) CNT interface stays incommensurate, i.e., it doesn't develop local portions with matching lattice constants. Since these two CNTs have similar widths, the reduced friction relative to the results reported in Figure 3.9c can be attributed to the vanishing corrugation under crystallographic mismatch. The substantial reduction of friction relative to the commensurate case, caused by incommensurability is called superlubricity [48]. Third, (iii) Figure 3.9d shows F decreasing as T increases, and that the three F regimes for commensurate sliding are preserved at all T. In the PT model, the decrease of F with T is due to the increased influence of

thermal activation on the barrier jumping process. Our MD showed that the bond length fluctuations of the CNT2-CNT3 cross-links are virtually independent from v. Such poor load transfer at the collapsed CNTs represents a potential culprit for material underperformance. Increasing load transfer, for example by polymer addition, will be critical for fulfilling the CNT's potential as building blocks of ultrastrong materials. In this quest, MD could be useful for making predictions about the frictional attributes of diverse polymer-coated CNTs. Since at this level of MD complexity, it is often more convenient to enforce full PBC, we have tested as a preliminary step, the transferability of our results to the four-CNT MD setup (Figure 3.3b). In (35,35) collapsed CNTs, our computed F of $1.56 \pm 0.07 nN/nm$ at $v = 50 m/s$ is nearly twice as large than F of $0.85 \pm 0.05 nN/nm$ computed with setup of Figure 3.3a. Furthermore, the four-CNT setup also allows to compute F under applied lateral pressure. Our MD simulations under 5.5% compression measured $F = 1.97 \pm 0.12 nN/nm$ at $v = 50 m/s$. This change reflects the increased of corrugation, from $U = 1.5 eV/nm$ to $U = 2.9 eV/nm$, as CNT faces are getting in closer contact, Figure 3.8. Finally, it is worth to stress out the important role of commensuration for the CNT mesoscale dynamics. With the setup of Figure 3.3a, the simulated zero-input microcanonical evolution of CNT1 under an initial $v = 50 m/s$ gave a stopping time of only 3 ps for the commensurate (30,30)-(30,30) collapsed CNT and about 400 ps for the (29,29)-(50,0) collapsed CNT case.

3.5 Conclusions

In summary, because of the important role played by contact area and commensuration, collapsed CNTs present frictional attributes more similar with graphene [53] than with cylindrical CNTs [50]. The commensuration dependence of F manifested in superlubricity, points out a critical weakness in these material systems, and gives a useful starting reference for the ongoing efforts aimed at improving the load transfer. The MD derived F can be used to inform coarse-grained mesoscopic models that can explicitly incorporate the CNT tribology [64, 65] and thus can be used to predict the spontaneous bundle formation and its mechanics with accounting for the CNT sliding. While the presented MD simulations considered vacuum between collapsed CNTs, the approach can be generalized to study the nanofriction at collapsed CNT interfaces in the presence of solvent or polymeric layers [66].

Chapter 4

Collapsed Carbon Nanotubes: From Nano to Mesoscale via Density Functional Theory-Based Tight-Binding Objective Molecular Modeling

Due to the inherent spatial and temporal limitations of atomistic modeling and the lack of mesoscale models, mesoscopic simulation methods for guiding

the development of super strong lightweight material systems comprising collapsed carbon nanotubes (CNTs) are missing. Here we establish a path for deriving ultra-coarse-grained mesoscopic distinct element method (mDEM) models directly from the quantum mechanical representation of a collapsed CNT. Atomistic calculations based on density functional-based tight-binding (DFTB) extended with Lennard-Jones interactions allow for the identification of the cross-section and elastic constants of an elastic beam idealization of a collapsed CNT. Application of the quantum treatment is possible due to the simplification in the number of atoms introduced by accounting for the helical and angular symmetries exhibited by twisted and bent CNTs. The modeling chain established here is suitable for deriving mesoscopic models for a variety of microscopic filaments with bending anisotropy. This chapter was published in Ref [19].

4.1 Introduction

Advances in carbon nanotube (CNT) synthesis have brought a new class of materials, which include large volume CNT sheets suitable for developing macroscale applications [8]. The sheet exhibits a network structure comprising partially-aligned and entangled large-diameter CNTs. Currently, there are significant efforts to manipulate the CNT orientation by mechanical and electrochemical

stretching of the CNT sheets [67]. During sheet stretching, the initially cylindrical large-diameter CNTs undergo not only partial alignment and bundling, but also permanent radial collapse to a dog-bone-shaped cross-section [68, 69]. The obtained collapsed CNT assemblies represent a promising material platform for developing super strong lightweight composite materials with mechanical attributes approaching those of individual CNTs [8,23,70]. In this quest, the guidance power of computational materials modelling is critical for understanding how materials properties are influenced by variations in structure at the mesoscale. Ideally one would like to simulate collapsed CNT assembles with all-atom simulation methods [71, 72], but this approach is computationally prohibitive. While large-scale mechanical behavior of materials is usually treated with continuum mechanics, simulation of the non-continuous response caused for example by the strain-induced relaxation of misaligned collapsed CNT bundles in a material with large void volume fraction, is not well adapted to the continuous description. Therefore, we are required to develop computationally efficient coarse-grained (CG) strategies, where the atomistic degrees of freedom are completely eliminated.

The dog-bone shape of the collapsed CNTs, Figure 4.1(a)-(b), is the outcome of the balance between the bending energy stored at the closed edges and the van der Waals (vdW) energy gained by bringing in close contact of the

flattened CNT walls [9, 10]. In the quest of developing a mesoscale representation, one possibility is to pursue the CG of each one-atom thick graphene wall using the Martini force-field [73] or a Tersoff bond-order potential [74, 75]. Such CG would capture the transformation from cylindrical to collapsed CNTs and therefore would be clearly needed if one would like to simulate the CNT stretching process [68, 69]. However, because the level of coarse-graining mapping is low (a few carbon atoms to 1 CG element) and the developed effective potentials must be supplemented with long-ranged Lennard-Jones (L-J) interactions in order to describe the important vdW gluing of the flat faces, this approach would be computationally ineffective. Since we are interested in resolving the representative mesoscale mechanics [76] of collapsed CNT assemblies, a more ambitious ultra-CG mapping (a few hundred carbon atoms to 1 CG element) capturing the carbon atoms in several unit cells is desirable. The development of such ultra-CG approach, which would capture implicitly into the effective potential the intra-tube vdW interactions, is supported by the observation that large diameter collapsed CNTs (above $\sim 4nm$ in the case of single-wall CNTs) are stable [77] (do not go back to the cylindrical shape) and therefore can be regarded as individual entities. Furthermore, the strong covalent connection between the flat multilayer graphene central region enabled by the closed round edges, make the interlayer shear response significantly less important than in multi-layer graphene with free edges.

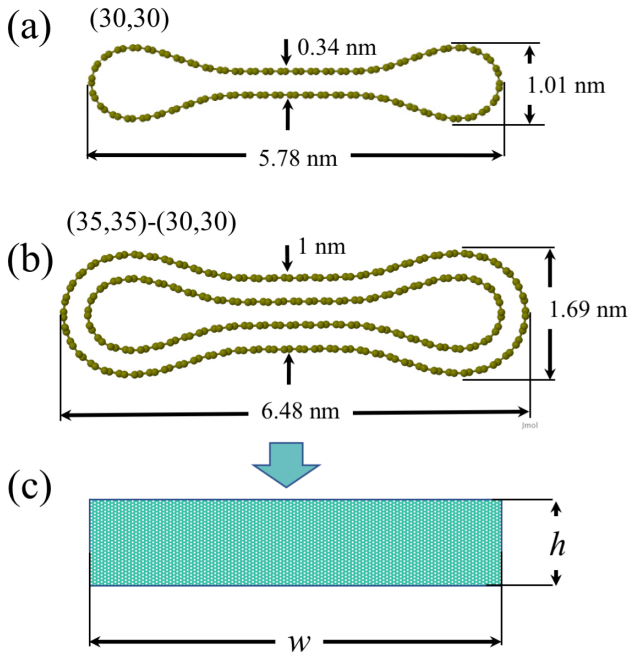

Figure 4.1. Cross section of the DFTB optimized (a) collapsed (30,30) single-wall CNT and (b) (35,35)-(30,30) double-walled CNTs. The number of carbon atoms N_o in the unit cells are 120 and 260, respectively. (c) Coarse grain "brick", representing carbon atoms in the unit cells.

While efficient ultra-CG methods for cylindrical CNTs have been already developed [76, 78–80], such models for collapsed CNTs are currently missing. As a key step in addressing this issue, here we delineate a hierarchical multiscale

chain in which objective molecular simulations [81] coupled with a quantum mechanical density functional-based tight-binding (DFTB) description of the interatomic interactions presented in Section 4.2, are used in Section 4.3.1 to uncover the nanomechanics of stretched, twisted, and bent collapsed single and double-walled collapsed CNTs. In Section 4.3.2, we transfer the obtained behavior to the meso-scale by developing a reduced-order mesoscopic distinct element method (mDEM) model consisting of a chain of rigid "brick" distinct elements, Figure 4.1(c), connected by parallel bond contacts [80]. In Section 4.3.3, the mDEM model is verified and validated for describing the important twisting and bending deformation modes. Finally, Section 4.4 presents our summary and conclusions.

4.2 Model and methods

Interatomic forces play a key role in establishing the shapes of the collapased CNTs resulted from the balance of bending strain stored one-atom thick hexagonal lattice and vdW adhesion. The selection of the interatomic potential is particularly subtle as the molecular mechanics of the commonly-employed bond-order potentials [74] describe bending strain differently [82]. As a result, the simulated nearly circular edges of the collapsed CNTs may present different shapes with different potentials [83]. Gao et al. [77] showed that force fields derived from

density functional theory supplemented with Lennard-Jones (LJ) interactions can describe the shapes observed in experiment. Since force fields are less appropriate for describing the potential breaking of the carbon-carbon bonds at the reactive close edges, here we adopt instead the a tight-binding model with parameters derived from density functional theory [84] (DFTB) extended with L-J interactions (energy parameter $\epsilon = 0.069 kcal/mol$ and the distance parameter $\sigma = 3.80 \mathring{A}$) similar with those used by Gao et al. [77]. While DFTB has been previously applied to collapsed CNTs [85–88], the focus was on CNT diameters less than the ones considered here. Moreover, we focus on simuations of collapsed CNTs under twisting, and bending deformations, Figure 4.2, which are enabled by the implementation of objective boundary conditions [81] into the code DFTB+ [89]. These boundary conditions are based on the concept of objective structures [90], and have been coupled [91] with DFTB in a manner that allows for the application of an arbitrary twist[88].

It is worth to compare the traditional ways of imposing twisting and bending deformations, with the same deformations imposed by subjecting the N_o atoms of the unit simulation cell to objective boundary conditions. Uniformly twisted CNTs have a translationally repeating cell size corresponding to the size of the helical motif described by the closed edges. Such a large number of atoms (a multiple of N_o) makes unpractical alternative DFTB calculations adopting

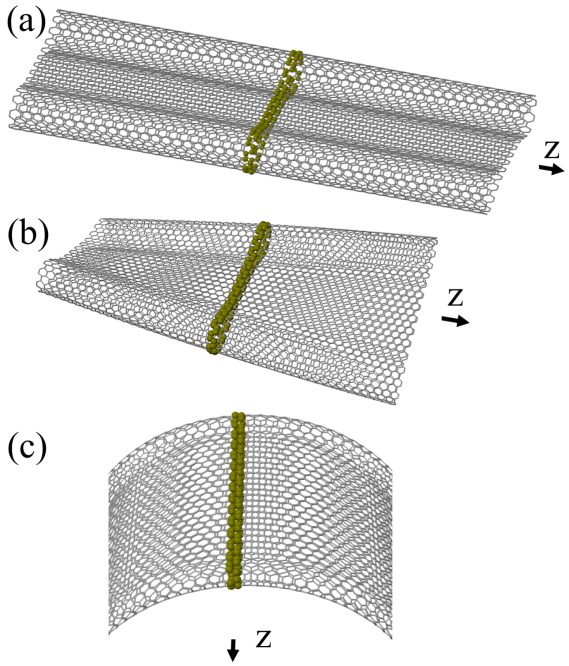

Figure 4.2. Relaxed configurations of (30,30) collapsed CNTs under (a) stretching, (b) torsion, and (c) bending. Helical boundary conditions are imposed along z axis. The simulation cells are shown as ball structures; the images obtained with eq. (1) are shown as wire frames.

translational symmetry via standard periodic boundary conditions (PBC). Pure bending is a condition of stress where only a bending moment is applied to a CNT, without simultaneous application of axial forces. Since, a bent CNT is incompatible with PBC, this type of deformation is usually imposed in a cluster fixed-end approach, which involves a large number of atoms and where special care must be taken to relieve the axial strain in the CNT. Because under objective

boundaries the only constraint imposed on the simulation cell is the bending angle, the N_o atoms are free to move away or toward the rotation axis. The curvature of the CNT, is not imposed but is a result of the relaxation. Therefore, our method inherently tends to relieve the axial strain in the unit cells.

Our calculations considered collapsed (30,30) and (35,35)-(30,30) CNTs. The N_o atoms of coordinates $\mathbf{X}_{i,0}$ located in the simulation cell are imposed the objective boundary conditions

$$\mathbf{X}_{i,\zeta} = \zeta\mathbf{T} + \mathbf{R}^{\zeta}\mathbf{X}_{i,0}$$
$$\mathbf{T} = \begin{pmatrix} 0 \\ 0 \\ T \end{pmatrix} \qquad \mathbf{R} = \begin{pmatrix} \cos\gamma & -\sin\gamma & 0 \\ \sin\gamma & \cos\gamma & 0 \\ 0 & 0 & 1 \end{pmatrix} \tag{4.1}$$

Here, $\mathbf{X}_{i,\zeta}$ are the coordinates of the ζ-th helical image of this atom, $\mathbf{T}$ and γ are the translation vector and angle comprising the helical operation. We describe next how these conditions allow to describe uniformly stretched, twisted, and bent collapsed CNTs: (i) With the boundary conditions expressed by Equation 4.1, the standard translational case is regained by setting $\gamma = 0^0$. An axial strain then can be applied by setting $\mathbf{T}$ around its relaxed state value $\mathbf{T}_0$=2.47 $\mathring{A}$. (ii) Figure 4.2b shows how an infinite collapsed (30,30) CNT, where -$\infty < \zeta < \infty$, under differential torsion (with $\gamma = 10$) is described from a unit cell containing $N_o = 120$ carbon atoms. To simulate this state, the twist angle γ acts as a constraint. The

treatment of the long-ranged L-J interactions relies on a helical Ewald summation approach [29]. (iii) To simulate pure bending with Equation 4.1, $\mathbf{T}$ is set to zero and γ to $2/N_a$, where N_a is an integer, and $\zeta = 0, ..., N_{a-1}$. This simulates a closed ring of constant radius R. The L-J interactions are calculated by direct real space summations. The collapsed shape introduces anisotropy. Bending along the closed edge direction is much harder than along the collapse direction, when the central one-atom thick layers undergo out-of-plane bending. In Figure 4.2c, we demonstrate the bending of the collapsed (30,30) CNT along the soft direction, with $N_a = 90$. Simulating bending along the hard directions is done by re-orienting the unit cell such as the collapsed plane becomes perpendicular onto the z axis. Conjugate-gradient relaxations carried out under the constrains (i)-(iii) were considered converged when the maximum atomic force was less than 10^{-4} Hartrees/Bohr. For the twist simulations, the electronic states were sampled over 20 uniformly distributed k helical points. For bending, all N_a angular points were considered to calculate the electronic energy. Our atomistic simulation results summarized in Figure 4.3 and 4.4 are discussed next.

4.3 Results

4.3.1 Objective DFTB Simulations of Collapsed CNTs

Previous atomistic calculations obtained that the failure elongation strains of defect-free cylindrical CNTs is about $14 - 22\%$, depending on chirality[6], and that various defects can trigger fracture at smaller strains [92]. We find that the extended closed-edge "defects" are not promoting fracture and that the collapsed CNTs are not developing broken bonds up to the considered 12% strain. In fact, we find that the characteristic dimensions of the collapsed shape are changing very little, even at larger stretching, Figure 4.3(b). The computed strain energy, plotted in Figure 4.3(a), gives nearly quadratic overlapping curves for the stretching of collapsed (30,30) CNTs and (35,35)-(30,30) CNTs. The second derivative of the two overlapping curves of 64 eV is consistent with the stiffness of stretched graphene [82], indicating that overall the high curvature at the closed edges affects little the in-plane elasticity of the CNT walls. The cross-sectional shape plays an important role in the torsional attributes of nanofilaments. Cylindrical CNTs are extremely stiff torsional springs [88], and for this reason this deformation is typically ignored in mesoscopic models [78]. By comparison, the collapsed CNTs are significantly less stiff under torsion since the hexagonal walls are storing less shear strain energy under a similar amount of differential twist [85, 88]. Thus,

this deformation must be accounted for at the mesoscale especially in collapsed CNTs with fewer numbers of walls, Figure 4.3(c). The collapsed shape is again preserved under severe twisting, with the separation between flattened faces practically pinned at the 0.34 nm vdW equilibrium distance, and closed edges lacking any bond breakings, Figure 4.3(d). Figure 4.3(e)-(f) and Figure 4.4 present our bending simulation results. The simulated behavior may be summarized as follows: initially, at low values of curvature, the CNT is in a state of pure bending with accumulation of in-plane elongation and compression strains on the opposite faces. The separation of the two strain energy curves with the number of layers in Figure 4.3(e) indicates that accumulation of strain is larger in the outer walls, which are more distant from the neutral bending plane. As curvature increases, the increased in-plane strain is accommodated by slightly decreasing the interlayer spacing in the central region, Figure 4.3(f), as well as the bulging of the edges away from the neutral surface with a width increase. Remarkably, this shape adjustment occurs without the breaking of any bonds located in the high curvature edges. By measuring the bending curvature at the different γ, we also noted that the $(\gamma\pi/180^\circ)/T_0$ approximation of the curvature is excellent. For example, for the configuration shown in Figure 4.3(f) the predicted bending radius is 3.55 nm while the one measured directly, by averaging the atomic positions, is 3.56 nm. We can conclude that like graphene, collapsed CNTs lack stretch-bending

coupling up to fairly large curvatures.

CNTs:	C (eV)	K (eV)	D_s ($eVnm^2$)	D_h ($eVnm^2$)	Y (TPa)	G (GPa)	w (nm)	h (nm)
(30,30)	7697	13520	300	25630	1.15	37	6.32	0.68
(35,35)(30,30)	15401	82824	2404	60696	1.27	102	6.57	1.31

Table 4.1. Stiffness constants for (30,30) and (35,35)(30,30) CNTs calculated with DFTB, and the material constants and cross-sectional parameters of the derived beam models.

The orders of magnitude differences between the extracted soft and hard bending constants D_s and D_h (Table 4.1) indicate that the collapsed CNTs exhibit a very strong bending preference along the soft direction. We previously studied the bending of 2-layer graphene, and obtained a bending stiffness of 163 eV [31]. Using this information, we can approximate the bending stiffness of the (30,30) CNTs containing 120 carbon atoms per cell as that of a bilayer with 60 atoms per layer, each taking up $2.71\mathring{A}^2$ of area. We obtain $26,340eV\mathring{A}^2$, which is close to our D_s fitted value. The value approximated this way is below the computed one, indicating that the closed edges are reducing to some small extent the remarkable flexibility of collapsed (30,30) CNT.

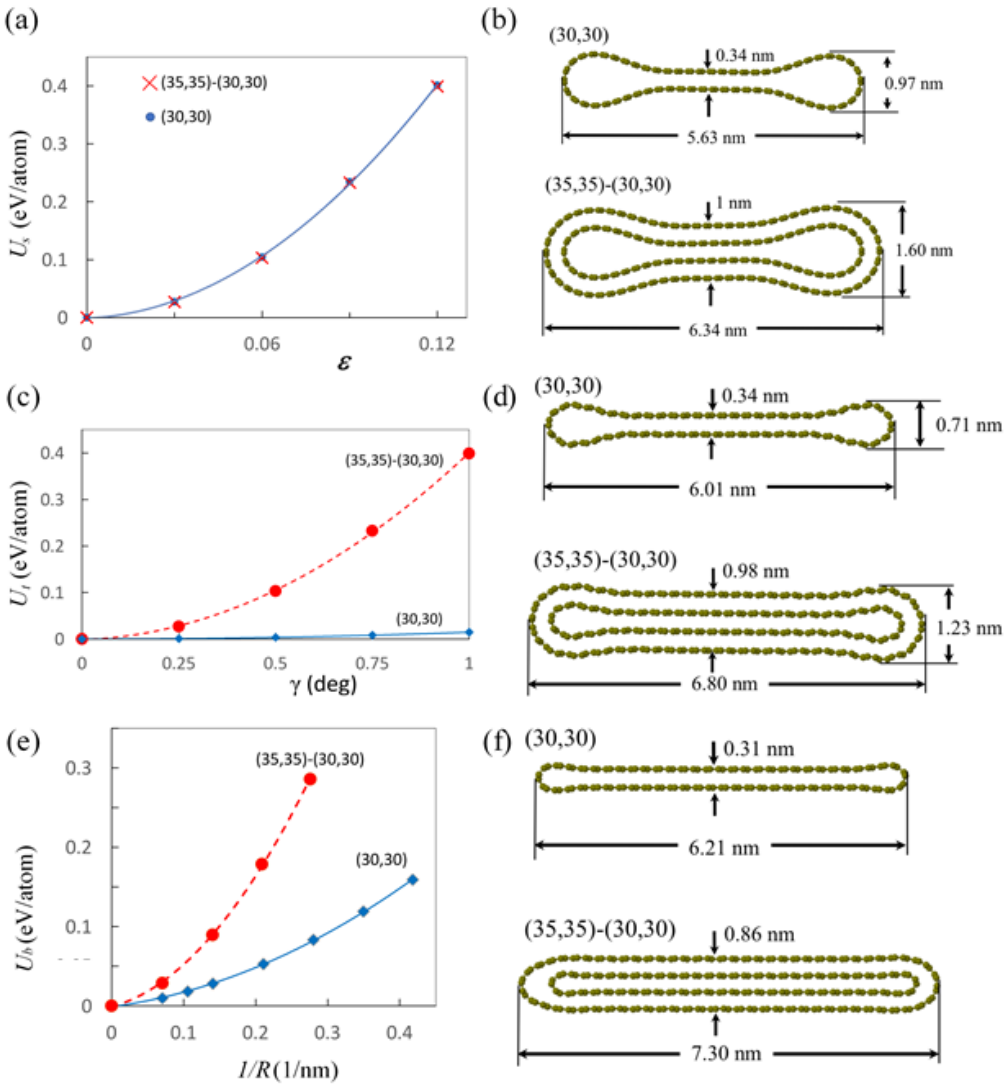

Figure 4.3. (a) Stretching energy vs.ϵ for (30,30) and (35,35)-(30,30) CNTs. Lines represent quadratic fits of the data points. (b) The relaxed shapes of the unit cells at $\epsilon = 12\%$. (c) Torsional energy vs.γ. (d) The relaxed shapes of the twisted unit cells at $\gamma = 10$. (e) Bending energy vs. $1/R$ (soft direction). (f) The relaxed shapes of the bent unit cells at γ=40 (N_a=90 and R=3.5 nm). The geometrically deformed CNTs become visible when the unit cells displayed in b, d, and f are subjected to equation (1).

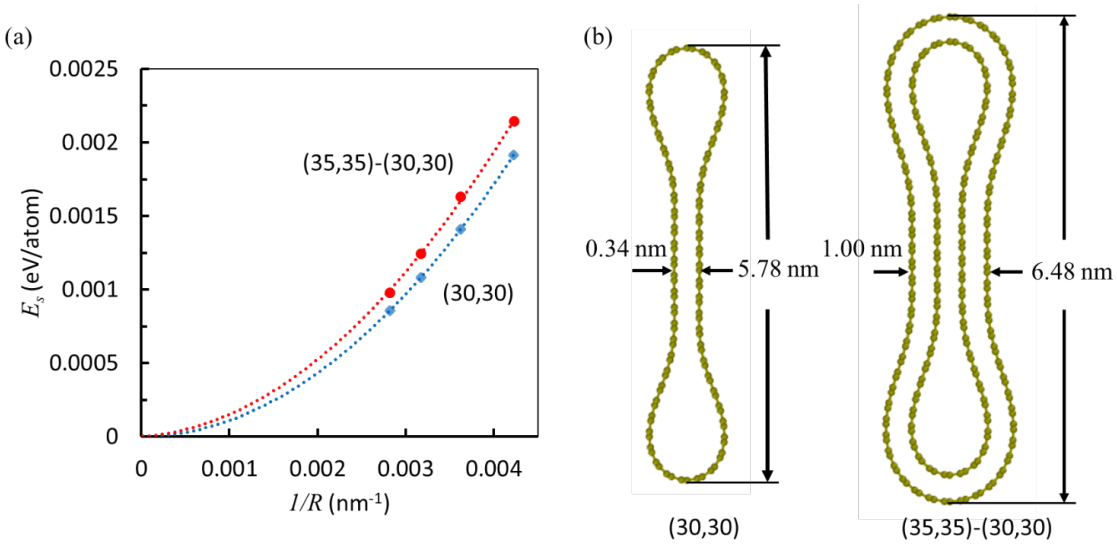

Figure 4.4. (a) Bending strain energy vs. curvature (hard direction) for (30,30) and (35,35)-(30,30) CNTs. Lines represent quadratic fits of the data points. (b) The relaxed shapes of the bent unit cells at large curvature. Here, $\gamma = 0.060$ and $N_a = 6000$. The radii of the closed rings are $R = 236nm$.

4.3.2 Derivation of mDEM Models for Collapsed CNT

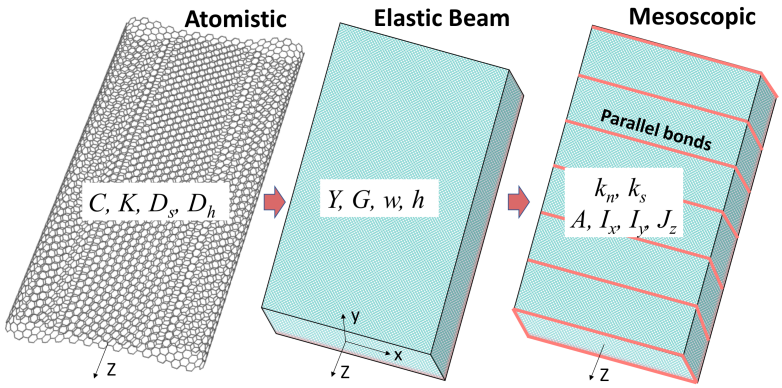

Figure 4.5. Representation of a collapsed CNT (left) as an isotropic elastic beam (center). Next, a collection of mesoscopic bricks connected by parallel bonds (right) are representing the inertial and elastic properties of the beam.

DEM, the macroscopic method introduced 40 years ago by Cundall and Strack, [22] is largely used today for simulating the mechanical properties of geological materials. In our previous work, we have adapted this method for cylindrical CNTs, where each CNT is represented by a chain of rigid cylindrical elements interacting with each other via contact models informed by atomistic scale simulations. Refs. [76] and [80] give detailed descriptions of how these microscopic interactions are incorporated into contact models, while Ref. [20] describes the application of mDEM to the mechanics of CNT yarns. Figure 4.5 illustrates our strategy for developing the mDEM model for collapsed CNTs, which involves the

intermediate step of setting an equivalent elastic continuum [80] based on the outcomes of the atomistic calculations summarized in Figure 4.3 and 4.4. The stiffness constants C, K, D_s, and D_h of Table 1 are obtained by direct fits of the DFTB data of Figure 4.3 and 4.4, restricted to the linear regime. With their help we can represent the stretching, twisting, and bending energies of the unit cells as $U_s = 1/2C\epsilon^2$, $U_t = 1/2K\gamma^2$, and $U_b = 1/2D_s(1/R)^2$and $U_b = 1/2D_h(1/R)^2$. We now focus on how to represent these deformations at the continuum level. While generally the elastic deformation of a nano-filament can be expressed in general with 10 elastic constants (to capture for instance cross-terms like bend-stretch coupling), the symmetries of the computed DFTB energy profile to clockwise and counter-clockwise twisting, and concave and convex bending of the collapsed CNT shape reduces significantly the number of independent constants. To this end, we propose to represent the DFTB computed energetics (encapsulated by C, K, D_s, and D_h) by an isotropic beam with rectangular cross-section which is uniform along the long axis. (A cylindrical cross-section was selected to represent cylindrical CNT [80].) The elastic energy of the beam is expressed as a summation of pure stretching, twisting, and bending strain energies along the soft and hard directions $U = U_s + U_t + U_b$. The beam idealization is identified by equating the atomistic strain energy U of the unit cell deformed in a pure mode to that of a deformed beam portion of length T_0. In pure stretching, we have $U_s = 1/2C\epsilon^2 = 1/2YAT_0\epsilon^2$,

where Y is the Young's modulus and $A = hw$ is the area of the beam cross section. In pure twisting, $U_t = 1/2K\gamma^2 = 1/2GJ_z\gamma^2/T_0$, where G is the beam torsional constant and J_z the polar moment of inertia. Finally, in pure bending along the soft and hard directions, we have $U_b = 1/2D_s(1/R)^2 = 1/2YI_yT_0(1/R)^2$ and $U_b = 1/2D_h(1/R)^2 = 1/2YI_xT_0(1/R)^2$, respectively, where $I_y = 1/12wh^3$, $I_x = 1/12hw^3$, and $J_z = I_x + I_y$. Solving these equations together, we arrived at the Y and G elastic constants, and the w and h parameters of the beam listed in the last columns of Table 4.1. Having established the elastic beam idealization, we are now in the position to develop the mDEM model, by partitioning the beam into "bricks" of lengths L. Using the PFC3D [20] computational machinery of classical DEM, these elements will be evolved in time as rigid bodies (with 6 degrees of freedom per element). In mDEM, each "brick" element of dimensions h, w, and L, is evolved in time under the laws of classical mechanics $\mathbf{F} = m\ddot{\mathbf{X}}$ and $M = I\dot{w}$,where Here $\mathbf{X}$ labels the position of the center of mass and the angular velocity of the element. The mass m and moments of inertia I_h,I_w, I_L components along the thickness, width, and length directions, respectively, of a "brick" with $L = 4T_0$, where $4N_o$ carbon atoms correspond to one distinct element, are summarized in Table 4.2. The elasticity of these elements is lumped into carefully designed parallel bond contacts distributed over the rectangular interfaces. The parallel contacts, which generate resisting forces $\mathbf{F}$ and moments $\mathbf{M}$

, are essentially distributed linear springs with normal k_n and shear k_s stiffness (measured per unit area) representing the elastic response of a brick of length L, i.e. $k_n = Y/L$ and $k_s = G/L$ [80]. In Table 4.3, we are listing the parallel bond contact parameters for $L = 4T_0$.

4.3.3 Verification and Validation of the mDEM Models

CNTs:	L (nm)	m (amu)	I_h $(amunm^2)$	I_w $(amunm^2)$	I_L $(amunm^2)$
(30,30)	0.99	5765	19660	693	19411
(35,35)(30,30)	0.99	12491	45951	2806	46717

Table 4.2. Parameters of the mesoscopic distinct element of "brick" shape with $L = 4T_0$.

In Figure 4.6 we provide a verification of the mDEM models for describing the important twisting and bending deformation modes. The (30,30) and (35,35)-(30,30) collapsed CNTs were modeled by joining together 100 mesoscopic elements with the mass and moment of inertias given in Table 4.2, and the parametrization of the parallel bonds given in Table 4.3. In the initially straight CNT, the total contact forces and moments are set to zero. The velocities of

CNTs:	k_n (eV/nm^4)	k_s (eV/nm^4)	A (nm^2)	I_x (nm^4)	I_y (nm^4)	J_z (nm^4)
(30,30)	725	232	4.30	14.3	0.1	14.5
(35,35)(30,30)	802	646	8.61	30.8	1.2	32.0

Table 4.3. Derived parameters for the parallel bond contacts. The length of the element brick is $4T_0$.

all six degrees of freedom are fixed to zero for the first element, while an external twisting moment and an external bending moment along the soft direction, are applied separately to the last element, Figure 4.6a. The deformation of the chain of bonded elements under the considered external loads results in relative twist ($\Delta\theta_w$) and bending ($\Delta\theta_h$) angles between elements. Restoring shear M_s and bending M_b contact moments are developed according to the incremental laws $\Delta M_s = -k_s J_z \Delta\theta_w$ and $\Delta M_b = -k_n I_y \Delta\theta_h$. The models are evolved in time with a 30 fs time step until equilibrium is reached. Figure 4.6(b) presents the accumulated angular displacements at the tip. The resulted values of 1.5381 rad (0.2510 rad) for twisting angle and 0.0851 rad (0.0106 rad) for bending of the single (double-) walled CNTs, agree within 4 significant digits to the closed form solutions $100LM_s/GJ_z$ and $100LM_b/YI_y$. As demonstrated in the TEM images of Figure 4.7, twisted collapsed CNTs are often encountered in the Nanocomp CNT

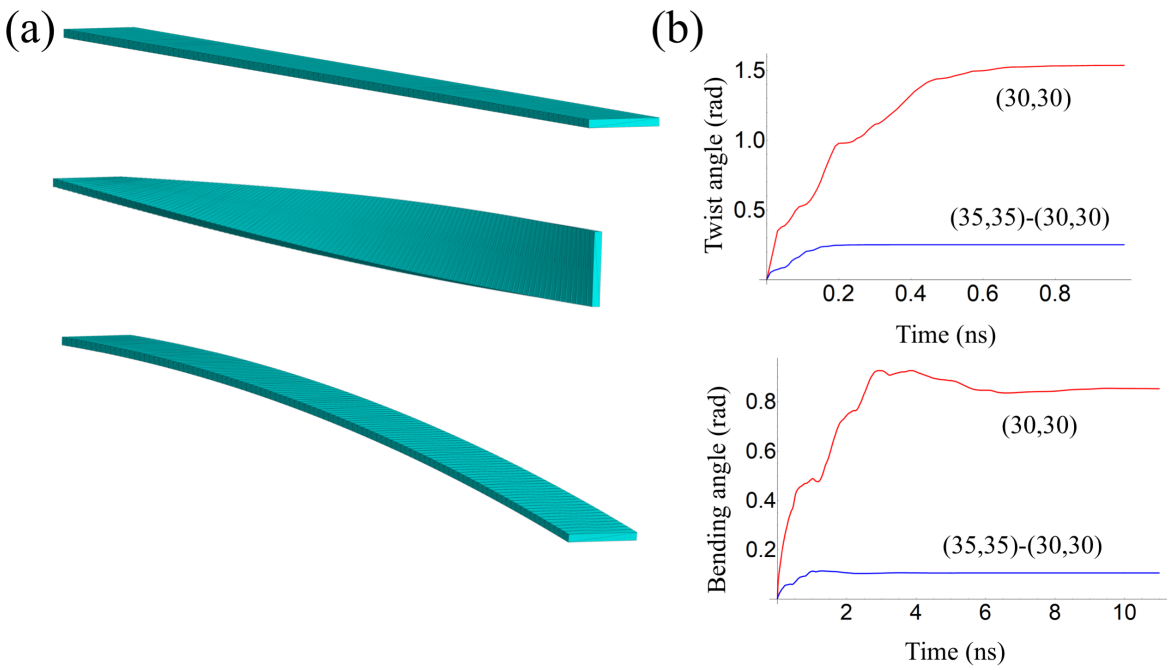

Figure 4.6. (a) mDEM simulations of a (30,30) collapsed CNT, stress free (top), and subjected to torsional (middle) and bending (bottom) moments. (b) Evolution of the total angular displacement of the element at the tip, when the collapsed (30,30) and (35,35)-(30,30) CNTs are subjected to a 50 eV twist (top) and 1 eV bending (bottom) moments.

sheets processed by stretching. The experimental images are showing twisted double-walled CNTs collapsed to a $\sim 6nm$ width. The relative twist angles across the lengths of $\sim 100nm$ and $\sim 300nm$ are π and 3π, respectively. Interestingly, the stability of the twisted CNT of Fig. 4.7(b) can be likely explained by the competition between torsional energy stored in the individual CNT and the van

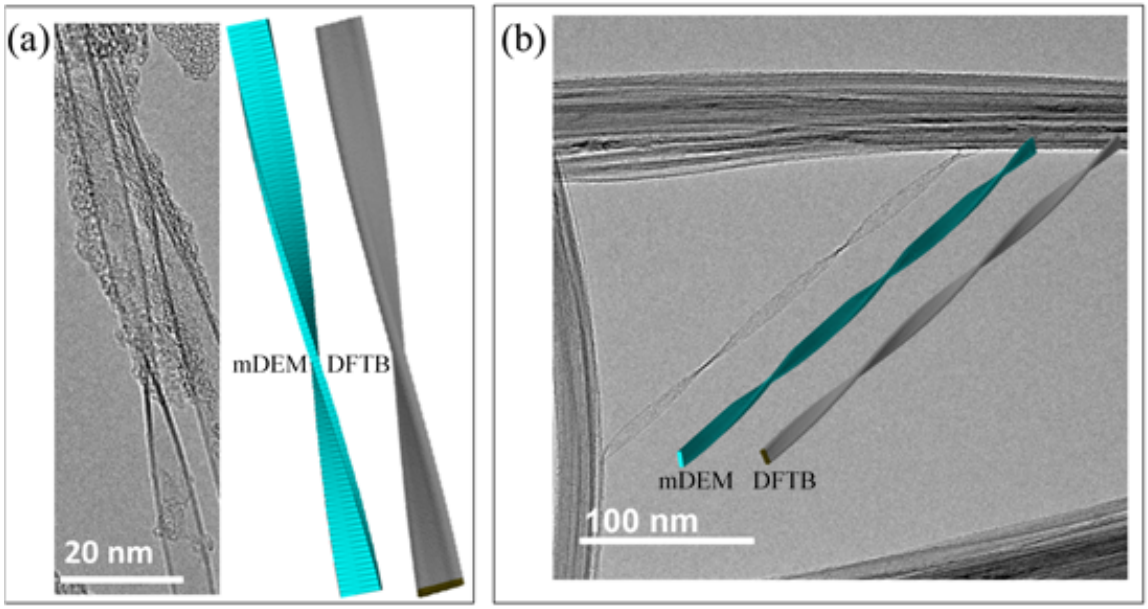

Figure 4.7. TEM images of pre-stretched CNT material, showing (a) a 100 nm twisted collapsed double-walled CNT and (b) a 300 nm twisted collapsed double-walled CNT located near the crossing of two CNT bundles. The mDEM and DFTB simulated (35,35)-(30,30) CNTs are shown near the experimental images.

der Waals adhesion energy of its ends with the crossed bundles. With mDEM, we modeled these filaments as twisted collapsed (35,35)-(30,30) CNTs comprising 100, Fig. 4.7(a), and 300, Fig. 4.7(b) mesoscopic distinct elements. To match the experimentally observed twist, the magnitude of the moment applied to the end element was determined with $\pi G J_z/100L$ and $3\pi G J_z/300L$, respectively. The cantilever set-up simulations took only a few minutes on a personal computer.

The final twist angles are indeed π and 3π, and strain energy is 1021.8 eV and 3065.4 eV. These energies are in excellent agreement with the DFTB strain energy of 2.554 eV computed of the (35,35)-(30,3) collapsed CNT unit cell under γ=0.450 differential twist

4.4 Summary and conclusions

Objective simulations provided a detailed nanomechanical characterization of collapsed (30,30) and (35,35)-(30,30) CNTs, and obtained that the collapsed shapes are robust to severe stretching, twisting, and bending deformations. On this basis, we developed ultra CG mDEM models, able to quantitatively reproduce the nanomechanical response derived from the covalent and vdW intra-tube interactions. Owing to recent advances in characterization and capturing the dynamical friction [35] and inter-tube shear between CNTs represented at the ultra CG level [16, 17], the derived mDEM models will be useful for simulating the mechanics of material systems comprising collapsed CNTs obtained by sheet stretching [2]. Recent modeling revealed that bending rigidity of CNTs impacts, among other factors, the strength of CNT yarn, with the more flexible CNTs making stronger yarns. As our DFTB calculations showed, collapsed CNTs present extraordinary flexibility, comparable to that of few-layer graphene. Therefore,

the mesoscale model can prove useful for the computational design of ultra-strong CNT yarns. The multiscale chain established here and summarized in Figure 4 has implications beyond CNTs. With the helical Ewald rule approach [93], objective simulations are now possible with the self-consistent charge (SCC)-DFTB level of chemistry [94], which allows one to tackle the nanomechanics of a large variety of nano- and bio-structures, like DNA and actin. Thus, the multiscale modeling chain proposed here can be used to derive CG models from a quantum mechanical basis for a variety of complex microscopic filaments [95].

Chapter 5

Flexibility and Nanometer-Scale Rippling of Few-layer Graphene

As mentioned in Chapter 4, bending rigidity of collapsed single-walled CNTs is close to 2-layer graphene. It's reasonable to speculate that bending rigidities of multi-walled CNTs can be approximated with few-layer graphene (FLG). In this chapter, We model bent FLG as large-radii (up to 45 nm) infinitely-long multi-walled nanotubes in order to uncover its bending rigidity. Quantum calculations based on a density functional theory-based tight-binding model extended by Lennard-Jones interactions are carried out in an objective molecular framework, which accounts for the helical and angular symmetries exhibited by these large-diameter nanotube structures. Bending of ABA-stacked FLG simulated from

different objective computational domains allow to evaluate the impact of interstitial defects and interlayer sliding onto FLG flexibility. We reveal a contrasting behavior: On one hand, inter-layer interstitials that bond to four carbon atoms located on two adjacent bent layers are stable and able to preserve the plate-like bending rigidity. Thus, introducing inter-layer interstitials can be an effective way to maintain the plate-like rigidity of FLG by preventing layer sliding. On the other hand, inter-layer sliding dramatically lowers the bending constant and makes FLG nearly as flexible as the on-atom thick graphene. We show that the layer-sliding gives rise to non-classical low-energy rippling modes characterized by wavelengths as small as a few nm and large local curvatures, which are distributed non-uniformly across the FLG thickness.

5.1 Introduction

Rippling of graphene is commonly observed. It's crucial in maintaining the structural stability of freestanding or supported graphene[96, 97], and closely related to many distinctive electronic properties[98–100]. The prevalence of rippling can be attributed to the small bending rigidity of graphene[101]. Albeit graphene has ultra-high in-plane stiffness[102], the out-of-plane deformation leads

to little energetic cost. Much endeavor has been put to explore the mechanics behind the bending properties and rippling structure of mono-layer or FLG. Continuum theory interprets graphene as thin plates[103]. However, such idealization may break down at atomistic level,especially for the mono-layer [104]. Some make resource to molecular mechanics, and reply on empirical inter-atomic potentials,such as the second-generation Brenner potential[105], to address the issue. Bending rigidity of mono-layer graphene is found to be associated with the bond angle effect as well as the bond order term related with dihedral angles [101]. Quantum mechanical approach like DFTB supplemented with objective boundary conditions, provides a more accurate and convenient tool[106]. DFTB results reveal the scaling law between bending rigidity D and number of graphene layers N.

$$D = \frac{CZ_0^2 N(N^2-1)}{12(1-\nu^2)} \qquad N \geq 2 \tag{5.1}$$

Here in-plane stiffness $C = 26.6eV/\mathring{A}^2$, interlayer spacing $Z_0 = 3.35\mathring{A}$, and Poisson ratio $\nu = 0.24$. In this work, we examined bending properties of graphene for a large range curvatures and along different chiral directions. We demonstrated inter-layer sliding made the bending stiffness of FLG similar with mono-layer.

5.2 Bending Rigidity of FLG

We discussed in detail the simulation method of bending collapsed CNTs in Chapter 4. We applied the same method to impose bending deformation. The role of translational periodicity ρ is the same as common periodic boundary condition while the angular periodicity γ, defined by $2\pi/N_a$, generates N_a periodic images each rotated by an angle γ, forming a closed ring. To model bent N-layer (NL) graphene, $4N$ carbon atoms are required, Figure 5.1a. The bent mono-layer graphene is equivalent as infinite long single-walled CNT. It's worth to point out for bent FLG, each layer contains the same number of atoms, different from multi-walled CNTs, Figure 5.1b. Also note the two unit vectors $\vec{a}$ and $\vec{b}$, Figure 5.1a, are along the armchair and zigzag directions, respectively, causing our naming conventions for CNTs to vary from tradition. (m,n) CNT in our context corresponds to conventional (m+n,n) CNT. The radius of curvature under such construction can be estimated as $N_a|\vec{a}|/2\pi$ ($N_a|\vec{b}|/2\pi$) if it's bent along $\vec{a}$ ($\vec{b}$). Thanks to such setup, layers closer to the convex (concave) side are subject to extension (compression) deformations, matching continuum theory. For 2-layer graphene, half bonds are stretched and half bonds are compressed, Figure 5.1c.

We considered bending FLG not only in armchair and zigzag directions, but also in chiral directions, Figure 5.2. For the chiral case, the way to determine

tranlational periodicity ρ and helical angle γ is discussed in ref [107]. Relaxation shows the ideal construction yields structure with minimum energy even for 6-layer graphene, Figure 5.2c-d. As in Figure 5.2a-b, in-plane deformations mainly occur along the bending direction. It has been pointed out under small curvature, graphene demonstrates isotropic bending [101], in agreement with our results in Figure 5.4a.

Rather than setting curvature as a constraint, our simulations allow radial relaxation and measure the resulting curvature. The curvature is defined as the average distance between all atoms and z axis. In Figure 5.3, We find measured curvature matches theoretical prediction very well for radius larger than $200\mathring{A}$. As the FLG is severely bent, deviation from prediction begins. The deviation starts from larger radius when there are more number of layers, since more layers means longer distance from the neutral plane. Radial expansion deals with the large strain by releasing part of the compression strain, at the cost of extra stretching of bonds located on outer layers. Within the small curvature regime, the bending energy depends linearly on $1/R^2$, and the calculated bending constant matches well with equation 5.1, Figure 5.4.

Radial deformations cannot release extension and compression strain simultaneously. Inter-layer sliding, on the other hand, allows each layer to expand

or contract. We show the inter-layer sliding is prohibited by inserting an interstitial atom between the 2L graphene, Figure 5.5a. The atom forms bonds with adjacent atoms from both layers, preventing relative sliding between layers. Simulations show the added interstitial atom is stable and the bending energy varies little from results without interstitial defects, Figure 5.5b.

We artificially realize inter-layer sliding by allocating different number of atoms for each layer. One can imagine the purpose of such setup is to create space for inner layers to expand, and fill in more atoms when outer layers contract and leave breaking bonds. With proper selection of number of atoms, angular boundary condition yields ideal single-walled and multi-walled CNTs. In the case of Figure 5.6, $N_a = 5$, rotation angle $\gamma = 2\pi/N_a$, outer layer unit cell contains 32 atoms, equivalent as 8 unit cells in Figure 5.1, and inner layer is made of 28 atoms. The exact same bond length for the 1L and 2L cases shows the breakdown of coupling between in-plane deformation and bending. The measured strain energy also validates the disappearance of in-plane strain, Figure 5.7a. Bending constant $d = E_s/R^2$. d linearly depends on N rather than $N^2(N-1)$. Note the scaling holds for $N = 1$, demonstrating the flexibility of FLG is comparable with the mono-layer.

5.3 Nanometer Scale Rippling of FLG

The vanishing in-plane strain can be attributed to our setup, however in reality, it is not common to bend FLG with as-designed layer lengths. Here we verify our theory by designing nanometer scale rippling of FLG free of in-plane strain. One unit cell of the ripple is constructed by connecting the relaxed NL graphene with its inversed image, Figure 5.8a. We relaxed the obtained structure with DFTB under periodic boundary condition, and found little deformation. Bond length measurement confirms all bonds stay around their reference states. Strain energy is very small, similar with those in Figure 5.7. Local curvature represented with pyramidalization angle shows a increasing trend from the convex side to the concave side. Wavelengths of those constructed ripples are around a few nanometers. For 10L, it's only 4.4 nm, Figure 5.8. Continuum theory would predict extension (compression) strain on the convex (concave) side. We propose that inter-layer sliding could release those strain and lead to the low energy rippling mode.

For verification of the proposed low-energy FLG rippling modes, the atomistic models obtained with DFTB were further relaxed with density functional theory (DFT) calculations until the Hellmann-Feynman forces were smaller

than 0.01 eV/Å. These first-principle calculations were performed with the Vienna Ab Initio Simulation Package (VASP) code. [1,2] The projected-augmented wave method [3,4] was used to solve Kohn-Sham equations, and Perdew-Burke-Ernzerhof (PBE) [5] functional were used to describe the exchange and correlation interactions of valence electrons. The vdW interactions were treated with the semi-empirical Tkatchenko and Scheffler (TS) [6]. The vacuum region was fixed to at least 30 Å in order to isolate the vdW interactions between the ripples. The Brillouin-zone integrations were sampled on Γ-centered 1x2x16 k-point grids for all calculations. The kinetic energy cutoff for plane waves was set to 800 eV and the convergence criterion for electronic self-consistency was set to 10-6 eV. DFT results are in good agreement with DFTB, Figure 5.9.

5.4 Conclusions

DFTB simulations with objective boundary conditions provided measurement of bending rigidities of mono-layer and FLG. Coupling between bending and in-plane strain holds for FLG as described by the continuum plate model. Nevertheless, such coupling may break down thanks to inter-layer sliding. As a result, FLG can be bent as easily as the mono-layer. Enlightened by the mechanism, we designed a new low-energy rippling mode which was proven to be stable.

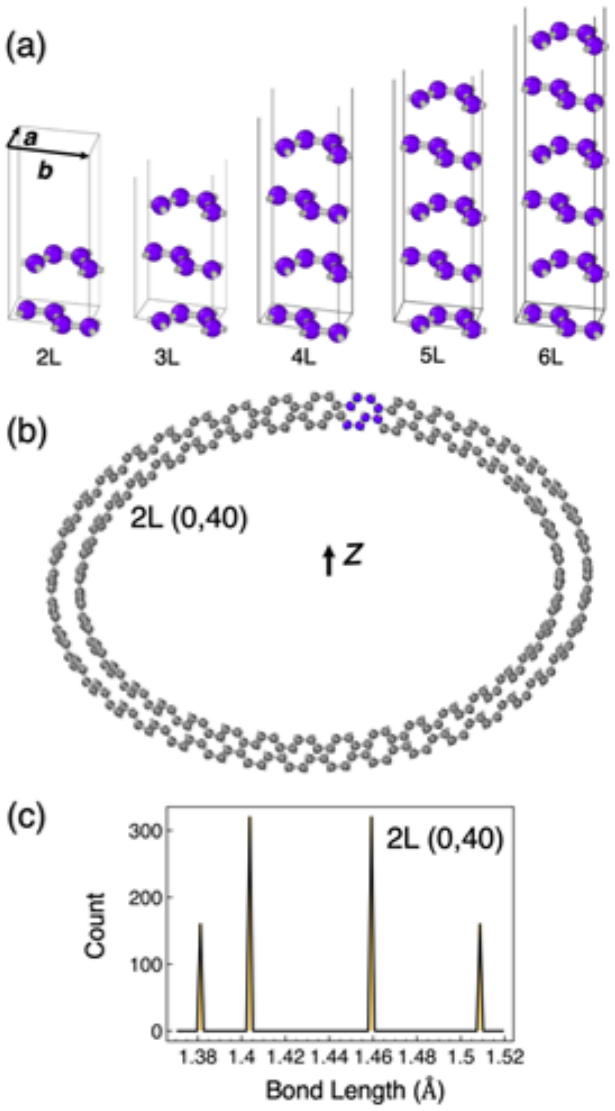

Figure 5.1. (a) Ball-and-stick representations of the relaxed N-layer orthorhombic graphene cells (N=2,...,6) under periodic boundary conditions. (b) The 2L relaxed cell (purple balls) under the translational-angular objective boundary conditions with structural parameters provided by the ideal roll-up construction for (0,40) single-walled nanotubes. The gray atoms are the angular images of the computational cell. (c) Histogram of the measured intra-layer bond lengths for the structure in (b)

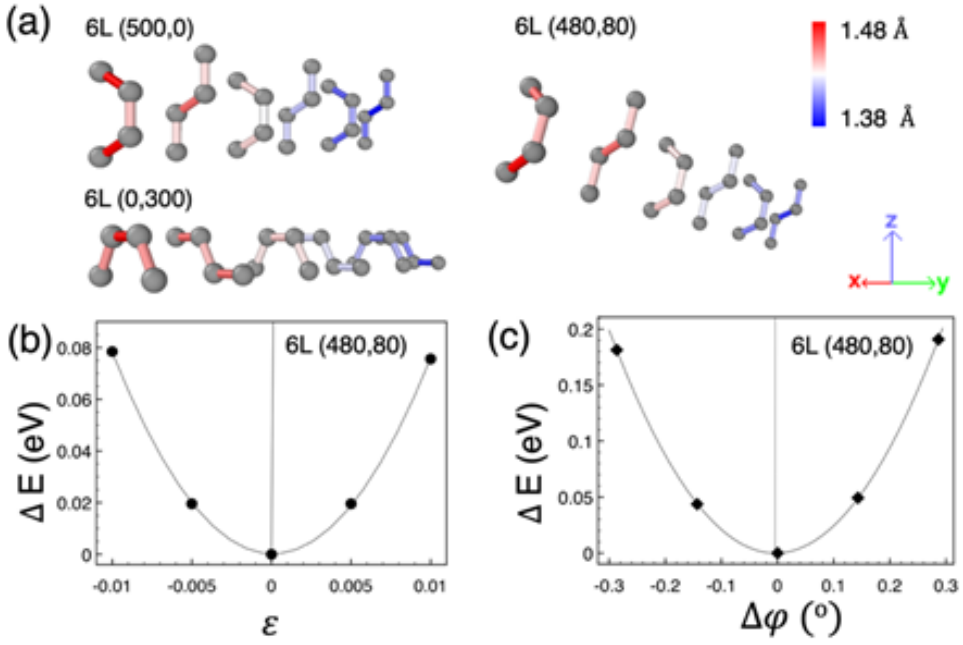

Figure 5.2. (a) Ball-and-stick representations of the 6L graphene relaxed cells under the helical-angular objective boundary conditions with structural parameters provided by the ideal roll-up construction for (500,0), (0,300), and (480,80) single-walled nanotubes. The color code indicates the intra-layer bond lengths. (b) Energy variation of the 6L (480,80) cell as the translation ρ is varied compared to the value predicted by the ideal roll-up construction ρ_0. Here $\epsilon = (\rho - \rho_0)/\rho_0$. (c) Energy variation of the 6L (480,80) cell as the helical angle ϕ is varied compared to the value predicted by the ideal roll-up construction ϕ_0. Here $\Delta\phi = \phi - \phi_0$

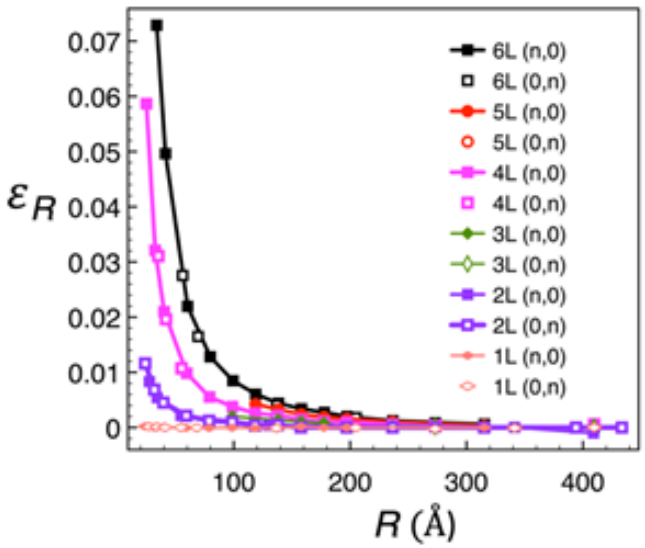

Figure 5.3. Radial expansion of the bent NL domains during relaxations with respect to the R_0 of the ideal roll-up construction, as a function of measured nanotube radius R. Here $\epsilon_R = (R - R_0)/R$.

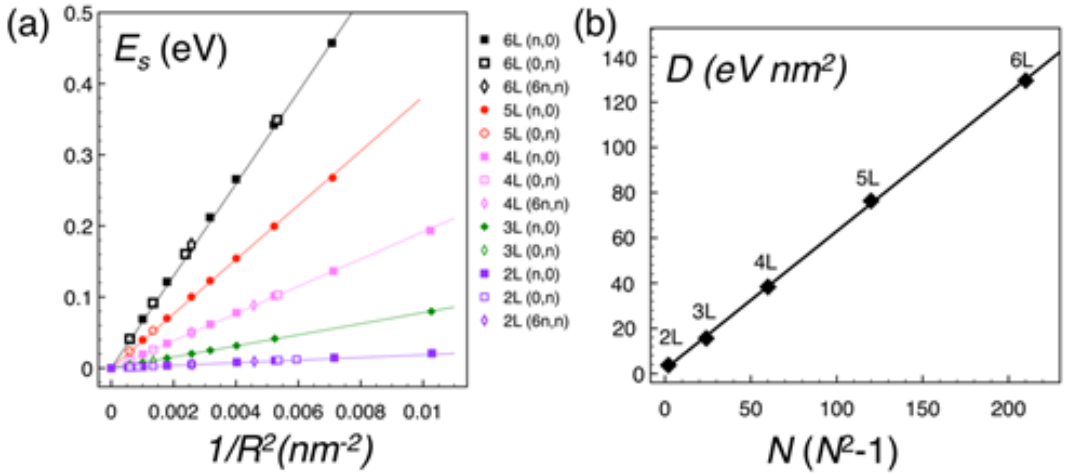

Figure 5.4. Bending of FLG without inter-layer sliding: (a) Bending strain energy (measured per atom times N) vs. curvature square, for a collection of relaxed N-layer orthorhombic graphene cells (N=2,...,6) under helical-angular boundary conditions. (b) Bending constant D vs. $N(N^2-1)$.

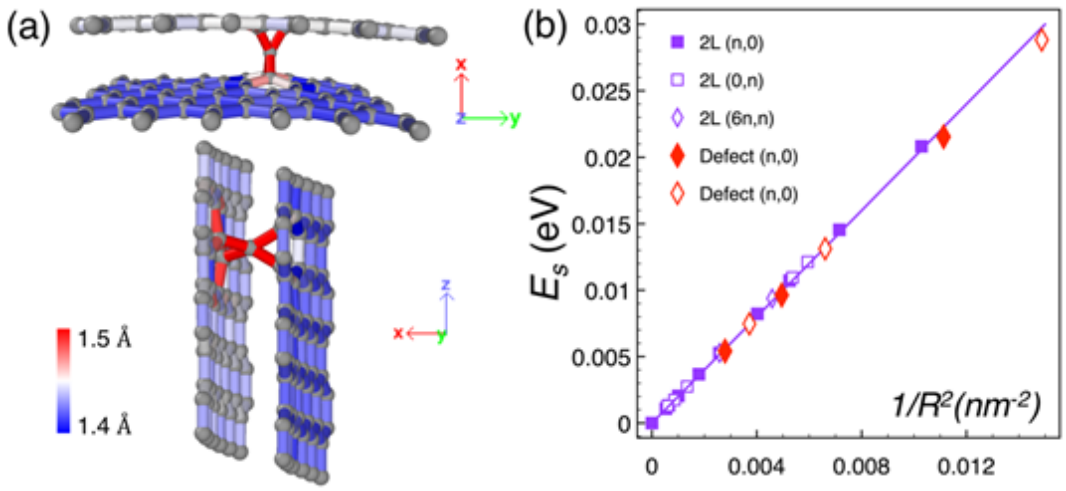

Figure 5.5. Bending of FLG without inter-layer sliding and interstitial defects: (a) Ball-and-stick representations (views along z and y axes) of a relaxed two-layer domain containing an interstitial bridge carbon above a bond center. Simulations use the translational-angular objective boundary conditions with structural parameters provided by the ideal roll-up construction for (0,40) single-walled nanotubes. (b) Comparison of the bending strain energy (measured per atom times two) vs. curvature square for 2L graphene with and without interstitial defect.

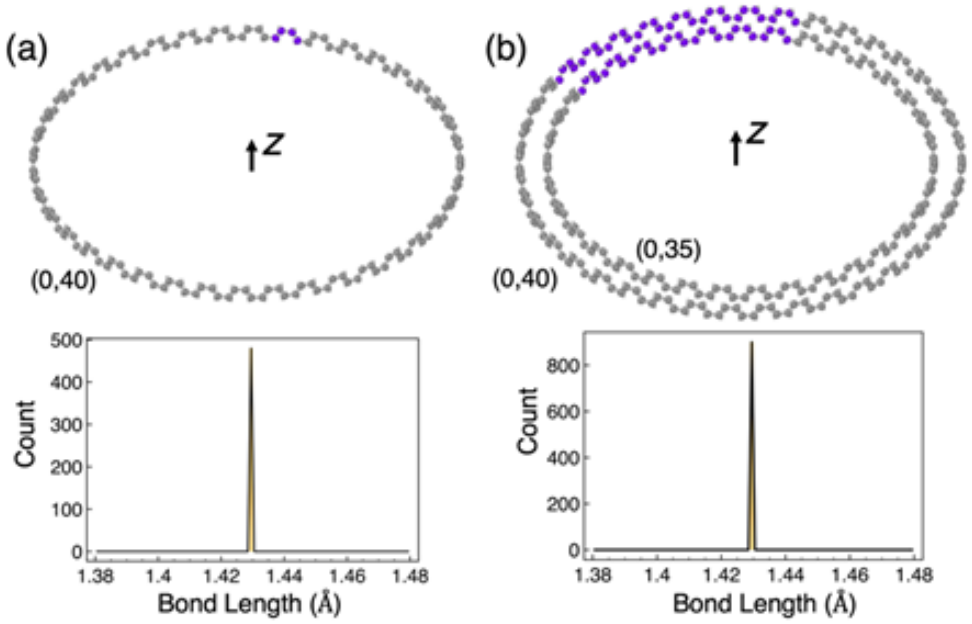

Figure 5.6. Full angular representations of (a) (0,40) single-wall and (b) (0,40)-(0,35) double-walled nanotube obtained by repeated applications of rotations (around z axis) to the objective domains shown with purple balls. Histograms of the measured bond lengths are shown under each structure.

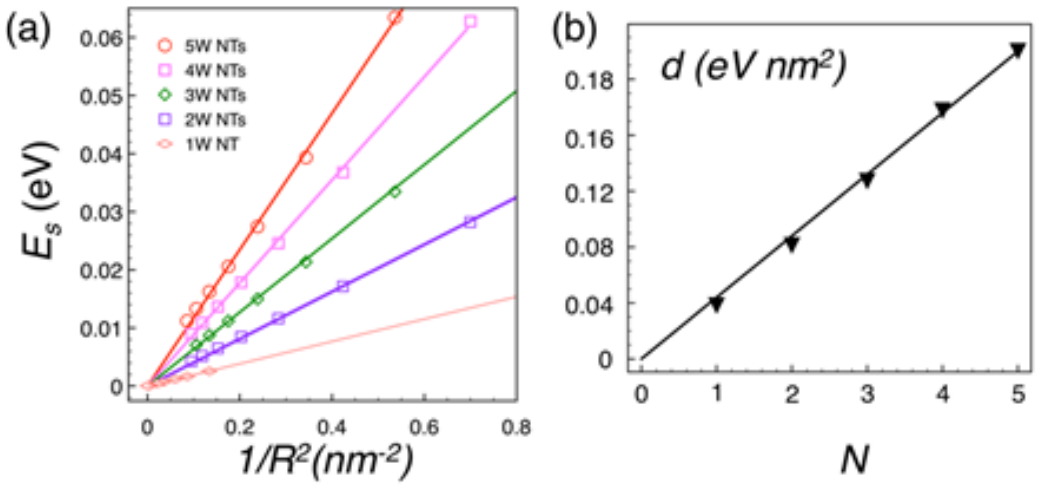

Figure 5.7. Bending of FLG without inter-layer sliding: (a) Bending strain energy (measured per atom times N) vs. curvature square, for a collection of . . . (0,n-5)(0,n)(0,n+5). . . N-walled nanotubes simulated from objective domains under translational-angular boundary conditions. (b) Bending constant d vs. N.

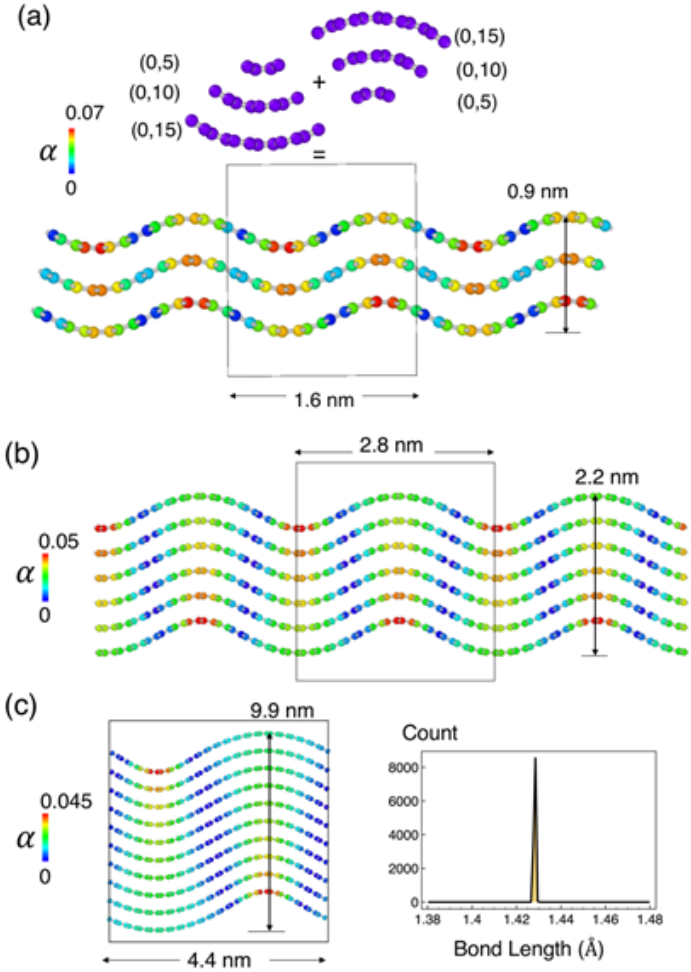

Figure 5.8. Nano-meter rippling of FLG. The unit cell is delineated by a rectangle. The color code reflects the distribution of the local curvature as measured by the modulus of the local pyramidalization angle α. (a) Ball-and-stick representation of 1.6 nm in wavelength ripple in 3L graphene. The schematics above the unit cell shows the construction of the periodic unit cell by joining together two objective domains of a (0,5) (0,10) (0, 15) nanotube. (b) A 2.8 nm in wavelength ripple in 6L graphene. (c) A 4.4 nm in wavelength ripple in 10L graphene. Histogram shows the distribution of the measured intra-layer bond lengths in this structure.

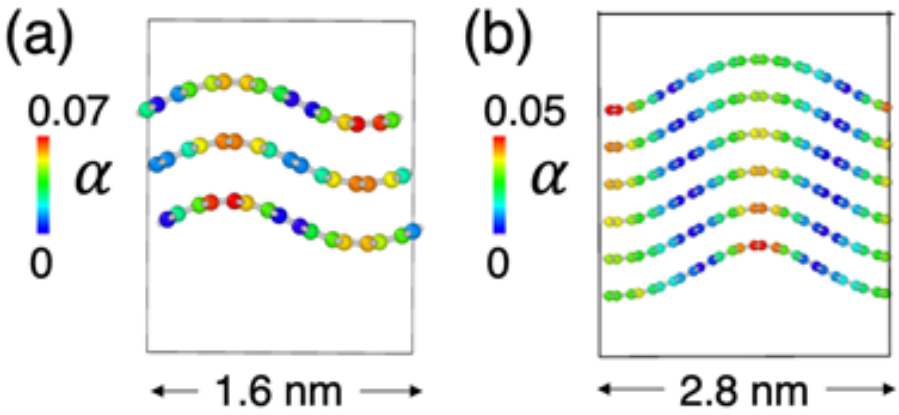

Figure 5.9. DFT verifications for the nano-meter rippling of FLG. The unit cell is delineated by a rectangle. The color code reflects the distribution of the local curvature as measured by the modulus of the local pyramidalization angle α. (a) Ball-and-stick representation of 1.6 nm in wavelength ripple in 3L graphene. (b) A 2.2 nm in wavelength ripple in 6L graphene.

Chapter 6

mDEM simulations of CNT yarns under uniaxial tension

Carbon nanotube (CNT) yarns are nanomaterials of interest for diverse applications including super-lightweight aerospace structures, artificial muscles, energy storage and generation devices. To bring fundamental understanding into the yarn formation process from the CNT soot-like material, we perform mesoscopic scale distinct element method (mDEM) simulations for the stretching of CNT networks. The parameters used by the mDEM model, including the inter-tube sliding nano-friction, are based on full atomistic results. By bridging across the atomistic and mesoscopic length scales, our model predicts the mechanical response over a large deformation range. At small and moderate deformations,

the network evolution is dominated by the zipping relaxation, which is directed along the applied strain direction. At larger deformations, we find a transition to an energetic elasticity regime, which promotes yarn densification by lowering the CNT waviness and elimination of squashed pore defects. Next, by varying the mesoscopic dissipation around the value obtained from the atomistic data, we reveal that nanofriction is a key factor for the yarn formation process. While the lack of nanofriction compromises the strain-induced alignment process, phononic and polymeric nanofriction promote CNT alignment by enabling load transfer and directed zipping relaxations, especially in networks containing long and entangled individual CNTs. Our results anticipate that the bridging of the scales approach here can be extended to include the enhancement in dissipation caused by the presence of specific polymeric layers, and to simulate the different regimes of deformation without relying on empirical parameters. This chapter has been published in Ref [20].

6.1 Introduction

Continuous yarns, composed of aligned CNTs stacked together, can be drawn out from CNT forests (a system with low degree of entanglement) [108,109], or can be formed by stretching CNT ribbons cut from buckypaper formed by

sticky CNTs thinly coated with polymeric compounds [110]. Twist-based spinning processes were also developed to increase the density of the CNT yarns and improve their mechanical properties [109–113]. Significant insights into the strain-induced alignment of stretched networks comprising multi-walled CNTs have been obtained from in situ X-ray [114] and scanning electron microscopy [115] characterizations. These studies identified important load-induced changes at the microstructural-level, including elongation to reduce CNT waviness, de-bundling, self-assembly into large bundles, and sliding friction, and have revealed the importance of the polymeric layers in promoting the strain-induced alignment. Nevertheless, the mesoscale features that most decisively impact the transition from the rather stochastic network structure to the bundled structure comprising highly aligned CNTs are not well understood. In order to gain a better understanding of this process, we simulate the stretching of a collection of various networks consisting of several hundred CNTs with the coarse grained (CG) mesoscopic distinct element method (mDEM) [13, 16].

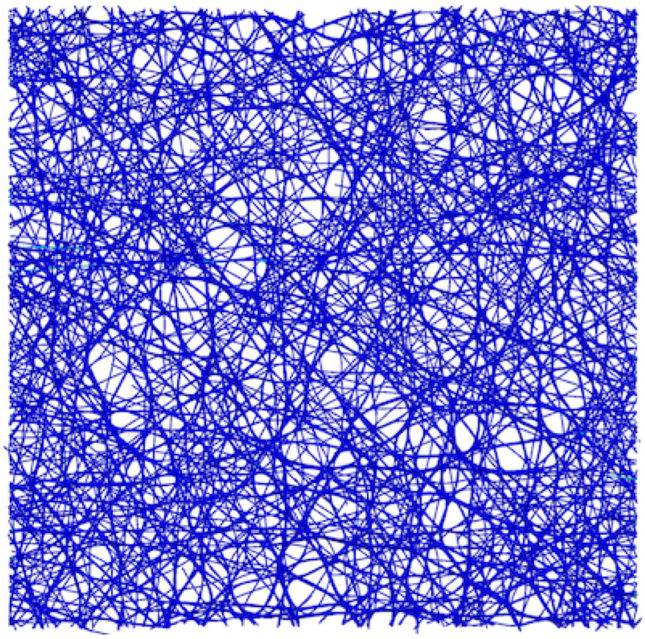

Figure 6.1. mDEM-simulated CNT network, measuring 1000 nm x 1000 nm x 11 nm in size, after 6 ns relaxation.

6.2 Mechanical behavior under uniaxial tension leading to yarn formation

Figure 6.1 displays the characteristics of a mDEM network which was directly relaxed under the influence of the mesoscopic contact interactions. The shown film was constructed from 500 (10,10) CNTs, each 950 nm in length. The network has a density of 0.14 g/cm3 and a porosity of 83.5 %. To arrive at this structure, we computer generated a random network of straight (strain free)

CNTs, which was evolved freely for 6 ns.Next We have further conducted simulations of the mDEM-represented networks to uniaxial tensile loadings. As in our previous simulations [116], two thin layers of distinct elements at the left and right edges of a film were designated as grips. Displacement-controlled loading was enabled by prescribing both grips to accelerate from 0 to the given horizontal velocity during 0.6 ns. This acceleration period is used to reduce the undesired dynamic response, which is significant in the case of instantaneous acceleration of the grips. The grip elements are allowed to evolve in the transversal direction. In a series of simulations, the network sample was elongated at the constant strain rate of $10^8 s^{-1}$over the $0\% - 150\%$ strain (ϵ) range.

The stretched network undergoes significant restructuring, with the formation of a central yarn comprising aligned CNTs, Figure 6.2. To understand this remarkable process, Figure 6.3 shows the calculated stress-strain curve as well as the evolution of the network energy composition, and number of aligned distinct element pairs during stretching. In Figure 6.3a, the flow stress was derived from the unbalanced force on the grip elements. Note that this quantity doesn't account for the transverse shrinking effect in the cross-sectional area. The number of aligned distinct element pairs shown in Figure 6.3c serves as an indicator for the bundling process. In computing it, two elements in close vdW contact are considered aligned when their crossing angle is less than 10 deg.

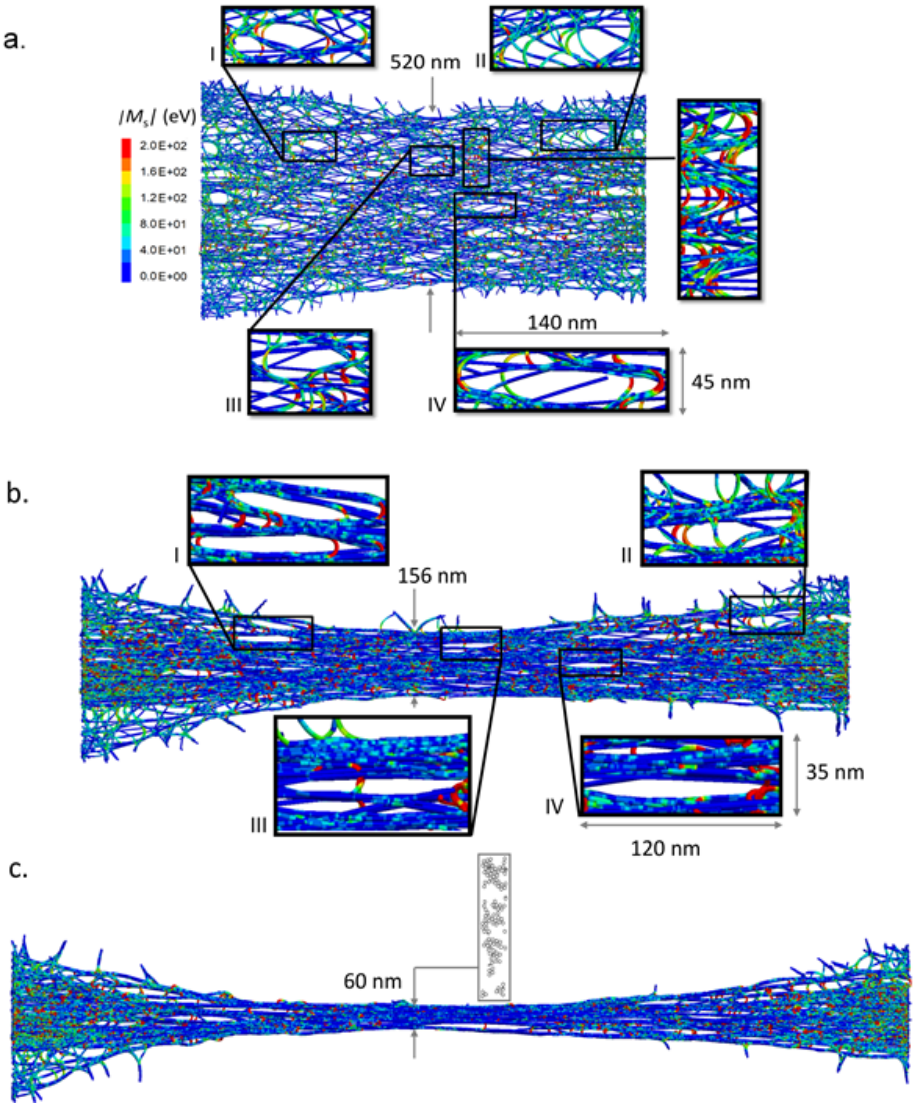

Figure 6.2. The CNT network of Figure 5.1 under (a) $\epsilon = 30\%$, (b) $\epsilon = 75\%$, and (c) $\epsilon = 150\%$. Color gives the magnitude of the bending moments stored by the parallel bonds. The callouts detail the structure around selected pores (a and b) and yarn packing (c).

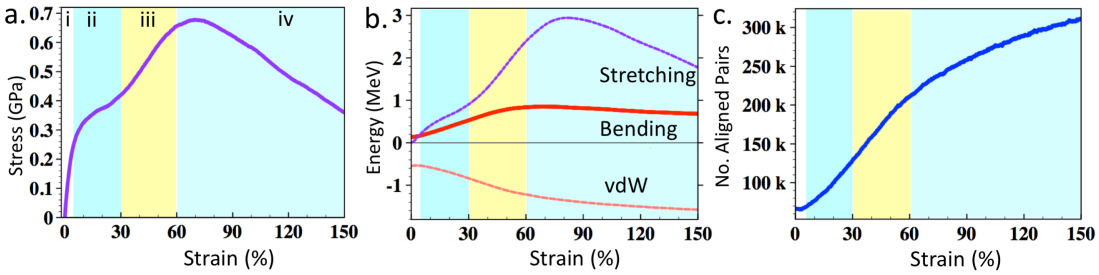

Figure 6.3. (a) Engineering stress, (b) energy, and (c) number of aligned distinct element pairs, vs. ϵ. The shadings mark the four regimes (i-iv) occurring during stretching the network of Figure 5.1.

The evolution of the sample shape and regimes revealed by our simulations are in good qualitative agreement with the experimental tensile tests of neat buckypaper [115]. Specifically, our stress-strain and strain energy curves exhibit distinct variations, which indicate four contiguous mechanical regimes: (i) elastic, for $\epsilon < 3\%$, (ii) softening, for $3\% < \epsilon < 30\%$, (iii) stiffening, for $30\% < \epsilon < 60\%$, and (iv) softening and failure, for $\epsilon > 60\%$. We discuss next the underlying distinct microstructural changes occurring in these regimes. As a common feature of these regimes, we note that the vdW energy gain and degree of bundling are increasing. Additionally, the parallel contact bonds are permanently stretched, Figure 6.3b, suggesting a good load transfer. The linear elastic stretching (regime i), visible in Figure 6.3a and analyzed in detail in our previous work [116], presents a Young's modulus of 8.6 GPa. The lowering of the vdW energy of Figure 5.3b

and the increase in number of aligned pairs of Figure 6.3c, indicate that the initial affine elastic deformation is limited by the activation of the zipping relaxation, which starts just above $\epsilon \sim 3\%$. As stretching progresses (regime ii), the network softens significantly. The behavior can be seen in the slope changes presented by the stress-strain and stretching energy curves of Figure 6.3a and 6.3b, respectively. At the microstructure level, the local bundling and the pore sizes are increasing. Pores undergo squashing, especially in the central region of the network, under the transverse contraction caused by the Poisson's effect and the zipping relaxation directed by the strain direction. In Figure 6.2a, the right callout indicates that the largest bending energy is stored into the parallel bonds located at the non-flattened side of the pores. Thus, we conjuncture that a large part of the bending energy increase of Figure 6.3b can be attributed to pore squashing. We note that the "neck" developed in the central region of the film is in agreement with experimentation [115].

The occurrence of network hardening [115] (regime iii) is intriguing, considering the mDEM linear elastic representation of the CNT constituents The underlying mechanism is the energetic elasticity of wavy CNTs, an effect visible in the evolution of the stretching energy in Figure 6.3b. Energetic elasticity is enabled by the increase in entanglement caused by pore squashing. We also note that regime iii is important for yarn formation as the number of aligned pairs

increases significantly, Figure 6.3c. This increase is the result of straightening up selected portions of wavy CNTs, an effect that promotes vdW bundling and small pore elimination.

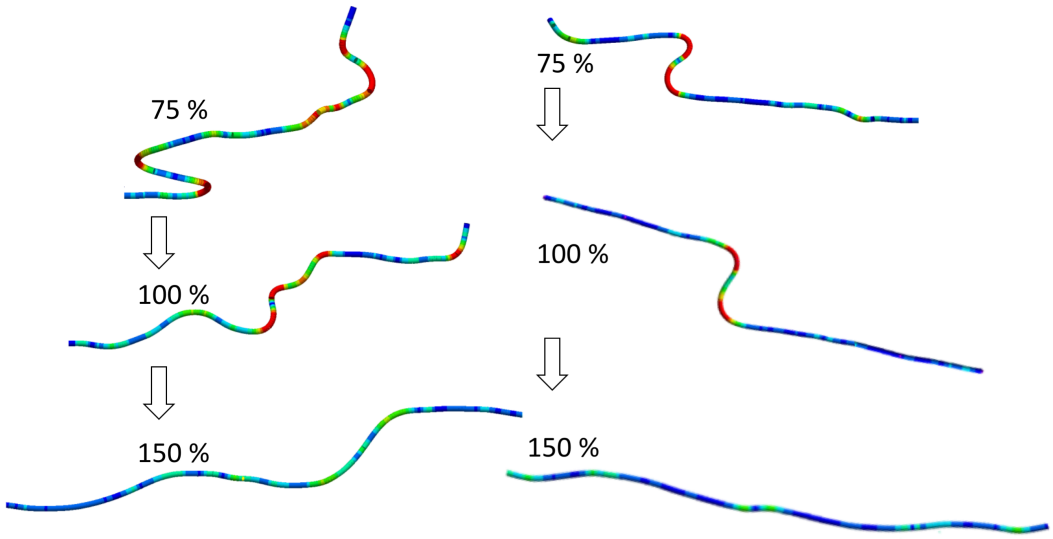

Figure 6.4. Two CNTs during horizontal network stretching, showing the removal of waviness. ϵ values are indicated above each CNT. Color code shows the bending moment magnitude, with the scale of Figure 5.2. The high curvature portions are coupled with the squashed pores of the network.

Above $\epsilon = 60\%$ (regime iv), the locking of the CNTs provided by the entanglement can no longer sustain the load transfer. The network begins its final softening and failure. At this deformation stage, the stretched CNTs begin to straighten their severely bent portions located around larger pores, Figure 6.4. The signature of disentanglement is visible in the bending energy drop, Figure 6.3b.

The $\epsilon = 75\%$ network depicted in Figure 6.2b, where the ultimate stress of 0.68 GPa is reached, conveys the remarkable microstructural changes that occurred up to this point. To arrive here, the earlier "neck" develops into a central yarn 150 nm in width, comprising highly aligned bundles with 10 to 20 CNTs each, separated by pores of nm widths. The CNT bundling and the yarn density have increased significantly in the middle part of the network. This is because many of the smaller pores closed when bent portions of CNTs were eliminated in regime iii. The remaining pore defects come from the larger pores of the original network, like the pores III and IV, which underwent significant squeezing to nm widths. We note that only the large pores located in the vicinity of the grip elements, such as I and II, are preserving their shape. Overall, Figure 6.3c shows that the $\epsilon = 75\%$ network stores significant bending, about 50% more than the initial network.

Above $\epsilon = 75\%$, the dominance of elastic deformation is substituted by

inter-tube CNT sliding. It further leads to the thinning of the bundle, Figure 6.2c, and increase in packing density. The disentanglement process continues, and more pores, like III and IV, are eliminated. To give a sense for this process, Figure 6.4 shows the evolution of two CNTs extracted from the network structure (away from the edges) showing high curvature elimination. In the network, this effect lead to disentanglement and pore closing. During further film stretching, the central cross section of the $\epsilon = 150\%$ network (Figure 6.2c) shows organization into three main aligned bundles, each containing about 30 CNTs, separated by nm-size pores. As deformation continues, the network will eventually fail by smooth sliding, i.e., when aligned CNTs lose their inter-tube binding [16, 116]. The tensile strength of such yarn could be enhanced for example by CNT crosslinking [117].

6.3 Parametric study of the yarn formation

Having identified the evolution of the stochastic network subjected to large uniaxial deformations, we now explore the parameter design space, which consists of the magnitude of the mesoscale friction, CNT length, entanglement, and high degree of CNT bundling. After first confirming the robustness of the yarn formation process by stretching of a ribbon network, we are required to consider a smaller size network to gain a reasonable computational efficiency.

6.3.1 Pre-equilibrated ribbon network of 814 nm CNTs under uniaxial tensile load

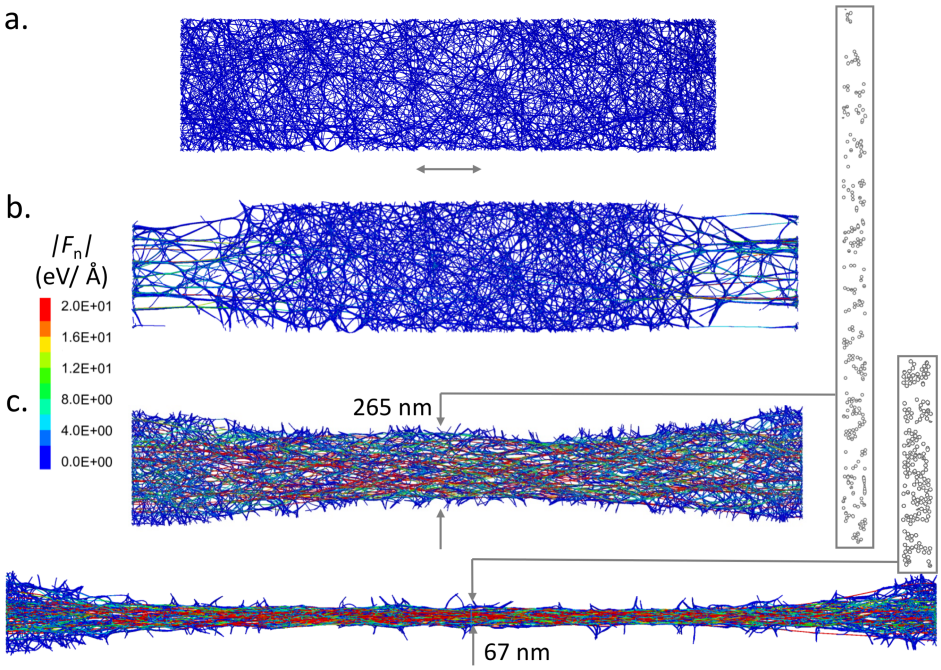

Figure 6.5. (a) mDEM relaxed CNT ribbon, measuring 2000 nm x 500 nm x 11 nm in size. (b) The $\epsilon = 30\%$ ribbon. The double arrow indicates the ϵ direction. Friction was not accounted for (i.e., $\gamma = 0$). (c) $\epsilon = 30\%$ (top) and $\epsilon = 90\%$ (bottom) ribbon. Here, $\gamma = 0.36pNs/m$. Color reflects the magnitude of the normal force stored by the parallel bonds. The callouts detail the yarn packing.

We have next probed the stretching response of a ribbon network with 2000 nm x 500 nm x 11 nm dimensions. The ribbon contains 800 (10,10) CNTs, and was cut out of a buckypaper containing CNTs 814 nm in length. The density

is 0.19 g/cm3. The ribbon structure after 6 ps relaxation is shown in Figure 6.5a. Two sets of mechanical simulations consider on one hand a purely athermal model (i.e., $\gamma = 0$) and, on the other hand, a model with enhanced, $\gamma = 0.36 pNs/m$, friction. For the latter case, the three times larger than the phononic friction was selected to explore the trend when dissipation is enhanced by the presence of polymeric layers between CNTs [110, 115].

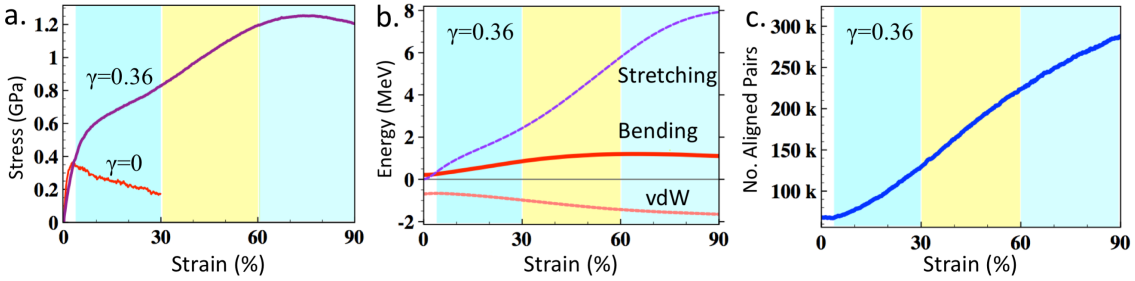

Figure 6.6. (a) Engineering stress, (b) energy, and (c) number of aligned distinct element pairs, vs. ϵ. The shadings mark the four contiguous regimes (i-iv) occurring during the stretching of the pre-equilibrated CNT ribbon of Figure 5.5a. The units for γ are pN s/m.

The differences in the ribbon network morphologies shown in Figure 6.5a and b, and the stress-strain curves of Figure 6.6a highlight the key role of mesoscopic friction. Both networks can sustain the short-lasting elastic deformation, where the Young's modulus measures 6.6 GPa. However, the friction-free network fails shortly afterwards by pulling out of the network the gripped CNTs.

The magnitude of the stretching force at each contact bond displayed in Figure 6.5b indicates poor load transfer at $\epsilon = 30\%$. The load "penetration" distance of about 500 nm on each side leaves intact the central section, which lacks the characteristic necking observed in experiment [115]. It follows that accounting for mesoscale friction (of phononic or polymer origin) is critical for establishing the load transfer through ribbon, which in turn triggers the deformation regime ii.

As it can be inferred from Figures 6.5c and 6.6, the deformation of the ribbon with enhanced friction follows the deformation regimes identified in Section 6.3. The formation of the yarn is significantly accelerated by the faster zipping relaxation of the nearly-transversal oriented CNTs, which by construction are expected to be shorter than the 814 nm in length nearly-axial CNTs. At the end of the first softening regime, the $\epsilon = 30\%$ ribbon presents an extended neck. As it can be seen in the shown cross-section, the yarn contains many bundles, each containing only a few CNTs.

The strain hardening regime follows. Reflecting the increase in nanofriction, the stiffening presents a modulus of 1.2 GPa, which is slightly larger than the 0.9 GPa measured in Figure 5.3a. As it can be seen in the side and cross sectional views at $\epsilon = 90\%$, the packing and density of the yarn are significantly enhanced with respect to the isotropic network, Figure 5.2c.

6.3.2 Preconditioned network of 475 nm CNTs under uniaxial tensile load

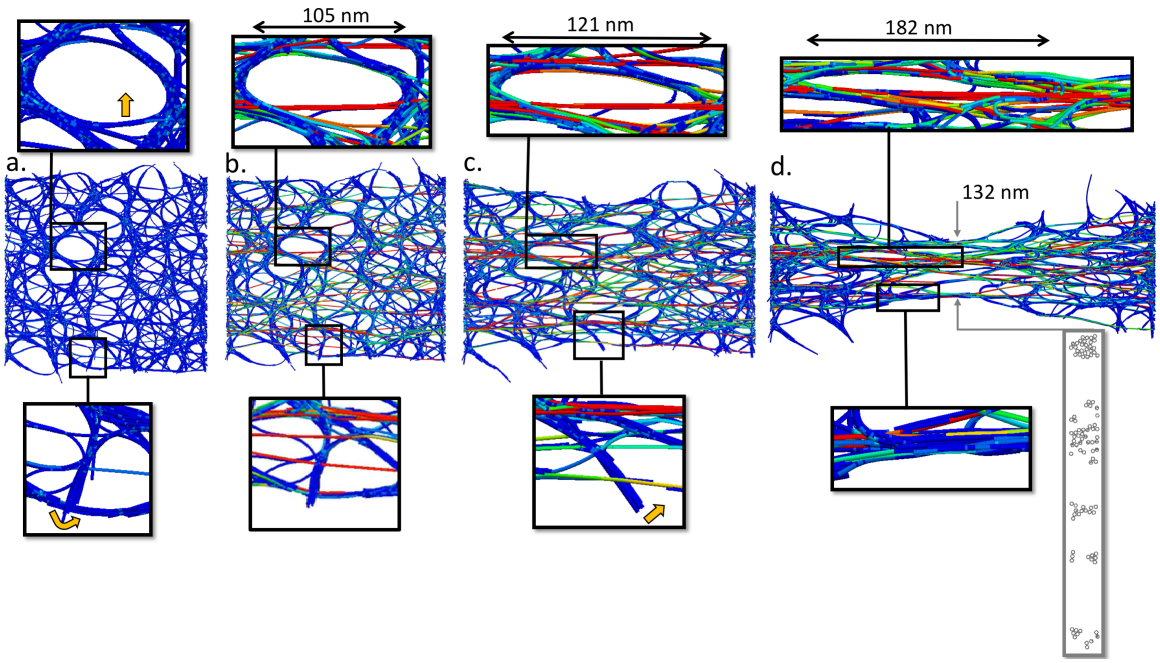

Figure 6.7. The preconditioned 500 nm x 500 nm x 11 nm CNT network at (a) $\epsilon = 0\%$, (b) $\epsilon = 10\%$, (c) $\epsilon = 30\%$, and (d) $\epsilon = 75\%$. Color gives the magnitude of the normal force stored by the parallel bonds. The upper callouts detail unzipping (yellow arrow) followed by zipping. The lower callouts exemplify zipping of bundles (yellow arrows). The yarn packing at $\epsilon = 75\%$ is also shown.

On a longer time, a (10,10) CNT network is slowly evolving toward a cellular network with large pores. An efficient way to remove the kinetic barriers encountered during this evolution, and accelerate the dynamics is to apply cycling

strain loading [118]. Following this approach, we have subjected our network to six 60% compression-recovery cycles. The resulting cellular network lowered its energy by nearly 100%, Figure 6.8, due to the significance increase in vdW energy. Interestingly, the subsequently applied 6 ns relaxation protocol gave a decreasing trend for the bending energy component, which is opposite to the bending energy increase presented by the initially prepared network. This behavior suggests that the evolution of the pre-cycled film starts to be dominated by the individual CNT sliding relaxation, which eventually disintegrates the network into disconnected bundles [119]. We have recently studied the response of this network to compressive strains and small stretching deformations [120].

Representative snapshots of the network evolution during stretching are shown in Figure 6.7, while the engineering flow stress, network energy decomposition, and number of aligned pairs, vs. ϵ are shown in Figure 6.9. Bending modes are still dominating the deformation of the preconditioned network, in spite of its significantly thicker bundles. To understand this similarity, it is important to recall that, because the of the CNT smooth sliding, CNT bundles are still softer to bending [121]. Nevertheless, the deformation of the preconditioned network brings also some new distinctive features. In the initial stages of the deformation, the applied tensile load is carried by the CNTs which are most aligned to the applied strain direction. At the microstructure level, the stretching of these

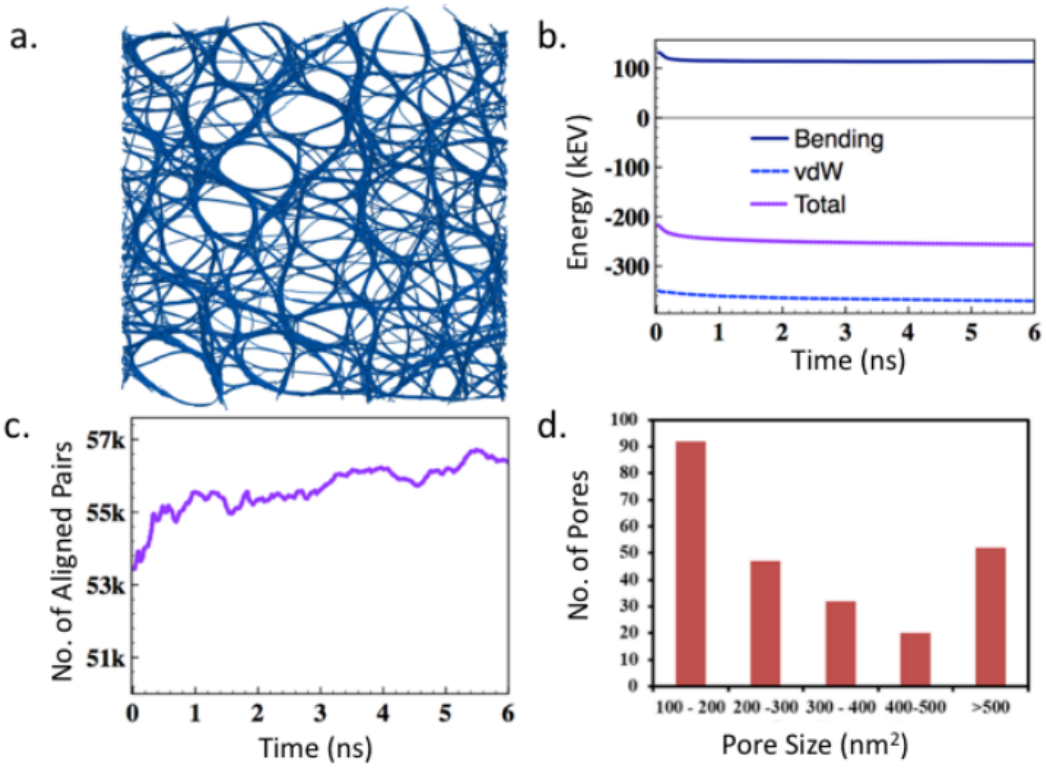

Figure 6.8. Pre-compressed CNT network, measuring 500 nm x 500 nm x 11 nm in size after 6 ns relaxation. (b) Bending, vdW, total energy, and (c) number of aligned pairs during the network relaxation process. (c) Pore size distribution after 6 ns relaxation. Here $\gamma = 0.36pNs/m$.

CNTs can lead to un-zipping (or de-bundling), Figure 6.7a-b, a new effect that is globally visible in the initial increase in the vdW energy of the network until $\epsilon = 10\%$, Figure 6.9b, and the drop in the number of aligned pairs measure, Figure 6.9c. After the network yields, at 0.32 GPa, there is a continuous drop in stretching energy. Although the vdW energy component is lowered and number of

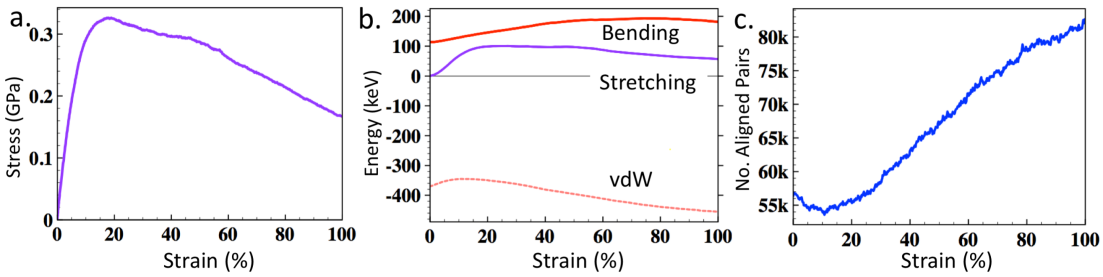

Figure 6.9. (a) Engineering stress, (b) strain and vdW energy components, and (c) number of aligned pairs, vs. ϵ. Here $\gamma = 0.36pNs/m$.

aligned pairs increases significantly, the load transfer is not sufficiently potent to insure a massive bundle-to-bundle zipping relaxation directed along the applied strain direction. (The callouts of Figure 6.7 exemplify two strain-directed bundle-to-bundle relaxations.) As a result, the yarn presents many disparate bundles separated by large pores evolved from the original structure, Figure 6.7d. Further stretching does not lead to significant yarn densification. Instead, the network fails in a fracture mode with smooth sliding failure occurring gradually in each bundle, Figure 6.10.

6.4 Comparison with bead-and-spring model

CG molecular dynamics models, such as the simple bead-and-spring models appropriated from polymer physics, are widely used for studying the mechanical properties of CNT systems, and these models have been recently used

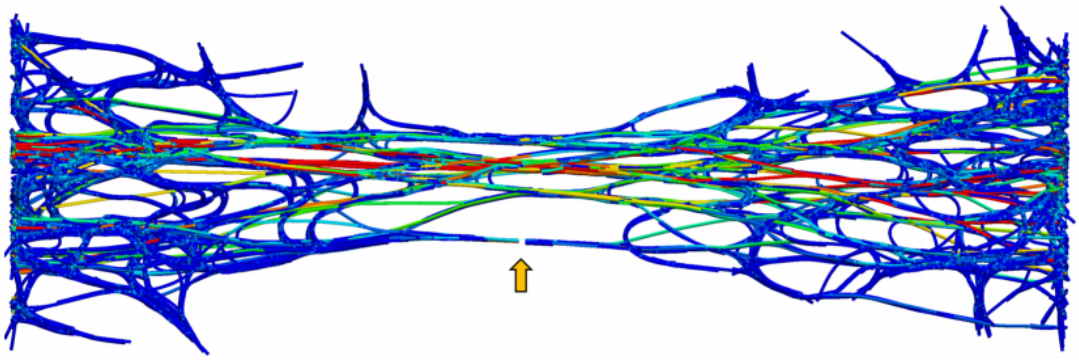

Figure 6.10. The preconditioned 500 nm x 500 nm x 11 nm CNT network at $\epsilon = 110\%$. The yellow arrow shows the failure by smooth sliding in one of the bundles.

for studying the stability and mechanical behavior of buckypaper films [118, 122]. While these CG models as well as the more advanced ones, like shape-based mesoscopic dynamics [119], recognized that CNT-CNT sliding-friction and CNT-CNT zipping are important microstructural processes involving individual CNTs, training these key dissipative processes to the underlying atomistic representation has not been yet attempted. In fact, the simple bead-and spring representation of CNTs virtually removes the dynamical sliding friction of CNTs Fig 6.11.

The detailed description of the bead-and-spring model we select is documented in ref [21]. In order to significantly reduce the corrugation artifact, each bead represents 55 carbon atoms. The equilibrium distance between beads is

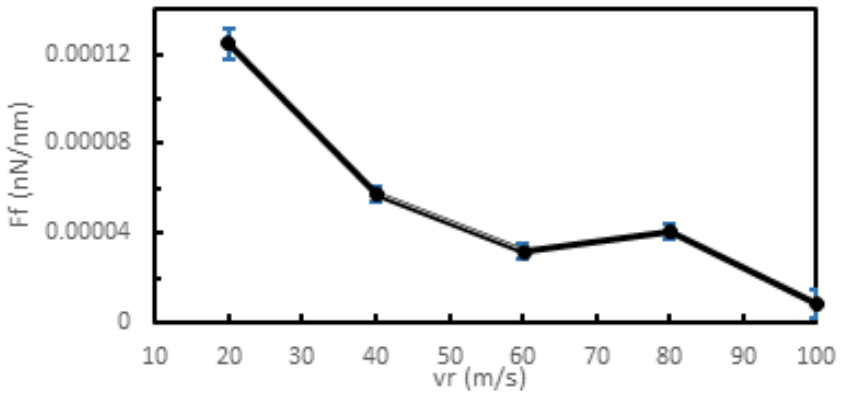

Figure 6.11. Friction force F_f (per unit length) vs. relative velocity v_r, as computed with a dense bead and spring model.

$3.38\mathring{A}$. Beads within the same CNT are connected by harmonic springs with stiffness $K_n = 270.0eV/\mathring{A}$. An angular potential $E = 0.5K_b(\theta - \theta_0)^2$ is applied to reproduce the bending stiffness of CNTs, where θ stands for the angle between three consecutive beads. Here $K_b = 6,599eV$ and $\theta_0 = 180°$. Beads located on separate tubes interact by Lennard-Jones potential with $\epsilon = 0.11eV$ and $\sigma = 12.7\mathring{A}$.

With the bead-and-spring model, we performed similar uniaxial tensile test as in Figure 6.2. The network was exactly the same as the one in Fig 6.1.Velocities were applied to two thin layers of beads to realize a constant strain rate of $10^{-8}s^{-1}$. Other than the two thin layers of beads, other particles were evolved with canonical ensemble at 300 K. The network was stretched until 100%.

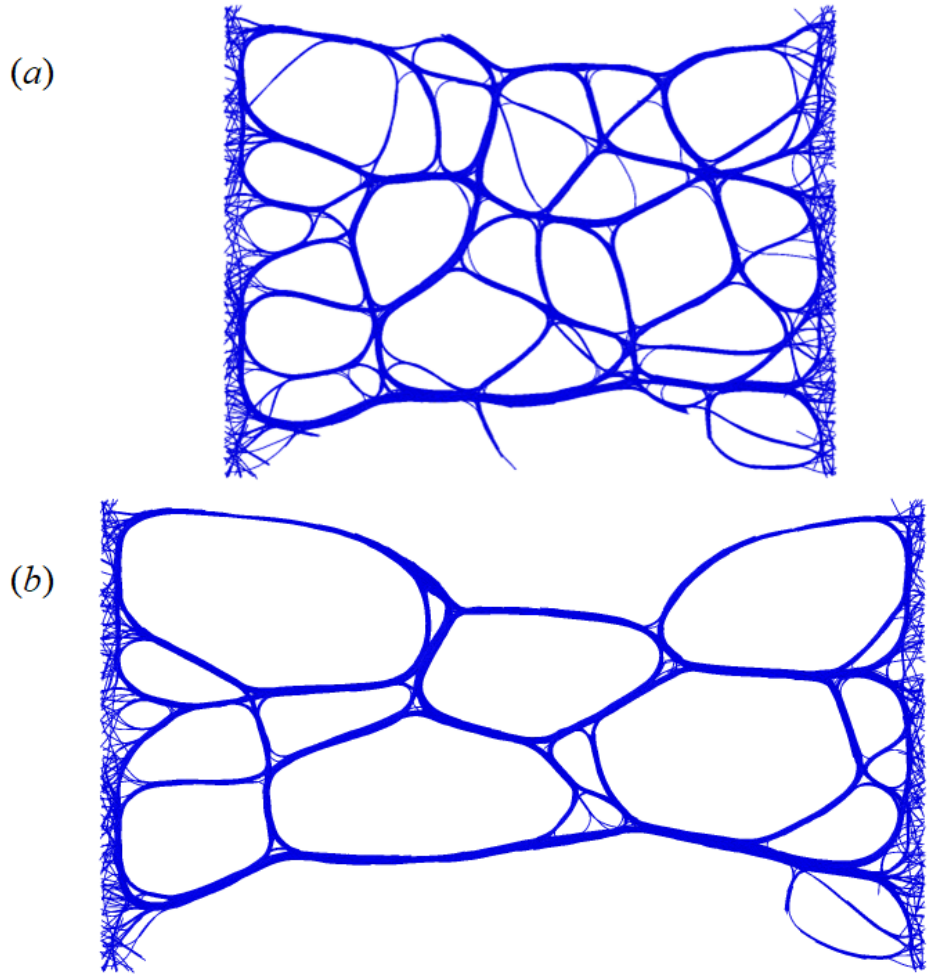

Figure 6.12. The CNT network of Figure 5.1 under (a) $\epsilon = 30\%$ and (b) $= 75\%$.

The apparent difference from mDEM simulations is the evolution of network structure is dominated by the bundling process, Fig 6.12. From the beginning of our simulation, bundling happens with much faster rate than in mDEM simulation. Entanglement of CNTs fails to hinder the process. CNTs easily sneak through each other. As bundling proceeds, small pores get annihilated and merge

into bigger ones. While under 30% strain, the pore sizes already exceeds to a large degree the maximum pore size one can observe during mDEM simulations. To better understand the phenomenon, energy evolution was plotted in Figure 6.13. The dominating bundling is in good match with the dramatic drop of vdW energy. As a cost, bending energy and stretching energy increases. Nevertheless, the increased bending energy is hardly comparable with the drop of vdW energy. And the change of stretching energy is even less noticeable.

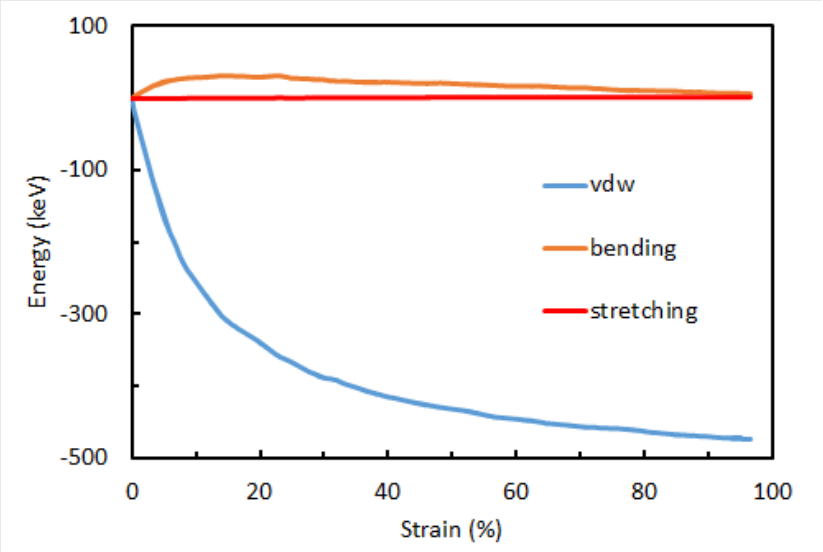

Figure 6.13. Energy vs. ϵ during stretching the network of Figure 5.1.

6.5 Conclusions

In this chapter we have developed a framework to introduce the MD computed phononic nanofriction into the athermal mDEM method. The resulted model was used to simulate the CNT yarn formed by stretching (10,10) CNT networks, which are stabilized by room-temperature nanofriction. The deformation stages obtained in the simulations, including a strain hardening one, are in good agreement with experimental observations on stretching the buckypaper formed from multi-walled CNTs. The model facilitates fundamental understanding and exploration of the parameter design space for the development of yarn processing strategies. Our simulations indicated that achieving a good load transfer through the stretched network is key for directing the zipping relaxations in order to process a yarn with well-aligned CNTs and nano-scale porosity. This type of response cannot be achieved with the purely athermal model, i.e., without accounting for the CNT "stickiness" provided by nanofriction. Enhancing nanofriction by polymer coatings is beneficial, especially in networks containing long and hooked individual CNTs, while reducing the room-temperature phononic nanofriction for example by increasing the temperature, compromises the strain-induced alignment process. Without being directed by the applied strain, the zipping relaxation evolves the CNT film into a highly bundled, cellular network

structure. Yarns formed by stretching these cellular networks are shown to maintain a higher porosity. Our exploratory results considering increased nanofriction (for $\gamma = 0.36pNs/m$) anticipate that the bridging of the scales approach pursued here for neat CNTs can be extended to include the enhancement in dissipation caused by the presence of specific polymeric layers, and to simulate the different regimes of deformation from polymer-specific impregnated CNT networks. As a comparison, a bead-and-spring model was also used to simulate the same tensile test of the CNT network. Simple bead-and-spring model demonstrates its limitations in modeling such a complex network. Bundling driven by vdW forces is the key factor under bead-and-spring model. The network quickly evolves into a few bundles, leading to the creation of pores with characteristic dimensions larger than tens of nms and poor load transfer.

Chapter 7

Conclusions

This thesis focuses on studying mechanics of complex CNT networks with multiscale modeling and simulations. Starting with atomistic simulations, I am able to get a clear quantitative description of the frictional and elastic properties of CNTs. Nevertheless, as the cost of the accuracy and reliability, atomistic simulations are still not applicable at mesoscale. CG models are usually used to solve this issue. Simple CG models like BS model have limitations in their efficiency or capability of reproducing atomistic properties. Thus we made resource to DEM and developed a ultra CG model for CNTs. The model was informed by and verified against atomistic data. The mDEM model was further applied to study the stretching process of CNT networks, unveiling intriguing mechanical behaviors.

In Chapter 2, we re-examined the widely-studied CNT oscillator problem with MD. Instead of L-J potential, the application of K-C potential to describe vdW interaction between CNTs brings significantly enhanced corrugation and brand new phenomenon. This example shows K-C potential is critical when considering friction between CNTs.

In Chapter 3, a systematic exploration of friction between both cylindrical and collapsed CNTs were conducted. Several factors including relative sliding velocity, interface commensuration, contact area, and temperature decide the magnitude of friction. The friction data were fed into the mDEM model with the viscous damping parameter.

Chapter 4 studied elasticity of single CNT with DFTB under objective boundary conditions. We got quantum mechanical insights on the mechanical response of collapsed CNTs under stretching, twisting and bending deformations. An elastic beam model was introduced to match the elasticity, and was then discretized into mDEM elements.

Chapter 5 extended the bending simulations from collapsed CNTs to FLG. It was discovered inter-layer sliding could lead to drop of bending rigidity for FLG and nano-meter scale low-energy rippling mode.

Chapter 6 showed mDEM simulations of stretching CNT network in relation to experimental CNT yarn formation process. The deformation stages

were in good agreement with experimental observations. Friction was proved to play an important role in the load transfer during the tensile test.

The mDEM model facilitates fundamental understanding of mesoscale mechanics of CNT network. The current mDEM model can be further amended. For example, CNT networks often contains catalyst nano-particles. These particles could be important in determining local morphology and might enhance friction. A model descrbing interaction between nano-paritcles with CNTs would be desirable. Also, the methodology to design such CG models can be applied in other fields as well.

Bibliography

[1] Traian Dumitrica, Ming Hua, and Boris I Yakobson. Symmetry-, time-, and temperature-dependent strength of carbon nanotubes. *Proceedings of the National Academy of Sciences*, 103(16):6105–6109, 2006.

[2] Igor Ostanin, Roberto Ballarini, David Potyondy, and Traian Dumitrică. A distinct element method for large scale simulations of carbon nanotube assemblies. *Journal of the Mechanics and Physics of Solids*, 61(3):762–782, 2013.

[3] Aleksey N Kolmogorov and Vincent H Crespi. Registry-dependent interlayer potential for graphitic systems. *Physical Review B*, 71(23):235415, 2005.

[4] TW Ebbesen, HJ Lezec, H Hiura, JW Bennett, HF Ghaemi, and T Thio. Electrical conductivity of individual carbon nanotubes. *Nature*, 382(6586):54, 1996.

[5] Eric Pop, David Mann, Qian Wang, Kenneth Goodson, and Hongjie Dai. Thermal conductance of an individual single-wall carbon nanotube above room temperature. *Nano letters*, 6(1):96–100, 2006.

[6] Jihong Al-Ghalith, Hao Xu, and Traian Dumitrică. Collapsed carbon nanotubes as building blocks for high-performance thermal materials. *Physical Review Materials*, 1(5):056001, 2017.

[7] Sulin Zhang, Roopam Khare, Ted Belytschko, K Jimmy Hsia, Steven L Mielke, and George C Schatz. Transition states and minimum energy pathways for the collapse of carbon nanotubes. *Physical Review B*, 73(7):075423, 2006.

[8] Emilie J Siochi and Joycelyn S Harrison. Structural nanocomposites for aerospace applications. *MRS Bulletin*, 40(10):829–835, 2015.

[9] William L Jorgensen, Jayaraman Chandrasekhar, Jeffry D Madura, Roger W Impey, and Michael L Klein. Comparison of simple potential functions for simulating liquid water. *The Journal of chemical physics*, 79(2):926–935, 1983.

[10] RC Haddon. Comment on the relationship of the pyramidalization angle at a conjugated carbon atom to the σ bond angles. *The Journal of Physical*

Chemistry A, 105(16):4164–4165, 2001.

[11] Peter A Cundall and Otto DL Strack. A discrete numerical model for granular assemblies. *geotechnique*, 29(1):47–65, 1979.

[12] Pere Andreu Ubach, Ferran Arrufat, Lev Ring, Raju Gandikota, Francisco Zárate, and Eugenio Oñate. Application of an enhanced discrete element method to oil and gas drilling processes. *Computational particle mechanics*, 3(1):29–41, 2016.

[13] Igor Ostanin, Roberto Ballarini, David Potyondy, and Traian Dumitrică. A distinct element method for large scale simulations of carbon nanotube assemblies. *Journal of the Mechanics and Physics of Solids*, 61(3):762–782, 2013.

[14] PFC3D Itasca. Particle flow code in 3 dimensions, user's guide, 2008.

[15] Alexey N Volkov and Leonid V Zhigilei. Mesoscopic interaction potential for carbon nanotubes of arbitrary length and orientation. *The Journal of Physical Chemistry C*, 114(12):5513–5531, 2009.

[16] Igor Ostanin, Roberto Ballarini, and Traian Dumitrică. Distinct element method modeling of carbon nanotube bundles with intertube sliding and dissipation. *Journal of applied mechanics*, 81(6):061004, 2014.

[17] Hao Xu and Traian Dumitrică. Role of inter-tube corrugation in the dynamic sliding friction of concentric carbon nanotubes: Implications for nanomechanical oscillator devices. *Extreme Mechanics Letters*, page 10508, 2019.

[18] Hao Xu, Jihong Al-Ghalith, and Traian Dumitrică. Smooth sliding and superlubricity in the nanofriction of collapsed carbon nanotubes. *Carbon*, 134:531–535, 2018.

[19] Hao Xu, Grigorii Drozdov, Ben Hourahine, Jin Gyu Park, Rebekah Sweat, Thomas Frauenheim, and Traian Dumitrică. Collapsed carbon nanotubes: From nano to mesoscale via density functional theory-based tight-binding objective molecular modeling. *Carbon*, 143:786–792, 2019.

[20] Yuezhou Wang, Hao Xu, Grigorii Drozdov, and Traian Dumitrică. Mesoscopic friction and network morphology control the mechanics and processing of carbon nanotube yarns. *Carbon*, 139:94–104, 2018.

[21] Sumio Iijima. Helical microtubules of graphitic carbon. *nature*, 354(6348):56, 1991.

[22] D-B Zhang and T Dumitrică. Elasticity of ideal single-walled carbon nanotubes via symmetry-adapted tight-binding objective modeling. *Applied physics letters*, 93(3):031919, 2008.

[23] Traian Dumitrica, Ming Hua, and Boris I Yakobson. Symmetry-, time-, and temperature-dependent strength of carbon nanotubes. *Proceedings of the National Academy of Sciences*, 103(16):6105–6109, 2006.

[24] Aleksey N Kolmogorov and Vincent H Crespi. Smoothest bearings: interlayer sliding in multiwalled carbon nanotubes. *Physical Review Letters*, 85(22):4727, 2000.

[25] John Cumings and A Zettl. Low-friction nanoscale linear bearing realized from multiwall carbon nanotubes. *science*, 289(5479):602–604, 2000.

[26] Quanshui Zheng and Qing Jiang. Multiwalled carbon nanotubes as gigahertz oscillators. *Physical review letters*, 88(4):045503, 2002.

[27] FP Bowden and D Tabor. Friction and lubrication of solids: Oxford univ. *Press (London), Pt. I*, 1954.

[28] Tobin Filleter, Scott Yockel, Mohammad Naraghi, Jeffrey T Paci, Owen C Compton, Maricris L Mayes, SonBinh T Nguyen, George C Schatz, and Horacio D Espinosa. Experimental-computational study of shear interactions within double-walled carbon nanotube bundles. *Nano letters*, 12(2):732–742, 2012.

[29] Jeffrey T Paci, Al'ona Furmanchuk, Horacio D Espinosa, and George C Schatz. Shear and friction between carbon nanotubes in bundles and yarns. *Nano letters*, 14(11):6138–6147, 2014.

[30] Seiji Akita and Yoshikazu Nakayama. Interlayer sliding force of individual multiwall carbon nanotubes. *Japanese journal of applied physics*, 42(7S):4830, 2003.

[31] SB Legoas, VR Coluci, SF Braga, PZ Coura, SO Dantas, and Douglas S Galvao. Molecular-dynamics simulations of carbon nanotubes as gigahertz oscillators. *Physical review letters*, 90(5):055504, 2003.

[32] Wanlin Guo, Yufeng Guo, Huajian Gao, Quanshui Zheng, and Wenyu Zhong. Energy dissipation in gigahertz oscillators from multiwalled carbon nanotubes. *Physical Review Letters*, 91(12):125501, 2003.

[33] Paul Tangney, Steven G Louie, and Marvin L Cohen. Dynamic sliding friction between concentric carbon nanotubes. *Physical review letters*, 93(6):065503, 2004.

[34] Zhengrong Guo, Tienchong Chang, Xingming Guo, and Huajian Gao. Thermal-induced edge barriers and forces in interlayer interaction of concentric carbon nanotubes. *Physical review letters*, 107(10):105502, 2011.

[35] Aleksey N Kolmogorov and Vincent H Crespi. Registry-dependent interlayer potential for graphitic systems. *Physical Review B*, 71(23):235415, 2005.

[36] A Carlson and T Dumitrică. Extended tight-binding potential for modelling intertube interactions in carbon nanotubes. *Nanotechnology*, 18(6):065706, 2007.

[37] M Enachescu, RJA Van Den Oetelaar, Robert W Carpick, DF Ogletree, CFJ Flipse, and Miguel Salmeron. Atomic force microscopy study of an ideally hard contact: the diamond (111)/tungsten carbide interface. *Physical review letters*, 81(9):1877, 1998.

[38] Jacqueline Krim. Friction and energy dissipation mechanisms in adsorbed molecules and molecularly thin films. *Advances in Physics*, 61(3):155–323, 2012.

[39] Steve Plimpton. Fast parallel algorithms for short-range molecular dynamics. *Journal of computational physics*, 117(1):1–19, 1995.

[40] Steven J Stuart, Alan B Tutein, and Judith A Harrison. A reactive potential for hydrocarbons with intermolecular interactions. *The Journal of chemical physics*, 112(14):6472–6486, 2000.

[41] James Servantie and Pierre Gaspard. Translational dynamics and friction in double-walled carbon nanotubes. *Physical Review B*, 73(12):125428, 2006.

[42] MM Van Wijk, M Dienwiebel, JWM Frenken, and A Fasolino. Superlubric to stick-slip sliding of incommensurate graphene flakes on graphite. *Physical Review B*, 88(23):235423, 2013.

[43] Bernd Bauerhenne, Eeuwe S Zijlstra, Alan Kalitsov, and Martin E Garcia. Controlling three laser-excited coherent phonon modes in boron nitride nanotubes to produce ultrashort shaped terahertz pulses: Implications for memory devices. *ACS Applied Nano Materials*, 1(12):6932–6937, 2018.

[44] ME Itkis, DE Perea, S Niyogi, SM Rickard, MA Hamon, H Hu, B Zhao, and RC Haddon. Purity evaluation of as-prepared single-walled carbon nanotube soot by use of solution-phase near-ir spectroscopy. *Nano Letters*, 3(3):309–314, 2003.

[45] Emilie J Siochi and Joycelyn S Harrison. Structural nanocomposites for aerospace applications. *MRS Bulletin*, 40(10):829–835, 2015.

[46] Ray H Baughman, Anvar A Zakhidov, and Walt A De Heer. Carbon nanotubes–the route toward applications. *science*, 297(5582):787–792, 2002.

[47] Sergio B Legoas, Ronaldo Giro, and Douglas S Galvao. Molecular dynamics simulations of c60 nanobearings. *Chemical physics letters*, 386(4-6):425–429, 2004.

[48] Andrea Vanossi, Nicola Manini, Michael Urbakh, Stefano Zapperi, and Erio Tosatti. Colloquium: Modeling friction: From nanoscale to mesoscale. *Reviews of Modern Physics*, 85(2):529, 2013.

[49] James Servantie and Pierre Gaspard. Methods of calculation of a friction coefficient: application to nanotubes. *Physical review letters*, 91(18):185503, 2003.

[50] Paul Tangney, Steven G Louie, and Marvin L Cohen. Dynamic sliding friction between concentric carbon nanotubes. *Physical review letters*, 93(6):065503, 2004.

[51] Paul Tangney, Marvin L Cohen, and Steven G Louie. Giant wave-drag enhancement of friction in sliding carbon nanotubes. *Physical review letters*, 97(19):195901, 2006.

[52] Wengen Ouyang, Ming Ma, Quanshui Zheng, and Michael Urbakh. Frictional properties of nanojunctions including atomically thin sheets. *Nano letters*, 16(3):1878–1883, 2016.

[53] MM Van Wijk, M Dienwiebel, JWM Frenken, and A Fasolino. Superlubric to stick-slip sliding of incommensurate graphene flakes on graphite. *Physical Review B*, 88(23):235423, 2013.

[54] Diana Berman, Sanket A Deshmukh, Subramanian KRS Sankaranarayanan, Ali Erdemir, and Anirudha V Sumant. Macroscale superlubricity enabled by graphene nanoscroll formation. *Science*, 348(6239):1118–1122, 2015.

[55] Rebekah D Downes, Ayou Hao, Jin Gyu Park, Yi-Feng Su, Richard Liang, Benjamin D Jensen, Emilie J Siochi, and Kristopher E Wise. Geometrically constrained self-assembly and crystal packing of flattened and aligned carbon nanotubes. *Carbon*, 93:953–966, 2015.

[56] Steve Plimpton. Fast parallel algorithms for short-range molecular dynamics. *Journal of computational physics*, 117(1):1–19, 1995.

[57] Aleksey N Kolmogorov and Vincent H Crespi. Registry-dependent interlayer potential for graphitic systems. *Physical Review B*, 71(23):235415, 2005.

[58] Steven J Stuart, Alan B Tutein, and Judith A Harrison. A reactive potential for hydrocarbons with intermolecular interactions. *The Journal of chemical physics*, 112(14):6472–6486, 2000.

[59] A Carlson and T Dumitrică. Extended tight-binding potential for modelling intertube interactions in carbon nanotubes. *Nanotechnology*, 18(6):065706, 2007.

[60] Hao Xu, Jihong Al-Ghalith, and Traian Dumitrică. Smooth sliding and superlubricity in the nanofriction of collapsed carbon nanotubes. *Carbon*, 134:531–535, 2018.

[61] Jihong Al-Ghalith, Hao Xu, and Traian Dumitrică. Collapsed carbon nanotubes as building blocks for high-performance thermal materials. *Physical Review Materials*, 1(5):056001, 2017.

[62] GA Tomlinson. Cvi. a molecular theory of friction. *The London, Edinburgh, and Dublin philosophical magazine and journal of science*, 7(46):905–939, 1929.

[63] Jacqueline Krim. Friction and energy dissipation mechanisms in adsorbed molecules and molecularly thin films. *Advances in Physics*, 61(3):155–323, 2012.

[64] Igor Ostanin, Roberto Ballarini, David Potyondy, and Traian Dumitrică. A distinct element method for large scale simulations of carbon nanotube

assemblies. *Journal of the Mechanics and Physics of Solids*, 61(3):762–782, 2013.

[65] Igor Ostanin, Roberto Ballarini, and Traian Dumitrică. Distinct element method modeling of carbon nanotube bundles with intertube sliding and dissipation. *Journal of applied mechanics*, 81(6):061004, 2014.

[66] MS Radue and GM Odegard. Multiscale modeling of carbon fiber/carbon nanotube/epoxy hybrid composites: Comparison of epoxy matrices. *Composites Science and Technology*, 166:20–26, 2018.

[67] Shu Li, Jin Gyu Park, Zhiyong Liang, Theo Siegrist, Tao Liu, Mei Zhang, Qunfeng Cheng, Ben Wang, and Chuck Zhang. In situ characterization of structural changes and the fraction of aligned carbon nanotube networks produced by stretching. *Carbon*, 50(10):3859–3867, 2012.

[68] Rebekah D Downes, Ayou Hao, Jin Gyu Park, Yi-Feng Su, Richard Liang, Benjamin D Jensen, Emilie J Siochi, and Kristopher E Wise. Geometrically constrained self-assembly and crystal packing of flattened and aligned carbon nanotubes. *Carbon*, 93:953–966, 2015.

[69] Nasreen G Chopra, Lorin X Benedict, Vincent H Crespi, Marvin L Cohen, Steven G Louie, and Alex Zettl. Fully collapsed carbon nanotubes. *Nature*,

377(6545):135, 1995.

[70] E Hernandez, C Goze, P Bernier, and A Rubio. Elastic properties of c and b x c y n z composite nanotubes. *Physical Review Letters*, 80(20):4502, 1998.

[71] Benjamin D Jensen, Ananyo Bandyopadhyay, Kristopher E Wise, and Gregory M Odegard. Parametric study of reaxff simulation parameters for molecular dynamics modeling of reactive carbon gases. *Journal of chemical theory and computation*, 8(9):3003–3008, 2012.

[72] Chi Zhang, Adri CT van Duin, Jin Won Seo, and David Seveno. Weakening effect of nickel catalyst particles on the mechanical strength of the carbon nanotube/carbon fiber junction. *Carbon*, 115:589–599, 2017.

[73] Siewert J Marrink, H Jelger Risselada, Serge Yefimov, D Peter Tieleman, and Alex H De Vries. The martini force field: coarse grained model for biomolecular simulations. *The journal of physical chemistry B*, 111(27):7812–7824, 2007.

[74] J Tersoff. Empirical interatomic potential for carbon, with applications to amorphous carbon. *Physical Review Letters*, 61(25):2879, 1988.

[75] Jun-Jun Shang, Qing-Sheng Yang, and Xia Liu. New coarse-grained model and its implementation in simulations of graphene assemblies. *Journal of chemical theory and computation*, 13(8):3706–3714, 2017.

[76] Igor Ostanin, Roberto Ballarini, and Traian Dumitrică. Distinct element method modeling of carbon nanotube bundles with intertube sliding and dissipation. *Journal of applied mechanics*, 81(6):061004, 2014.

[77] Guanghua Gao, Tahir Cagin, and William A Goddard III. Energetics, structure, mechanical and vibrational properties of single-walled carbon nanotubes. *Nanotechnology*, 9(3):184, 1998.

[78] Markus J Buehler. Mesoscale modeling of mechanics of carbon nanotubes: self-assembly, self-folding, and fracture. *Journal of materials research*, 21(11):2855–2869, 2006.

[79] Alexey N Volkov and Leonid V Zhigilei. Mesoscopic interaction potential for carbon nanotubes of arbitrary length and orientation. *The Journal of Physical Chemistry C*, 114(12):5513–5531, 2009.

[80] Igor Ostanin, Roberto Ballarini, David Potyondy, and Traian Dumitrică. A distinct element method for large scale simulations of carbon nanotube

assemblies. *Journal of the Mechanics and Physics of Solids*, 61(3):762–782, 2013.

[81] Traian Dumitrică and Richard D James. Objective molecular dynamics. *Journal of the Mechanics and Physics of Solids*, 55(10):2206–2236, 2007.

[82] I Nikiforov, E Dontsova, RD James, and T Dumitrică. Tight-binding theory of graphene bending. *Physical Review B*, 89(15):155437, 2014.

[83] Jihong Al-Ghalith, Hao Xu, and Traian Dumitrică. Collapsed carbon nanotubes as building blocks for high-performance thermal materials. *Physical Review Materials*, 1(5):056001, 2017.

[84] Dirk Porezag, Th Frauenheim, Th Köhler, Gotthard Seifert, and R Kaschner. Construction of tight-binding-like potentials on the basis of density-functional theory: Application to carbon. *Physical Review B*, 51(19):12947, 1995.

[85] Dong-Bo Zhang and Traian Dumitrica. Effective strain in helical rippled carbon nanotubes: A unifying concept for understanding electromechanical response. *ACS nano*, 4(11):6966–6972, 2010.

[86] Tiago FT Cerqueira, Silvana Botti, Alfonso San-Miguel, and Miguel AL Marques. Density-functional tight-binding study of the collapse of carbon nanotubes under hydrostatic pressure. *Carbon*, 69:355–360, 2014.

[87] H Mehrez, A Svizhenko, MP Anantram, M Elstner, and Th Frauenheim. Analysis of band-gap formation in squashed armchair carbon nanotubes. *Physical Review B*, 71(15):155421, 2005.

[88] D-B Zhang, Richard D James, and T Dumitrică. Electromechanical characterization of carbon nanotubes in torsion via symmetry adapted tight-binding objective molecular dynamics. *Physical Review B*, 80(11):115418, 2009.

[89] Balint Aradi, Ben Hourahine, and Th Frauenheim. Dftb+, a sparse matrix-based implementation of the dftb method. *The Journal of Physical Chemistry A*, 111(26):5678–5684, 2007.

[90] Richard D James. Objective structures. *Journal of the Mechanics and Physics of Solids*, 54(11):2354–2390, 2006.

[91] D-B Zhang, M Hua, and T Dumitrică. Stability of polycrystalline and wurtzite si nanowires via symmetry-adapted tight-binding objective molecular dynamics. *The Journal of chemical physics*, 128(8):084104, 2008.

[92] RPB Dos Santos, E Perim, PAS Autreto, Gustavo Brunetto, and DS Galvao. On the unzipping of multiwalled carbon nanotubes. *Nanotechnology*, 23(46):465702, 2012.

[93] Ilia Nikiforov, Benjamin Hourahine, B Aradi, Th Frauenheim, and Traian Dumitrică. Ewald summation on a helix: A route to self-consistent charge density-functional based tight-binding objective molecular dynamics. *The Journal of chemical physics*, 139(9):094110, 2013.

[94] M Elstner. The scc-dftb method and its application to biological systems. *Theoretical Chemistry Accounts*, 116(1-3):316–325, 2006.

[95] Gregory M Grason. Perspective: Geometrically frustrated assemblies. *The Journal of Chemical Physics*, 145(11):110901, 2016.

[96] Annalisa Fasolino, JH Los, and Mikhail I Katsnelson. Intrinsic ripples in graphene. *Nature materials*, 6(11):858, 2007.

[97] Nelson David, Piran Tsvi, and Weinberg Steven. *Statistical mechanics of membranes and surfaces*. World Scientific, 2004.

[98] MI Katsnelson and AK Geim. Electron scattering on microscopic corrugations in graphene. *Philosophical Transactions of the Royal Society A: Mathematical, Physical and Engineering Sciences*, 366(1863):195–204, 2007.

[99] Guang-Xin Ni, Yi Zheng, Sukang Bae, Hye Ri Kim, Alexandre Pachoud, Young Soo Kim, Chang-Ling Tan, Danho Im, Jong-Hyun Ahn, Byung Hee Hong, et al. Quasi-periodic nanoripples in graphene grown by chemical vapor deposition and its impact on charge transport. *ACS nano*, 6(2):1158–1164, 2012.

[100] Yuanbo Zhang, Yan-Wen Tan, Horst L Stormer, and Philip Kim. Experimental observation of the quantum hall effect and berry's phase in graphene. *nature*, 438(7065):201, 2005.

[101] Qiang Lu, Marino Arroyo, and Rui Huang. Elastic bending modulus of monolayer graphene. *Journal of Physics D: Applied Physics*, 42(10):102002, 2009.

[102] J Scott Bunch, Scott S Verbridge, Jonathan S Alden, Arend M Van Der Zande, Jeevak M Parpia, Harold G Craighead, and Paul L McEuen. Impermeable atomic membranes from graphene sheets. *Nano letters*, 8(8):2458–2462, 2008.

[103] Daniel Garcia-Sanchez, Arend M van der Zande, A San Paulo, Benjamin Lassagne, Paul L McEuen, and Adrian Bachtold. Imaging mechanical vibrations in suspended graphene sheets. *Nano letters*, 8(5):1399–1403, 2008.

[104] Levente Tapasztó, Traian Dumitrică, Sung Jin Kim, Péter Nemes-Incze, Chanyong Hwang, and László P Biró. Breakdown of continuum mechanics for nanometre-wavelength rippling of graphene. *Nature physics*, 8(10):739, 2012.

[105] Donald W Brenner, Olga A Shenderova, Judith A Harrison, Steven J Stuart, Boris Ni, and Susan B Sinnott. A second-generation reactive empirical bond order (rebo) potential energy expression for hydrocarbons. *Journal of Physics: Condensed Matter*, 14(4):783, 2002.

[106] D-B Zhang, E Akatyeva, and T Dumitrică. Bending ultrathin graphene at the margins of continuum mechanics. *Physical review letters*, 106(25):255503, 2011.

[107] Deepti Verma, Ben Hourahine, Thomas Frauenheim, Richard D James, and Traian Dumitrică. Directional-dependent thickness and bending rigidity of phosphorene. *Physical Review B*, 94(12):121404, 2016.

[108] Kaili Jiang, Qunqing Li, and Shoushan Fan. Nanotechnology: Spinning continuous carbon nanotube yarns. *Nature*, 419(6909):801, 2002.

[109] Alan B Dalton, Steve Collins, Edgar Munoz, Joselito M Razal, Von Howard Ebron, John P Ferraris, Jonathan N Coleman, Bog G Kim, and Ray H

Baughman. Super-tough carbon-nanotube fibres. *Nature*, 423(6941):703, 2003.

[110] Mohammad Naraghi, Tobin Filleter, Alexander Moravsky, Mark Locascio, Raouf O Loutfy, and Horacio D Espinosa. A multiscale study of high performance double-walled nanotube- polymer fibers. *ACS nano*, 4(11):6463–6476, 2010.

[111] Reza Mirzaeifar, Zhao Qin, and Markus J Buehler. Mesoscale mechanics of twisting carbon nanotube yarns. *Nanoscale*, 7(12):5435–5445, 2015.

[112] Yuezhou Wang, Igor Ostanin, Cristian Gaidau, and Traian Dumitrica. Twisting carbon nanotube ropes with the mesoscopic distinct element method: Geometry, packing, and nanomechanics. *Langmuir*, 31(45):12323–12327, 2015.

[113] Canh-Dung Tran, William Humphries, Shaun M Smith, Chi Huynh, and Stuart Lucas. Improving the tensile strength of carbon nanotube spun yarns using a modified spinning process. *Carbon*, 47(11):2662–2670, 2009.

[114] Shu Li, Jin Gyu Park, Zhiyong Liang, Theo Siegrist, Tao Liu, Mei Zhang, Qunfeng Cheng, Ben Wang, and Chuck Zhang. In situ characterization of

structural changes and the fraction of aligned carbon nanotube networks produced by stretching. *Carbon*, 50(10):3859–3867, 2012.

[115] Rebekah Downes, Shaokai Wang, David Haldane, Andrew Moench, and Richard Liang. Strain-induced alignment mechanisms of carbon nanotube networks. *Advanced Engineering Materials*, 17(3):349–358, 2015.

[116] Yuezhou Wang, Grigorii Drozdov, Erik K Hobbie, and Traian Dumitrica. Excluded volume approach for ultrathin carbon nanotube network stabilization: A mesoscopic distinct element method study. *ACS applied materials & interfaces*, 9(15):13611–13618, 2017.

[117] Igor Ostanin, Roberto Ballarini, and Traian Dumitrică. Distinct element method for multiscale modeling of cross-linked carbon nanotube bundles: From soft to strong nanomaterials. *Journal of Materials Research*, 30(1):19–25, 2015.

[118] Chao Wang, Bo Xie, Yilun Liu, and Zhiping Xu. Mechanotunable microstructures of carbon nanotube networks. *ACS Macro Letters*, 1(10):1176–1179, 2012.

[119] Alexey N Volkov and Leonid V Zhigilei. Structural stability of carbon nanotube films: the role of bending buckling. *ACS nano*, 4(10):6187–6195,

2010.

[120] Chase P Broedersz and Fred C MacKintosh. Modeling semiflexible polymer networks. *Reviews of Modern Physics*, 86(3):995, 2014.

[121] Yuezhou Wang, Matthew R Semler, Igor Ostanin, Erik K Hobbie, and Traian Dumitrică. Rings and rackets from single-wall carbon nanotubes: manifestations of mesoscale mechanics. *Soft Matter*, 10(43):8635–8640, 2014.

[122] Zhiqiang Shen, Magnus Röding, Martin Kröger, and Ying Li. Carbon nanotube length governs the viscoelasticity and permeability of buckypaper. *Polymers*, 9(4):115, 2017.